A one dimensional numerical coupling of the cerebral vasculature and the cerebrospinal fluid flow in the cardio-spinal compartment

Marc Maher

Université Fédérale
Toulouse Midi-Pyrénées

THÈSE

En vue de l'obtention du

DOCTORAT DE L'UNIVERSITÉ DE TOULOUSE

Délivré par l'Université Toulouse 3 - Paul Sabatier

Présentée et soutenue par

Marc MAHER

Le 18 juin 2019

Couplage numérique unidimensionnel de l'écoulement vasculaire cérébral et du liquide céphalo-rachidien dans l'enceinte cranio-spinale

---

Ecole doctorale : **MEGEP - Mécanique, Energétique, Génie civil, Procédés**

Spécialité : **Dynamique des fluides**

Unité de recherche :
IMFT - Institut de Mécanique des Fluides de Toulouse

Thèse dirigée par
PATRICIA CATHALIFAUD

Jury

M. Olivier BALéDENT, Rapporteur
Mme Stéphanie SALMON, Rapporteure
M. Mokhtar ZAGZOULE, Examinateur
Mme Patricia CATHALIFAUD, Directrice de thèse
M. Jean-Pierre MARC-VERGNES, Invité
Mme Muriel MESCAM, Invitée

Acknowledgments

J'aimerais tout d'abord remercier Patricia Cathalifaud, de m'avoir accompagné tout le long de mes travaux. Patricia, je te remercie de m'avoir aiguillé et conseillé dans cette recherche, dans laquelle j'ai pu apprendre "l'esprit" intuitive de la recherche et à me poser les questions justes. Je remercie également Mokhtar Zagzoule pour son encadrement et ses conseils avisés. Je remercie Olivier Balédent et Stéphanie Salmon d'avoir rapporté mon manuscrit de thèse et d'avoir partagé quelques pistes de réflexion concernant l'avenir de ces travaux ainsi que les autres membres du jury, Jean-Pierre Marc Vergnes et Muriel Mescam.

Je souhaite remercier les membres du groupe ASI avec qui j'ai partagé un peu plus de trois ans de quotidien dans des conditions de travail des plus agréables. Une mention spéciale à Véronique Roig, Patricia Hern, Nadine Mandement et Pierre Brancher pour leur bienveillance ainsi que leur soutien en fin de thèse.

Ce séjour m'as également permis de faire de belles rencontres qui ont pris part à mon épanouissement dans ce travail. Et cela, je le dois entre autres à Loic, Karim, Aurélie, Johan, Guillaume, Tawfik, Marie et Elena que j'ai eu plaisir à côtoyer au cours de mon séjour à l'imft.

J'adresse mes remerciements les plus sincères aux figures inspirantes que j'ai côtoyées tout le long de ce travail : à commencer par Mady et Michel Geslin, merci à vous pour nos discussions passionnantes entre neurosciences et humanisme, merci également pour votre accompagnement invétéré et vos encouragements sans relâche. Je remercie également Nicolas Georges, ostéopathe D.O, d'avoir "synchronisé mon liquide céphalo-rachidien (LCR)" tout le long de cette thèse et pour nos intéressants échanges autour du symbolisme émotionnel et spirituel du LCR.

J'adresse mes remerciements les plus tendres à Pauline Geslin, le pilier émotionnel, celle qui m'as accompagnée nuit et jour dans cet espace hors du temps qu'est la thèse. Pauline, je te remercie pour nos échanges mémorables et passionnants autour du LCR, d'avoir nourri et attisé ma curiosité à travers nos discussions. Merci pour tes sincères encouragements et ta pleine présence. Il est sans doute énigmatique d'imaginer comment cette aventure se serait déroulée sans toi. Ce qui est certain, c'est que tu as participé à rendre ce voyage plein de sens.

Ensuite, du haut de ses 4 ans et né de la pluie de la deuxième année de thèse, je remercie mon fils Elliot, qui certainement sans le savoir a posé sa pierre à l'œuvre dans ce travail.

Enfin, c'est sans compter sur l'amour inconditionnel d'une mère qui m'as nourri et continue de me nourrir. A toi, Mona, je te dédicace ce travail, merci de m'avoir donné les moyens et la chance d'accomplir ces travaux et d'avoir sans aucun doute toujours cru en moi.

Résumé — Le liquide céphalo rachidien ou cérébro-spinal (LCS) s'écoule dans les ventricules cérébraux, les espaces sous arachnoidiens cérébraux et spinaux. Son écoulement est essentiel au fonctionnement normal du cerveau et sa perturbation est liée à des pathologies cérébrales. Un paramètre crucial directement lié à sa dynamique est la pression intracrânienne qui ne peut être mesurée que de manière invasive.

Dans cette thèse, en se basant sur l'hypothèse suivant laquelle le mouvement du LCS est principalement dûe à la pulsation artérielle cérébrale, nous modélisons numériquement le couplage entre l'écoulement sanguin dans la vascularisation cérébrale (VC), depuis les voies d'apports carotidiennes et vertébrales jusqu'aux veines jugulaires, et l'écoulement du LCS dans les espaces sous arachnoidiens cérébraux (ESAC) et spinaux (ESAS). La modélisation de ces écoulements est basée sur les équations de Navier-Stokes unidimensionnelles (1D) dans une configuration de tubes coaxiaux et souples. Dans le compartiment cérébral, le réseau des ESAC est coaxial à la VC tandis que dans le compartiment spinal, le réseau des ESAS est coaxial à la moelle épinière.

Nos conditions aux limites sont les signaux de pression des artères carotidiennes, vertébrales et des veines jugulaires. Dans un premier temps, nous utilisons un signal de pression sinusoïdal et par la suite un signal de pression physiologique admettant plusieurs harmoniques. Notre modèle a permis de reproduire le caractère pulsatile du LCS et de mettre en évidence les échanges de volume entre le compartiment crânien et spinal. Ainsi, lors d'une expansion vasculaire, nous avons pu reproduire la chasse du LCS crânien et son déplacement dans le canal spinal, mettant en évidence son rôle de compensation volumique. Nous avons également pu retrouver des valeurs d'amplitude de débits de LCS cervical entre 0.5 et 3 mL/s en accord avec des données mesurés par IRM et de pression moyenne de CSF crânien entre 2 et 8 mmHg. La prise en compte de la compliance spinale a permis également de mettre en évidence des valeurs de vitesse de propagtion du CSF spinal et d'atténuation de pression en accord avec des mesures IRM.

Par la suite, nous avons procédé à une étude paramétrique dans laquelle nous nous sommes intéressés à l'influence de la variation du volume du LCS et de la compliance des espaces sous arachnoidiens cérébraux et spinaux sur les pressions et débits dans la VC, les ESAC et les ESAS. Ces paramètres étant fortement liés aux pathologies crânio-spinales. Les résultats montrent une influence non négligeable de ces paramètres sur les maxima de débit, l'amplitude de pression et le stroke volume du LCS au niveau crânien de même que spinal. Un optimum de stroke volume du CSF spinal était atteint pour un volume global de LCS de 216 mL. Le modèle a permis de mettre en évidence qu'une diminution de la compliance cranio-spinale peut augmenter la pression intracrânienne et altérer l'écoulement du LCS. Enfin, nous avons adapté notre modèle 1D à des données spécifiques issues de mesures IRM d'une population de personnes saines ou avec des symptômes pathologiques et obtenu de bonnes corrélations entre les débits de LCS cervical calculés et mesurés.

Par la suite, cette étude permettra d'explorer le mécanisme d'autorégulation cérébrale sous la forme d'un problème de contrôle optimal en boucle fermée (dit feedback ou rétro-actif)

Mots clés : Pression intracrânienne, compliance cranio-spinale, modélisation 1d, couplage sang-LCS

Abstract — The cerebrospinal fluid (CSF) fills the ventricles, the cranial and spinal subarachnoid spaces. CSF exhibits a pulsatile motion essential to normal brain function and its flow dynamics disturbance is linked to several CSF diseases. A relevant hemodynamic parameter, the intracranial pressure, which can be acquired only invasively is closely related to CSF flow dynamics. The main goal of this study is to build, based on the hypothesis that the CSF displacement is mainly driven by the cerebral arterial pulsation, a one-dimensional model of the fluid mechanics coupling between the entire cerebral vasculature (CV) and the CSF. The CV is composed of 34 vessels depicting the arterial network, the microcirculation and the venous network. It starts from the carotid and vertebral arteries to the jugular veins and is surrounded by the cranial subarachnoid spaces. This cranial vault is then coupled to a spinal vault which consists of the spinal cord enclosed by the spinal subarachnoid spaces. Blood and CSF are considered viscous. The blood vessels and the dura mater are assumed compliants.

The boundary conditions of the blood-CSF 1D model consist of an arterial pressure signal at the inlet of the carotid and vertebral arteries and a venous steady pressure at the jugular veins. First, a sinusoidal waveform of the arterial pressure signal is employed followed by a physiological waveform signal. The study evaluates the effect of the dura mater elastance, the CSF volume and the lumbar cistern compliance on blood and CSF dynamics as their contributions are closely related to CSF disorders. First, the model was able to reproduce the CSF flow pulsatility and fluids volume exchange between the cranial and spinal compartment. We found cervical CSF peak flow between 0.5 and 3 mL/s and cranial CSF pressure between 2 and 8 mmHg which is in agreement with MRI studies. Moreover, due to the compliant spinal subarachnoid spaces, pulse wave velocity and pulse pressure attenuation were find decreasing under increasing spinal compliance.

A parametric analysis was conducted to quantify the effect of CSF volume and overall cranio-spinal compliance. Our results provide evidence of an optimal spinal CSF stroke volume for a CSF volume of 216 mL. Moreover, cranial CSF pressure was found increasing under decreasing the overall cranio spinal compliance. Finally, the model was confronted to PC-MRI measurements and we found good agreement between computed and measured cervical CSF flow.

This work constitutes the object of future studies regarding the modeling of the cerebral autoregulation mechanism as a retroactive optimal process.

Keywords:Intracranial pressure, cranio-spinale compliance, 1d modelling, blood-csf coupling

Contents

List of Figures

List of Tables

Table of Acronyms and Abbreviations

ICP	*Intracranial Pressure*
CSF	*Cerebrospinal Fluid*
sas	*Subarachnoid Space*
cv	*Cerebral vasculature*
CBF	*Cerebral Blood Flow*
CPP	*Cerebral Perfusion Pressure*
MAP	*Mean Arterial Pressure*
ICC	*Intracranial Compliance*
sc	*Spinal Cord*
IV	*Intracranial Volume*
PWV	*Pulse Wave Velocity*
PC-MRI	*Phase Contrast - Magnetic Resonance Imaging*

Chapter 1

Introduction

1.1 Historical facts about CSF discovery

The cerebrospinal fluid ...

... is a clear fluid which fills larger spaces within and around the central nervous system (CNS) referred as subarachnoid spaces and brain ventricles. Since its first mentions, CSF has been assigned countless origins and functions. Amongst them, Galen, a greek physician and philosopher, considered CSF as the *spirit of animal* and described it as *a vaporous humor in the ventricles that provided energy to the entire body* whereas Sutherland, one of the founding father of Ostheopathy has thought of the CSF as *the breath of life*. Thirty physicians and anatomists were at least involved in the CSF discovery. Among them, four greatest physicians should be considered as equal CSF's discoverers. The Egyptian physician Imhotep is the most likely to be the first one to mention intracranial CSF in vivo in 3000 B.C. Later, in 1536, the Italian anatomist Nicolo Massa described CSF within cerebral ventricles based on postmortem autopsies. Then, two centuries later, the italian physician Domenico Cotugno Niccolo was the first one to describe CSF around spinal cord through experimental postmortem research. And last but not least, three centuries later, the French physician François Magendie was the first to discover method of CSF pressure measurement and was able to lay the scientific foundation for development of the CSF dynamic research [30]. Illustration below titled "CSF discovery: from hieroglyphics symbols to MRI acquisition" depicts from left to right *The Papyrus of Smith* by Egyptian physician and architect Imhotep who first acknowledges the intracranial fluid presence, François Magendie's book title from 1842 and an MRI Sagital of neutral tube section in which CSF is red-colored. Until now, the CSF production, absorption and circulation is still the topics of many debates amongst the clinical community.

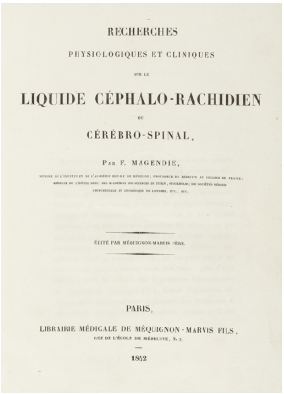
RECHERCHES

PHYSIOLOGIQUES ET CLINIQUES

LIQUIDE CÉPHALO-RACHIDIEN

CÉRÉBRO-SPINAL,

Par F. MAGENDIE,

PARIS,

LIBRAIRIE MÉDICALE DE MÉQUIGNON-MARVIS FILS,

1842

1.2 Basic concepts of brain physiology: the relationship between the cerebrospinal fluid and the intracranial pressure

The brain is a very complex organ which demands a continuous supply of oxygen. Although, it constitutes 2% of the body mass, its oxygen consumption accounts for 20% for the total body oxygen consumption. Moreover, due to its lacking stores of glucose, it also needs a continuous delivery of nutrients. Adequate oxygen and nutrients is supplied by the cerebral blood flow (CBF) via the cerebral vasculature (cv). The brain receives a CBF of 40 to 50mL/100 g of tissue per minute [61]. It is a vital need, as any reduction in CBF, known as cerebral ischaemia, occuring within seconds results in loss of consciousness and within 3-8 min in a permanent brain damage.

Factors that affect the cerebral blood flow Blood flow through a vascular segment may be described as the ratio between the pressure difference (ΔP) accross that segment and its vascular resistance (R). According to the Hagen-Poiseuille equation, the blood flow (BF) through a vascular segment of length L, radius r and blood dynamic viscosity (μ), driven by a pressure difference ΔP is given by,

$$BF = \frac{\Delta P}{R} = \frac{\pi \Delta P r^4}{8\mu L}$$

In the case of CBF, the driving pressure is known as the cerebral perfusion pressure (CPP), and the resistance is a total cerebrovascular resistance (CVR) which is related to the entire cerebral vasculature. CBF is therefore dependant upon the CPP, the CVR and the blood dynamic viscosity. For example, it will increases if the CPP increases and the CVR decreases. Under normal conditions, the CPP is variable and usually ranges between 70 and 90 mmHg . Variations in CPP may occur either under normal conditions, i.e during a change in posture or exercice or from pathological conditions such as traumatic brain injury or stroke. The CVR is affected by the small arteries, which can regulate their radius (r) through vasodilatation and vasoconstriction. Thus, when cerebral vasodilatation occurs, the increase in the radius of the vessels decreases the CVR and augments CBF. On the other hand, when vasoconstriction occurs, the CVR increases thus decreasing the CBF. This mechanism, diplayed figure 1.1a, is the so-called cerebral autoregulation which is the brain ability to maintain CBF relatively constant despite changes in the CPP. The normal range of autoregulation occurs between 60 and 150 mmHg of CPP, Beyond this plateau, CBF becomes pressure dependant.

Intracranial pressure The CPP is defined as the difference between the mean arterial pressure (MAP) and the intracranial pressure (ICP) which is the pressure in the cranial vault,

$$CPP = MAP - ICP \tag{1.1}$$

Under normal conditions, the ICP is between 10 and 20 mmHg in adults, 3 and 7 mmHg in children and 1.5 and 6 mmHg in newborns. Following the latter equation, the CPP is

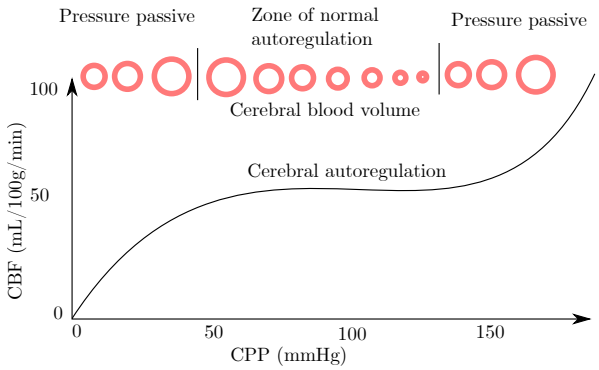

(a) Cerebral autoregulation mechanism

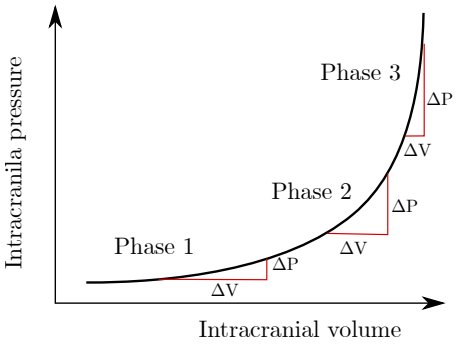

(b) The pressure-volume curve

Figure 1.1: (a) Cerebral autoregulation mechanism. (b) The relationship between intracranial pressure and intracranial volume

dependant upon the MAP and the ICP.
The concept of ICP can be explained if we assume the brain enclosed within a rigid structure. The brain contents may be divided into three main compartments: (1) the cerebral parenchyma or brain tissues (80%), (2) the cerebral vasculature (10%) and (3) the cerebrospinal fluid (10%). In an average adult, the brain tissue volume is $\sim$ 1400 mL; the blood volume is $\sim$ 150 mL; and the cranial CSF volume is $\sim$ 150 mL [31, 60]. The interaction between these components closely impacts ICP. An increase in ICP above a critical level is not tolerated because it results in a decrease in the CPP which itself results in a decrease in CBF (as a consequence of cerebral autoregulation failure) and consequently a risk of cerebral ischemia. Hopefully, under normal conditions, to avoid an increase in ICP, one or more of the other compartments must necessarily shrink. For example, in the case of a slow growing cerebral edema, the cerebral parenchyma may undergoes deformation to compensate for increased ICP. However, in the case of an abrupt raise in ICP, it is mainly the cerebral blood and CSF volume which will be responsible for compensating that increase. Thus, the reduction of the vascular compartment may consist of displacing blood by means of jugular drainage. And on the other hand, the CSF compensation role occurs by allowing a decrease in intracranial CSF volume by means of CSF displacement into the spinal canal. This compensatory mechanism is finite and is dependant of the cranio-spinal compliance.

Intracranial compliance The ratio of the intracranial volume differential (ΔV) to the intracranial pressure (ΔP) is known as the intracranial compliance (ICC). It determines the ability of the intracranial compartment to accommodate an increase in volume without a large increase in intracranial pressure.

$$ICC = \frac{\Delta V}{\Delta P}, \quad or \quad \Delta P = \frac{\Delta V}{ICC} \tag{1.2}$$

In other words, ICC can be thought as the cranial compartment adaptive capacity that lets it tolerate an increase in volume depending on its compensatory mechanisms. Figure 1.1b displays the well known pressure-volume curve. It portrays the relationship between changes

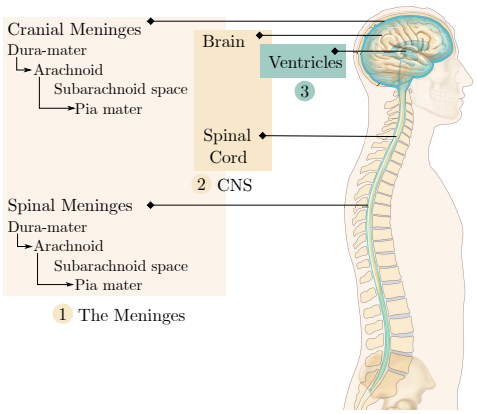

Figure 1.2: From outwards to inwards: the meninges, the central nervous system and the ventricles

in ICP and intacranial volume and may be divided into three phases, (1) Phase 1: A high compliance and low ICP. Despite the increase in volume, there is barely or a slight increase in ICP. CSF and cerebral blood volume buffering mechanisms are effective, (2) Phase 2 : A lower compliance and still a low ICP. But it starts to increase slowly as intracranial volume rises and finally, (3) Phase 3 : an inexisting compliance and high ICP. Buffering mechanisms are failling thus any small increase in intracranial volume results in a high increase in ICP.

1.3 Physiopathology of the cerebrospinal fluid system

During the previous section, we have demonstrated the crucial role and function of the CSF system acting as a buffering mechanism to ensure a steady ICP under normal conditions. However, in cases of abnormal CSF flow, the regulation of ICP is consequently disrupted.

In this section, we briefly present several prominent diseases that disrupt CSF dynamics. But first, we need to describe elementary anatomical aspects of the Central Nervous System (CNS).

Figure (1.2) displays the major components of the CNS. Working inwards from the skull lies the meninges (1), a system of three connective tissue layers. These are the dura mater, the arachnoid and the pia mater. The interval between the arachnoid membrane and the pia mater is called the subarachnoid space and is filled by CSF. The meninges covers the central nervous system (CNS) (2), composed of the brain and the spinal cord, and their vasculature. CSF is believed to be mainly produced by ependymal cells, called the choroid plexus, which line the ventricles (3), a set of four connected cavities. The ventricles are connected to cranial and spinal subarachnoid spaces through CSF filled foramina (openings) and CSF filled cisterns.

Hydrocephalus Hydrocephalus is a pathological disorder resulting from an inappropriate volume of CSF in the cerebral ventricles at an inappropriate pressure. Its symptom reflects increased ICP. Imaging hydrocephalus portrays enlargement of the cerebral ventricles with clinical evidence of inappropriately elevated pressure in the ventricles. Hydrocephalus results from either altered malabsorption of CSF at the arachnoid vili or direct obstruction by means of aqueductal of Sylvius stenosis. Clinical treatment of the stenosis is through removal of the obstructing lesion.

Chiari malformation type I Chiari malformation type 1 results from the extension of the lower part of the cerebellum (called the cerebellar tonsils) below the level of the foramen magnum into the cervical sas resulting in a alteration of CSF flow and pulsatility in the cranial compartement. Clinical treatment of CM1 consist of removing small sections of the bone to ensure enlargement of the cranio-cervical junction sas.

Syringomyelia Syringomyelia is a medical condition in which one or more fluid cavities (syrinxes) form within the spinal cord. The syrinxes often occur near locations of the spinal cord where spinal subarachnoid space is obstructed.

Although recent and ongoing progress in medical imaging is providing numerous data and new insights about the dynamics interactions of the CNS and its pathological disorders, yet the underlying physiological mechanisms of the interactions between CSF dynamics, ICP and arterial dynamics remains poorly understood. Computational model are therefore needed to provide additional predictions and interpretation of in vivo data acquired by means of medical imaging. Of special relevance, the strong coupling between arterial pulsations and CSF flow which is considered crucial in elucidating the pathophysiology of cerebrovascular and craniospinal diseases mentioned previously.

1.4 Motivation

There are numerous mathematical modelling of CSF flow in the cranium and the spinal vault. Moreover, most of these CFD models use rigid walls and finite domains such as a short segment of the sas which requires boundary conditions that are adjusted to meet the desired velocities. However, there are few models accounting for closed models of the CNS, i.e the interaction between the cranial and the spinal compartment, and accounting for compliant walls. To date and to our knowledge, there are a few models of a full CSF flow in the CNS. The first was developped by Lininger et al. [41] and consisted of multi-compartments model of the vascular system, the parenchyma and the CSF system. The model was able to predict CSF velocities through the entire CNS as driven by arterial pulsations and simulates in a simplified manner communicating hydrocephalus. However, authors have chosen to neglect unsteady and convective inertia terms for convenience, thus ignoring the important and well recognized role played by waves reflection in vascular and CSF dynamics. This model was extended to a subject specific 3D model to quantify fluid interactions between cranial and spinal CSF with a

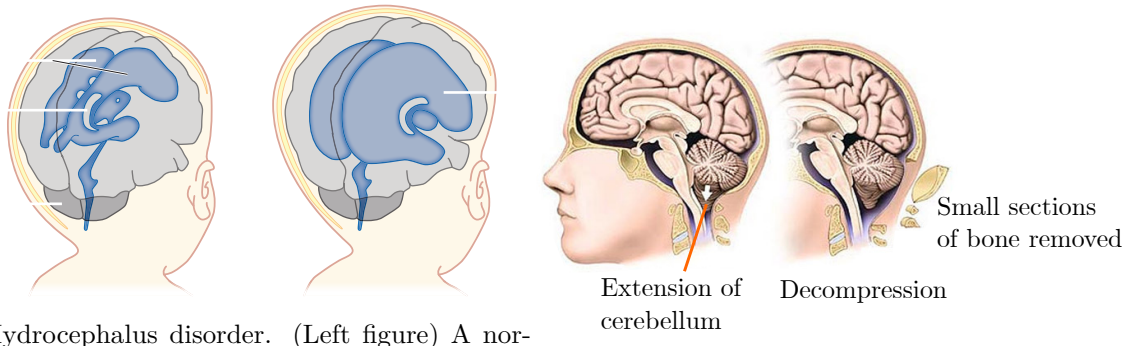

(a) Hydrocephalus disorder. (Left figure) A normal brain. (Right figure) A hydrocephalic brain displaying enlarged ventricles

(b) Chiari malformation type 1

Figure 1.3: CSF disorders. (a) Hydrocephalus, (b) Chiari malformation type 1

particular attention given to microstructures embedded within the spinal canal such as nerve roots. However, this model did not account for the main CSF motor function, i.e the cerebral arterial pulsations.

One dimensional models of compliant vessels have shown the ability to describe the major features of biological flows. Moreover, several comparison against in vivo and in vitro data have raised confidence in applying the 1-D formulation to capture blood and CSF flow in the craniospinal environment. In addition, due to their reduced computational expense compared to higher dimensional computational fluid dynamics, one dimensional models allow for parametric analysis, where specific parameters in the model can be altered to understand their distinct contribution on pulse wave propagation.

1.5 Methodolgy

In the current study, we propose to build a global one dimensional model of the interactions between compliant vessels of the cerebral vasculature and the CSF system. The cerebral vaculature was based upon the work of of Zagzoule and Marc Vergnes [73] and consisted of compliant arteries, arterioles, capillaries, veinules, veins, venous sinus and jugular veins. The CSF system comprises compliant cranial and spinal subarachnoid spaces. The model will be described and outcomes compared to in vivo results from Cine phase-contrast MRI measurements. The objective is to accurately quantify the dynamic interactions between blood flow, cranial and spinal CSF flow and therefore indirectly ICP. Moreover, the aim of this work is to provide an appropriate coupled 1D blood-CSF modeling of the craniospinal environment for patient- specific simulations to gain insights in estimating mechanical and medical relevant parameters such as intracranial pressure, intracranial CSF volume and intracranial compliance. The present work will be structured as follows, chapter 2 describes the physiology and anatomy of the central nervous sytem with a particular attention given to the cerebral vasculature and the CSF system. It also introduces the mechanical interactions between blood and CSF flow. Chapter 3 presents the 1-D mathematical formulation of the governing flow equations of

blood and CSF in a system of coaxial compliant tubes. Chapter 3 introduce the architecture of the coupled blood-CSF models and describes the CSF system parametres which are the CSF volume and the cranial and spinal subarachnoid spaces compliance. Chapter 4 performs a parametric analysis in which the effect of the latter CSF system on blood and CSF pulse wave propagation are described. Finally, in chapter 5, medical imaging data are used and confronted to outputs of the current model.

1.6 Work context

The study was conducted at l'Institut de Mécanique des Fluides de Toulouse (IMFT) in France. It is part of a project called ROMBA (Retro-active and Optimal Modelling of Blood flow Autoregulation), funded by a French state program called IDEX (Initiatives d'excellence). ROMBA project aims to simulate cerebral blood flow autoregulation described previously as the ability of the brain to maintain constant blood flow despite changes in cerebral perfusion pressures. The objective is a simulator tool and a clinical protocol, using the autoregulation time course pattern to interpret the clinical status of the craniospinal system and its aging process. ROMBA project involved researchers from four laboratories of Toulouse: the Institut de Mathématique de Toulouse (IMT), the Institut de Mécanique des Fluides de Toulouse (IMFT), the Centre de Recherche Cerveau et Cognition (CerCo), the Institut des Sciences du Cerveau de Toulouse and a fifth partner being the Amiens Hospital-University.

Chapter 2

Anatomy and physiology of the central nervous system: a focus on the cerebrospinal fluid, the cerebral vasculature and the meninges

---

Sommaire

2.1 Introduction: an anatomical scope of the major components involved in this study

Modelling the dynamics coupling between the cerebral vasculature and the cerebrospinal fluid requires rigorous anatomical description and understanding of the craniospinal environment.

This chapter is best treated under two main headings. Section one provides a description of the meninges and the ventricular system. Section two provides a description of the cerebral and spinal vasculature. And finally, section three discusses the hydrodynamic couplings between the cerebral vasculature and the CSF.

Anatomy of the craniospinal environment Describing the CNS requires an elementary understanding of standards used in anatomical terminology. Figure (2.1) depicts the relative

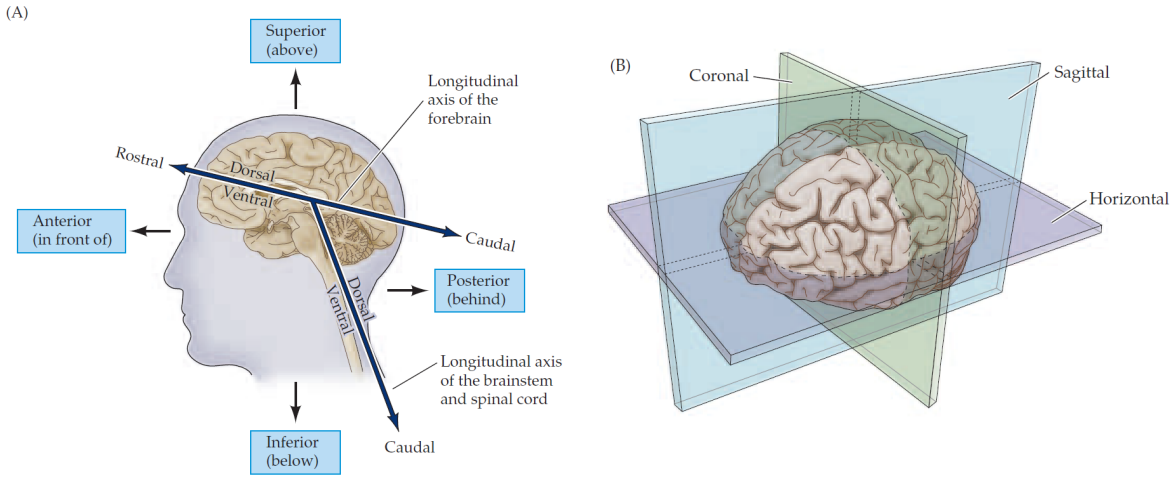

Figure 2.1: Anatomical terminology adapted from **Neurosciecne 2nd edition** [51]

directional terms and planes of reference employed to specify location in the CNS and more generally in the body. In subfigure (A), anterior and posterior refer to front and back of the head. Superior, and inferior indicates above and below the head. Rostral and caudal refer to direction toward the head and tail. For example, a rostral CSF flow refers to a flow direction toward the head. A caudal CSF flow refers to a flow direction towards the end of the spinal cord.

Subfigure (B) depicts the major planes of section used in cutting or imaging the brain. For a body standing upright, horizontal planes (also referred to as axial or transverse planes) are parallel to the ground. The sagittal plane is the section that divides the two hemispheres. The coronal or frontal plane refers to sections parallel to the plane of the face.

2.2 The cranial and spinal meninges: beyond their protective functions

The meninges are present along the cranial and the spinal compartement. They are composed of three layers: the dura mater, the arachnoid mater, and the pia mater. These tissues surround the brain and spinal cord and house the cerebrospinal fluid (CSF) located within the subarachnoid space (sas).

Figure (2.2) depicts a schematic view of the cranial meninges, a longitudinal view of the spinal cord (sc) and a section view of the sc portraying the spinal meninges.

The pia mater is the innermost layer of the meninges. It adheres to every contour of the brain and the spinal cord. It is separated from the arachnoid by the CSF-filled subarachnoid space. Furthermore, it is a highly vascular space containing blood vessels that supply the underlying surface of the brain and the spinal cord.

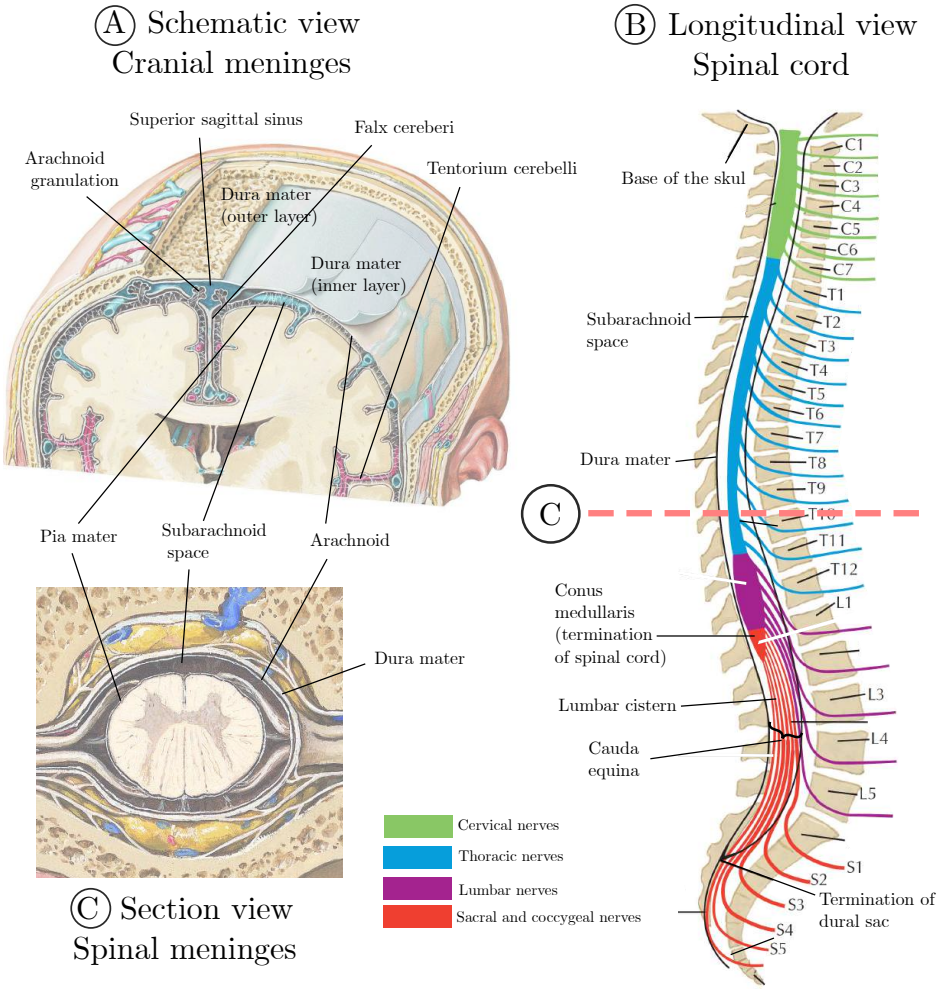

Figure 2.2: Cranial and spinal meninges adapted from *Netter's atlas of human anatomy 7th edition*[50]

The dura mater is the outermost layer of the meninges. In the brain, it is composed of two layers where the outer layer is adherent to the inner skull's surface. The deeper layer, known as the meningeal layer divides the brain into compartments. The most prominent of these are the falx cerebri and the tenorium cerebelli. In some locations, the two layers separate to provides channels, the dural venous sinuses, for return flow of the venous blood. At the foramen magnum, the cranial dura mater becomes continuous with the spinal dura mater. It has a single layer separated from the wall of the vertebral canal by the epidural space which contains adipose tissue and blood vessels. At the tapered caudal end of the spinal cord ,the conus medullaris, the spinal roots extend caudally traversing a considerable distance through the subarachnoid space of the lumbar cistern forming the cauda equina.

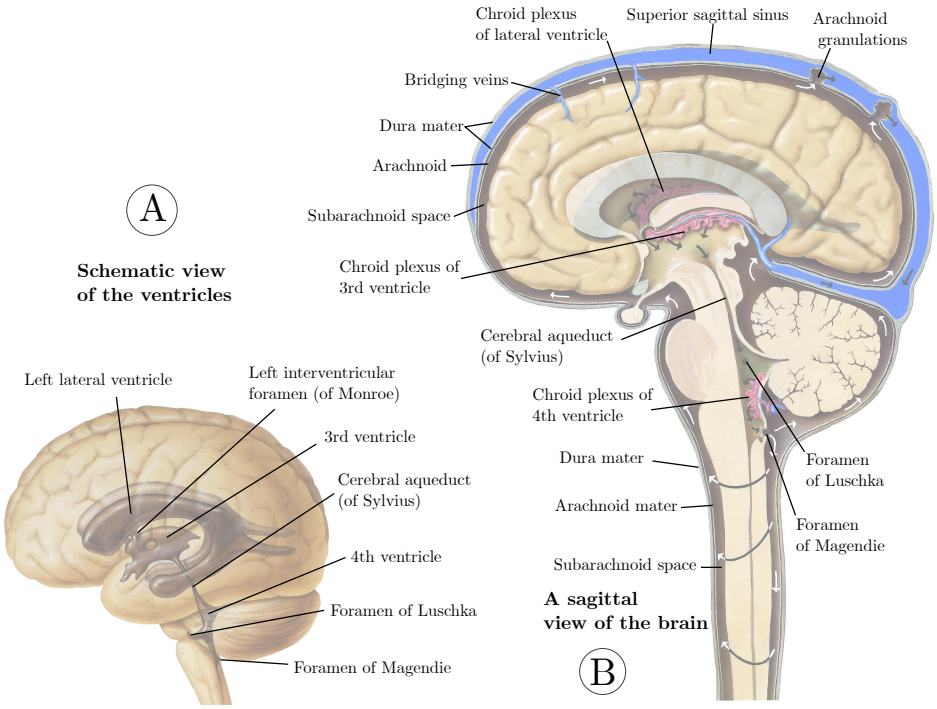

Figure 2.3: The ventricular system

2.3 The brain ventricular system

The ventricular system, figure (2.3), is a series of four interconnected ventricles and their connecting foramina (opening). The largest of these ventricles are the lateral ventricles (one within each of the cerebral hemispheres). These are connected to the third ventricle by two openings called the interventricular foramen (of Monro). Later, the third ventricle opens into the cerebral aqueduct (of Sylvius) which connects into the fourth ventricle. Finally, the fourth ventricle is later connected to subarachnoid cisterns and opens to cranial and spinal subarachnoid spaces.

The small arrows displayed in figure (2.3) (B)) portrays CSF presence within the v entricular system, the cranial and spinal subarachnoid spaces. CSF is believed to be mainly secreted through a plexus of cells called the Choroid Plexus (ChPs) embedded within the ventricles [68, 63, 17], while the remaining is being produced by other CNS structures such as the ependymal wall, cerebral parenchyma, and interstitial fluid (ISF) [34, 63, 44]. The ChPs have a relatively simple structure. It consists of a single layer of epithelial cells lying on a basement membrane. Beneath the epithelial basement membrane is a network of fenestrated capillaries supplied from both the internal carotid arteries and the vertebral artery [17, 72, 65].

In the brain, the arachnoid granulations, one way valves, expands from the subarachnoid space into the venous sinuses, especially the superior sagittal sinus, allowing CSF to drain into the venous blood. CSF may also be absorbed through nerve pathways into the extracranial lymphatic vessels [63] and arachnoid villi located at the origins of the spinal nerves [35, 56].

2.4 Arterial supply and venous drainage of the CNS: a great deal of variability

2.4.1 The brain and its need of uninterrupted blood oxygen

Arterial supply of the brain The brain, figure (2.4) (A)), is mostly supplied by two pairs of large arteries, the right and left internal carotid arteries (1) and the right and left vertebral arteries (2). The two vertebral arteries come together to form the basilar artery (3). The latter joins the two internal carotid arteries and other communicating arteries to form an arterial ring at the base of the brain known as the circle of Willis (4). The circle of Willis gives rise to three pairs of main arteries, the anterior cerebral artery (ACA) (5), the middle cerebral artery (MCA) (6), the posterior cerebral arteries (PCA) (7) and their communicating posterior (8) and anterior arteries (9). Figure (2.4) (B) and (C) illustrates the territories of distribution of the ACA, MCA and PCA along the cortical surface. Later, the main segments of the ACA, MCA and PCA branch into smaller vessels along the cortical surface. They are refered as pial arteries and are surrounded by the CSF. Later, they give rise to smaller arteries that eventually penetrate into the brain tissue, the parenchymal arterioles. The latter lie within the Virchow–Robin space which is a continuation of the subarachnoid space and varies considerably in depth. Finally, figure (2.4) (D) portrays the meningeal arteries which supply the dura mater and lies between the inner and outer layer of the dura mater.

Venous drainage of the brain Figure (2.5) depicts the venous drainage pathways of the brain. Unlike the majority of the rest of the body, the cerebral venous system does not follow the cerebral arterial system and there is significant variation in anatomy between different subjects. The venous drainage of the brain occurs via two different types of vessels: the cerebral veins (CV) and the dural venous sinuses. Cerebral veins and dural venous sinuses are different by their locations and their structures. On the one hand, cerebral veins (1) are **located within the subarachnoid space (2)** and unlike most of the body veins, they are thin and lack muscular tissue. Moreover, except for the interna jugular vein, they do not possess valves, thus bidirectional flow is possible. They ultimately aggregate into larger channels until they pierce the arachnoid mater (3) and the inner layer of the dura (4) and drain into the dural venous sinuses like the superior sagittal sinus (SSS) (2), via venous lacuna (5). Recall that CSF drain into the SSS via the arachnoid granulations (6).

On the other hand, dural venous sinuses, as the superior sagittal sinus (SSS) (2), are not true blood vessels as they consist of the spaces between the two layers of the dura mater.

Cerebral veins may be divided into cortical cerebral veins and deep cerebral veins. Superficial veins may empty into the superior sagittal sinus (SSS) (2) and deep veins may empty into the inferior sagittal sinus (ISS) (6) or great vein of Galen (7) and the straight sinus (8). Venous flow is afterwards directed toward the confluence of sinuses (9) then on toward the

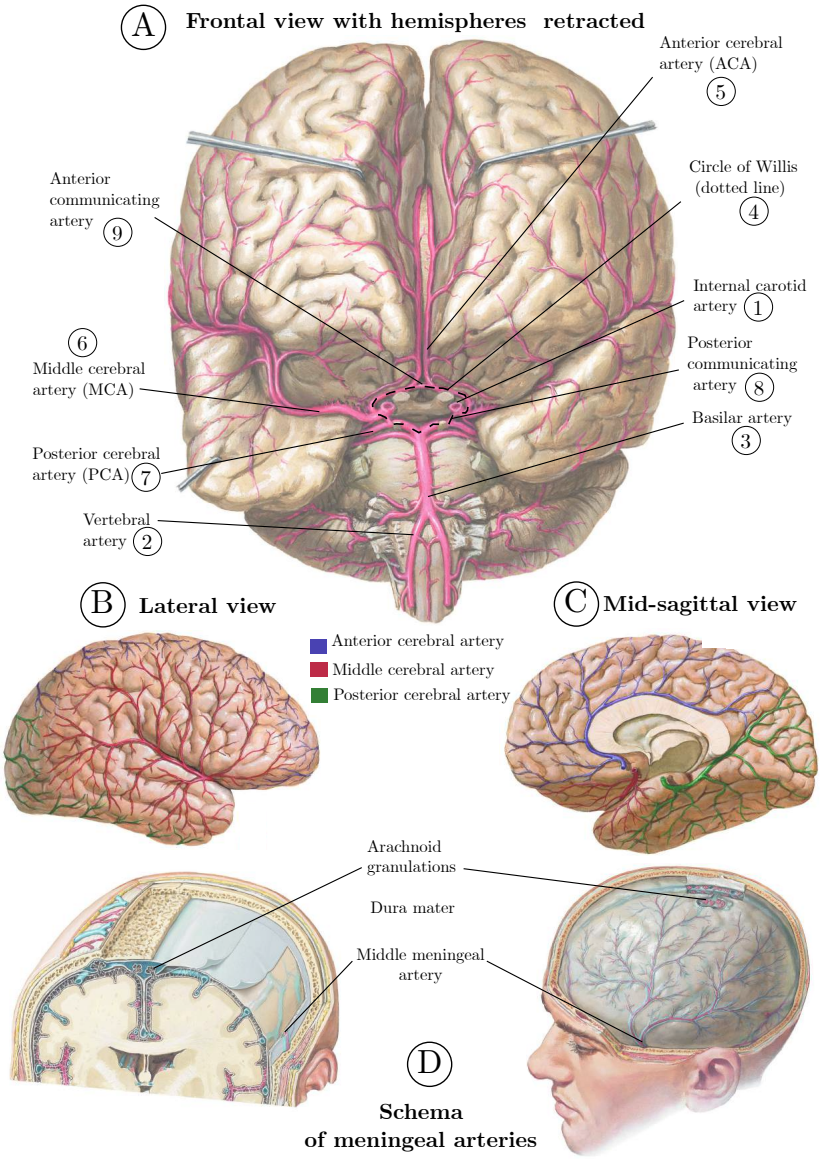

Figure 2.4: Arterial supply of the brain adapted from *Netter's atlas of human anatomy 7th edition*[50]

central circulation via the transverse sinus (10), sigmoid sinus (11), and ultimately empties into the jugular veins. Along the jugular vein, there are several routes that allow complementary venous drainage in the brain in particular in the upright position.

2.4.2 The spinal cord

The spinal cord, (2.6), is mostly supplied by the anterior (ASA) and the paired posterior spinal arteries (PSA) which derives from the vertebral artery. Radicular arteries, such as the artery of Adamkiewicz, deriving from the aorta, anastomose with ASA and PSA and reinforce the

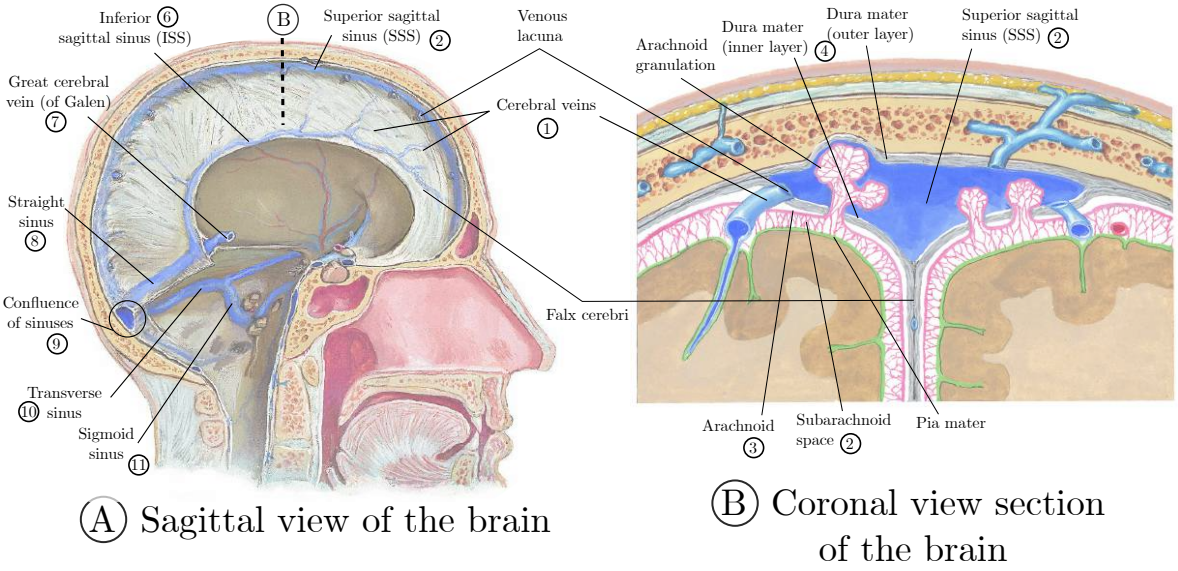

Figure 2.5: Venous drainage of the brain adapted from *Netter's atlas of human anatomy 7th edition*[50]

blood supply to the spinal cord. Later, the ASA and PSA penetrate through the subarachnoid space giving rise to pial arterial plexus.
Venous drainage largely follows arterial supply. An internal venoux plexus, located within the epidural space and the subarachnoid space drain into the anterior, posterior and radicular veins.

2.5 Cerebrospinal fluid motion and its coupling to the cerebral vasculature

In adults, mean CSF volume is estimated to be 150 mL with a distribution of 25 ml within the ventricles and 125 ml within the subarachnoid spaces. CSF forms at a rate of 500–600 mL/day. Therefore, the CSF is replaced three to four times per day. [11, 17].
CSF pulsates through the ventricular system. Magnetic resonance imaging (MRI) studies have confirmed that the cardiac cycle imposes its pulsatile pattern onto the CSF dynamics [24, 70]. CSF also flows from the cranial to the spinal SAS in systole, with flow reversal from the spinal SAS into the cranium in diastole [28]. Besides cardiac driven pulsations, respiration influence on the CSF oscillations has been described in many radiological studies. It produces a modulation of the intracranial pressure resulting in a smaller additional oscillation of the CSF [37, 21].

Freund et al. 2001 [26] suggests, using MRI that the total cerebral blood volume inflates and deflates in each cardiac cycle by approximately 1–2 mL, the same volumetric amount as there is CSF exchange between the cranial and spinal SAS. In addition to CSF pulsations with no net flux, there is evidence of a small volumetric bulk component due to CSF production

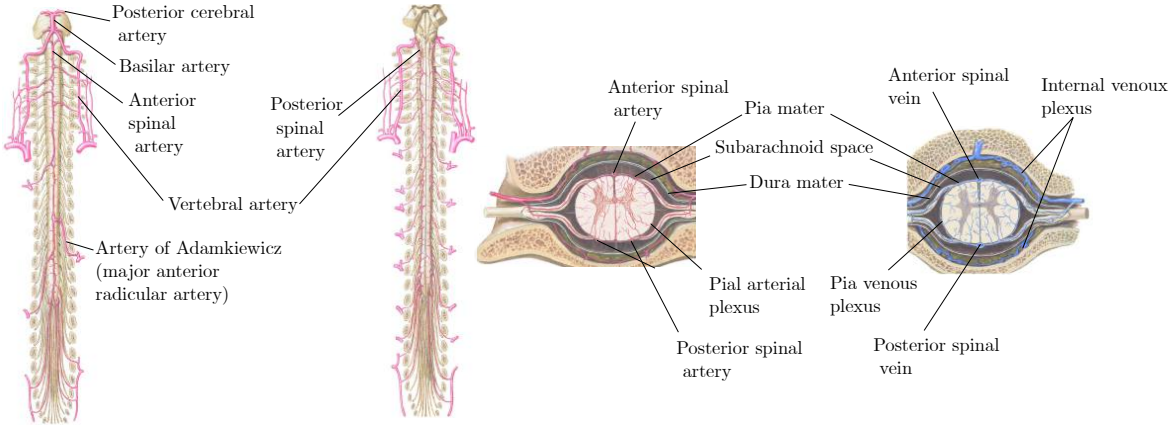

Figure 2.6: Arterial supply and venous drainage of the spinal cord adapted from *Netter's atlas of human anatomy 7th edition*[50]

and absorption.

So long, pulsatile CSF oscillations are believed to be driven by systolic vascular dilatation followed by diastolic contraction. From a mechanical point of view, this motion may be explained based on a concept known as the Monro-Kellie dogma [48]. Because the skull is a rigid box, the sum of the volumes occupied by the brain, the vasculature, the meninges, the ventricular system and the CSF must remain constant. The spinal cord has the same components but less rigid constraints on its total volume. Therefore, when the volume of one of the components increases, the volume of another must decrease to compensate increase in ICP. Thus, during a normal cardiac cycle, volume variation of the cerebral vasculature triggers CSF displacement.

Figure (2.7) portrays the overall concept of the Monro-Kellie doctrine employed in this study. The cranial compartment depicts the cerebral vasculature, the cranial subarachnoid space and the cranial dura mater and is coupled to the spinal compartment composed of the spinal dura mater, the spinal cord and the lumbar cistern. Thus, in this work, the Monro-Kellie dogma is reduced in the brain compartment to two components being the cerebral vasculature and the cranial subarachnoid space. Volumetric variations of the cerebral parenchym is being neglected. Based on this concept, a simplified one-dimensional model was built involving the following components of the CNS: the cerebral vasculature, the cranial and spinal subarachnoid spaces and finally the spinal cord.

Moreover, the dynamic coupling between a blood vessel and a cranial subarachnoid space has been approached using a model of two compliant and coaxial tubes as illustrated in figure (2.7) where the interior tube represents a blood vessel and the exterior tube represents a cranial subarachnoid-space enclosed by the dura mater. CSF flows in the annular space. By assuming a dura mater more rigid than the blood vessel, consequently as blood vessel expands, CSF flows out and as the blood vessel contracts, CSF flows in. Based on this coaxial configuration, we have expanded the one dimensional cerebral vasculature of Zagzoule and Marc Vergnes [73] and build upon it CSF flow in the cranial and spinal vault. The next chapter will be

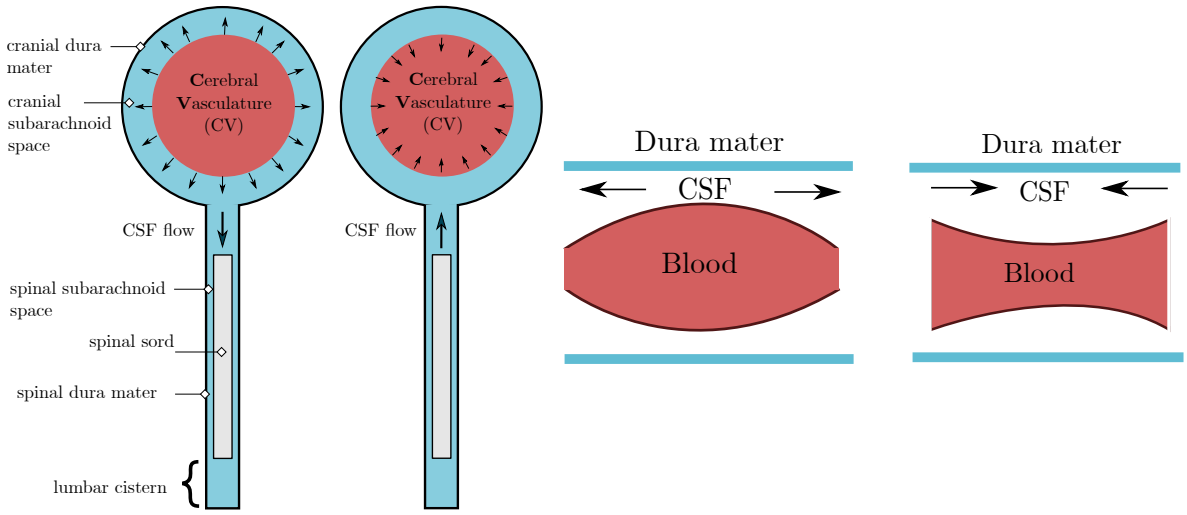

Figure 2.7: (a) An idealized representation of the interaction between blood and CSF. The left figure depicts CSF flowing towards the spinal cord during cerebral vasculature dilatation following by, in the right figure, CSF flowing towards the brain skull during cerebral vasculature contraction. (b) A coaxial configuration of two compliant vessels

dedicated to describing the morphological and mechanical characteristics of this model.

Chapter 3

The 1D craniospinal blood-CSF model

Sommaire

3.1 Introduction

In chapter 2, we have highlighted the fact that CSF oscillations and motion between the cranial and the spinal compartment are mainly driven by dilatation and contraction of the cerebral vasculature. In this chapter, we present the one dimensional model of blood and CSF couplings in the cranio-spinal vault.

First, we recall the one-dimensional model of Zagzoule and Marc Vergnes [73]. Then, we describe the geometric configuration used to model the cranial and spinal subarachnoid spaces. Finally, we investigate their mechanical properties.

3.2 The cerebral vasculature : the 1D blood model from Zagzoule and Marc Vergnes

Figure (3.2) portrays the 1D cerebral vasculature model from Zagzoule and Marc Vergnes [73]. It consists of a simplified morphological scheme portraying the major segments of the brain

Segment number(s)	Vessels	Cross-section A_0 (cm^2)	Length L (cm)	Elastance E_{L_2} (10^5 dyn cm^{-2})	Number of vessels
1 and 2	Internal carotid arteries (below posterior communicating arteries)	0.14	25.0	13.67	1
3 and 4	Vertebral arteries	0.09	25.0	13.67	1
5	Basilar artery: first part	0.19	2.0	27.35	1
6	Basilar artery: second part	0.09	2.0	27.35	1
7 and 8	Posterior cerebral arteries	0.07	2.0	27.35	1
9 and 10	Posterior communicating arteries	0.02	2.0	27.35	1
11 and 12	Internal carotid arteries (above posterior communicating arteries)	0.14	2.0	27.35	1
13 and 14	Anterior cerebral arteries (below anterior communicating arteries)	0.07	2.0	27.35	1
15 and 16	Posterior cerebral arteries	0.07	25.0	30.08	1
17 and 18	Middle cerebral arteries	0.12	35.0	30.08	1
19	Anterior cerebral arteries (above posterior communicating arteries)	0.12	25.0	30.08	2
20	Main branches of cerebral arteries	0.55	10.0	33.09	50
21	Pial network	1.75	3.5	36.40	3900
22	Intracerebral arteries	4.74	3.5	40.04	35000
23	Microcirculation	38.0	0.5	44.04	202000
24	Intracerebral veins	9.49	3.5	27.35	72000
25	Pial veins	3.86	3.5	13.0	3800
26	Cerebral veins	0.92	5.0	5.17	40
27	Cerebral veins	0.33	5.0	5.0	10
28	Longitudinal sinuses: first part	0.15	15.0	117.0	2
29	Veins	0.49	15.0	5.0	10
30	Longitudinal sinuses: second part	0.47	20.0	117.25	2
31	Veins	0.29	10.0	5.0	30
32	Transverse sinuses	1.65	5.0	117.78	1
33 and 34	Jugular veins	0.43	15.0	2.65	1

Figure 3.1: Morphological an rheological data used in Zagzoule et a. 1D model [73]

arterial supply and venous drainage. Blood was assumed to be a Newtonian fluid with density $\rho_b = 1.06$ kg.m^{-2} and dynamic viscosity of $\mu_b = 0.0035$ Pa.s.

It starts at the paired internal carotid arteries (1, 2) and the paired vertebral arteries (3, 4) followed by the basilar artery 5 & 6, the circle of Willis (from 7 to 14), the cerebral arteries, the middle (17, 18) and posterior (15, 16) cerebral arteries. The two anterior cerebral arteries are represented by a single vessel (19). The vessel, 6bis, is a peripheral resistance which may represent either the vertebrobasilar vascular system of the brain stem and the cerebellum or a complementary drainage pathways to the jugular veins. The three following tubes are regrouped into equivalent tubes of the principal collaterals of the cerebral arteries (20), the pial network (21) and the intracerebral arteries (22). Tube 23 represent the microcirculation. It includes the terminal arterioles, the pre-capillaries, the capillaries and the venulas. Tubes 24 and 25 depict respectively the intracerebral and pial veins. Vessels 26, 27, 29 and 31 portray a group of veins draining into the major sinuses 28, 30 and 32. Finally, they ultimately drain into the jugular veins (33, 34). Model data, including cross-section, length, number of vessels for the equivalent tubes and elastance are shown in table (3.1). In the work of Zagzoule and Marc Vergnes [73], the lengths, cross-sections and the number of vessels were taken from the litterature when they were available [32, 39, 1] . The blood volume of the carotid arteries, the vertebral arteries and the circle of Willis is 13.03 mL. For the arterial system after the circle of Willis, it is set to 43.187 mL. The microcirculation volume is 19.36 mL and finally the venous system volume is 96.04 mL.

Geometric assumptions and simplifications that were implemented to design this model are discussed in [73].

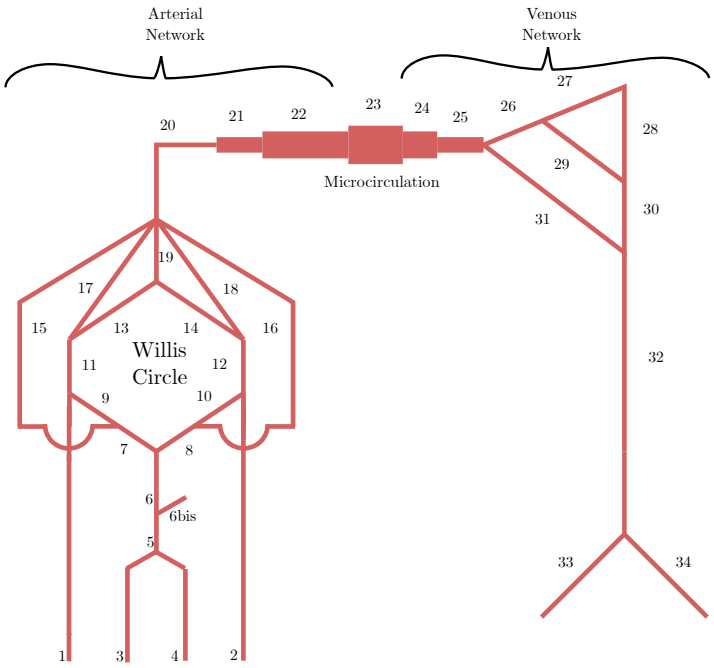

Figure 3.2: The 1d model from Zagzoule and Marc Vergnes [73]

3.3 Subarachnoid spaces

Figure (3.3) displays the architecture of the coupled 1d blood-csf model. As described previously, red vessels depicts the cerebral vasculature ranged from vessel 1 to 34. Blue vessels depict the coaxial cranial subarachnoid tubes, they are coaxial to blood vessels starting from bifurcations (11-9), (7-8) and (10-12) to the transverse sinus vessel 32. Therefore, the carotid arteries 1 and 2, the vertebral arteries 3 and 4 and the jugular veins 33 and 34 are not directly coupled to the cranial subarachnoid spaces. Orange tubes depicts the spinal subarachnoid spaces and the lumbar cistern vessels enclosing in grey area the spinal cord tube. The inlet of the spinal subarachnoid spaces is assumed to be the cervical C2-C3 CSF area. Finally green areas represent subarachnoid spaces tubes that link the cranial ones to the spinal ones. They will be referred in this work as the cranio-cervical junction tubes. Dashed black circles display the branching interfaces between the different vessels, they will be discussed in the next chapter.

3.3.1 Cranial subarachnoid spaces

As explained previously, the dynamic coupling between a cerebral blood vessel and a cranial subarachnoid space was approached using a coupled coaxial tubes modelling. The inner tube accounts for a blood vessel, whereas the outer tube portrays the cranial subarachnoid space confined by the cranial dura mater.

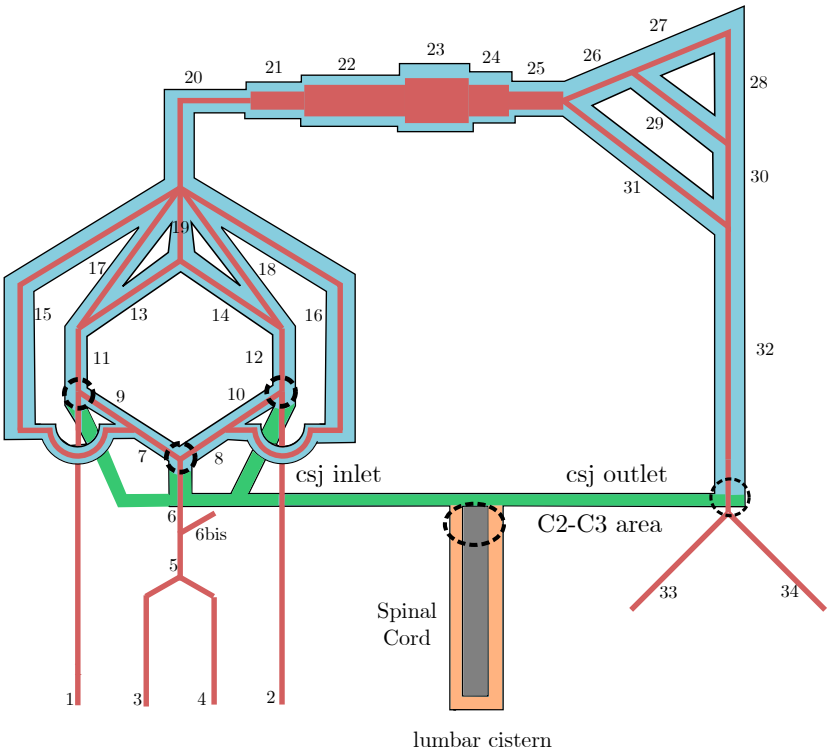

Figure 3.3: The 1d coupled blood-csf model. Red: blood vessels, blue: cranial subarachnoid spaces, orange: spinal subarachnoid spaces, green: CSF between the cranial and spinal vault, grey: the spinal cord. Dotted circles depict the branching interfaces between the cranial and the spinal vault

As mentioned previously, pulsatile CSF oscillations are believed to be driven by systolic vascular dilatation followed by diastolic contraction. In order to accurately model this coupling, some crucial questions have been raised in this study : which vascular vessels contribute the most to the pulsations of the cranial CSF flow and its displacement into the spinal canal ? Is it the arterial system by means of its strong pulsations ? What about the compliant venous system which blood volume is far greater than the arterial system ? Finally what about the parenchymal matter and the microcirculation system ?

Indeed, the main arteries running along the cortical surface, the pial arteries, are the closest to the cranial subarachnoid spaces. Thus, from a 'spatial' point a view, their pulsations may contribute the most to driving the CSF flow. Smaller penetrating arterioles or the microcirculation bed, embedded within the cerebral tissue may also distend. Their systolic expansion and thus their volumetric dilatation would need to be transmitted to the surrounding tissues and produce CSF motion [23, 24]. In a similar way, the bed capillary may contribute to CSF pulsations. In a first approach, we have chosen to enclose the entire global vasculature system within the cranial CSF. For this configuration, the major brain blood supply vessels, i.e the carotid, the vertebral arteries and the jugular veins vessels were not enclosed by the cranial CSF as they are located outside of the cranial vault.

A second important question was raised regarding the dimensions of the cranial subarachnoid spaces. In vivo, they have been measured by ultrasound (US), computed tomography (CT) and magnetic resonance imaging (MRI) mainly in neonates and infants as it may be a marker for the development of several neuropsychatric diosorders. Their width have been acquired between the cranium and the cerebral hemisphere, refered as the craniocortical distance and between the two hemispheres. Studies have shown variable upper limits for the craniocortical distance width rangin from 3.3 to 5 mm in neonates [25, 47, 49] to 4 to 10 mm in infants and adults [57, 38, 40, 33].

In this study, the sections of the cranial subarachnoid spaces were defined as follows: A dimensionless parameter referred as CSF confinement and denoted λ, is defined as the ratio between the sections of a blood vessel and a cranial sas.

$$0.1 < \lambda_{cb} = \frac{A_{bi}}{A_{ci}} < 0.85 \quad \text{for i=6,. . . , 32.} \tag{3.1}$$

where A_{bi} and A_{ci} are respectively the sections of a blood vessel of the cv and a tube of the cranial sas i.

For example, figure (3.4) illustrates at a full scale three values of cranial CSF confinement, λ_{cb} (0.1, 0.5 and 0.85), for a blood vessel, of 0.5 cm. As λ_{cb} increases from 0.1 towards 0.85, the annular CSF space and its volume, in blue, decreases.

The cranial CSF confinement was assigned a constant value along the cerebral vasculature. For example a cranial CSF confinement of $\lambda_{cb} = 0.7$ implies following equation (3.1) :

- For the posterior cerebral arteries (15, 16), a cranial subarachnoid vessel of $\frac{0.07}{0.7} = 0.1$

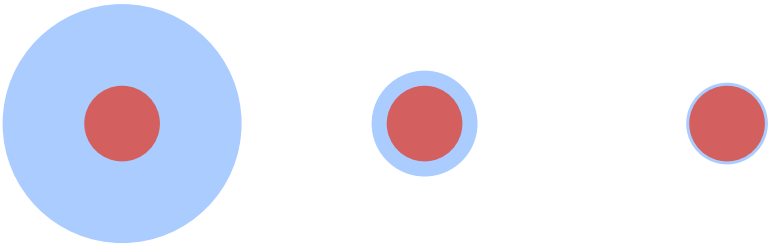

$\lambda_{cb} = 0.1$ $\lambda_{cb} = 0.5$ $\lambda_{cb} = 0.85$

Figure 3.4: Cranial subarachnoid space at full-scale for three values of cranial CSF confinement λ_{cb}

cm^2 and therefore an annular CSF space area of $0.1 - 0.07 = 0.03$ cm^2,

- For the middle cerebral arteries (17, 18), a cranial subarachnoid vessel of $\frac{0.12}{0.7} = 0.17$ cm^2 and therefore an annular CSF space area of $0.17 - 0.12 = 0.05\text{cm}^2$.

As the cranial CSF confinement varies between 0.1 and 0.85, cranial CSF volume varies beteween 85 mL and 1400 mL.

3.3.2 Spinal subarachnoid spaces

In a similar manner, the spinal compartment was modeled as two coaxial tubes in which the inner tube represents the spinal cord enclosed by the spinal pia mater and the outer tube represents the spinal subarachnoid space (SSS) enclosed by the spinal dura mater. Since, we are mainly interested in the CSF fluid transport in the spinal sas, the spinal cord was considered as well a CSF-fluid filled tube.

We used a geometric coaxial tube in which the spinal cord and the spinal sas were held constant along the spinal cord. Sections and length were partially based on the previously published FE-FSI models of the spinal cavity [8, 7]. Spinal cord and SSS sections were taken respectively equal to $A_{SSS} = 1.6$ cm^2 and $A_{SSS} = 0.78$ cm^2 yielding to a spinal CSF volume of 68 mL. Moreover, the spinal subarachnoid space length was taken longer, $A_{SSS} = 70$ cm, than the spinal cord, $A_{SC} = 50$ cm to account for the lumbar cistern.

Figure (3.5) depicts the cranial and spinal CSF volume for λ_{cb} values ranging between 0.1 (a cranial CSF volume of 1400 mL) and 0.85 (a cranial CSF volume of 95 mL). As stated previously, spinal CSF volume was assumed constant and equal to 68 mL.

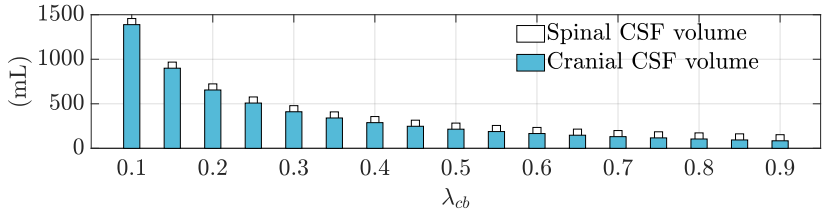

Figure 3.5: CSF volume (mL) for $0.1<\lambda_{cb}<0.85$

3.4 Cranio-spinal compliance

3.4.1 Elastic modulus of the dura mater

The mechanical compliance is the ability of a compartment to accomodate a change in volume for a corresponding change in pressure. The overall cranio-spinal compliance is of special interest in understanding regulation of the intracranial pressure and is determined by adding the cranial and spinal compartments compliance. It is expected from anatomic consideration, that both compliance contributes differently to the overall cranio-spinal compliance. From an anatomical point of view, the spinal vault would contribute largely as the spinal CSF is less confined by rigid structures than in the cranial vault. In vitro biomechanical charaterisation performed by several authors has demonstrated a highly nonlinear behaviour with a longitudinal and transverse Young's modulus from 1.4-105 MPa (10^4 - 8.10^5 mmHg) and 0.08-7 MPa (6.10^2 - 5.10^4 mmHg) respectively[27, 54, 62, 45, 14, 18].

In previous numerical models, the dura mater was considered as a linear elastic material model. Bertram et al.[9] and Cirovic et al. [15] have chosen the elastic modulus of the dura mater to approximate the spinal sas wave speed measured by MRI. It was set equal to 1.25 MPa (9.10^3 mmHg). The spinal dura mater was also investigated by several authors [10, 46, 52] and showed an elastic Young's modulus varying from 1-2.3 MPa ($7.5\ 10^3$ - $1.7\ 10^4$ mmHg).

In this work, the dura mater and the spinal pia mater were as well represented by a longitudinal Young's modulus.

3.4.2 The lumbar cistern compliance

The lumbar segment was terminated by a 3 elements Windkessel model described in figure (3.6). It was assigned a volumetric compliance C_lw , the proximal resitance R_1 is introduced to absorb the incoming waves and reduce artificial wave reflections and The distal resistance R_2 was taken high to limit CSF outflow from the lumbar segment.

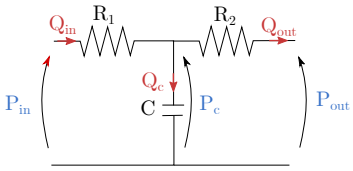

Figure 3.6: Three elements $R_1R_2C_lw$ Windkessel model

Chapter 4

The 1D flow equations in a system of coaxial tubes

Sommaire

4.1 Introduction

In this chapter, we first establish the 1D model of governing equations for single and coaxial tubes. The 1D blood-CSF model is composed of two geometric configurations, either single tubes such as the internal carotids arteries or coaxial tubes such as the coupled blood vessel and cranial sas vessel. The one dimensional formulation of compliant vessels is well established and widely used in biomechanics. Hereby, we just recall the main outlines. A detailed construction of one-dimensional model can be found in [12]. Second, we describe the Lax Wendroff numerical scheme employed to discretize the governing equations. In the third section, we present the boundary conditions and finally in the fourth section, we implement a method to account for branching or interface conditions such as bifurcations.

4.2 Mathematical Formulation

In a system of cylindrical coordinates (r, θ, z), the domain geometry is illustrated in figure (4.1). It exemplifies a portion of a coupled vessel of blood and subarachnoid space. The subscript **1**

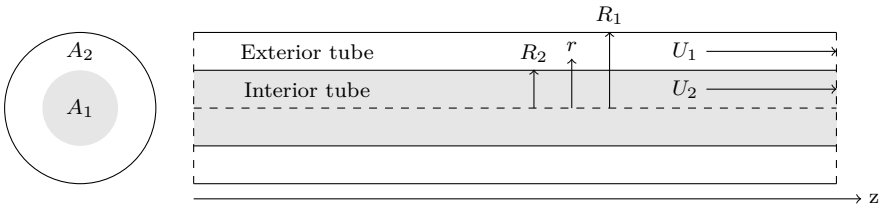

Figure 4.1: A one dimensional coaxial tubes where the inner tube represents a blood vessel and the outer tube a cranial sas where CSF flows

denotes a single tube or an interior one whereas the subscript **2** denotes the exterior (annular) tube. The axis of the vessels is aligned along the coordinate z. R_1 and R_2 are respectively the interior and exterior tube radius.

4.2.1 Main assumptions for the fluid flow and the wall motion

Blood was considered newtonian having respectively a dynamic viscosity $\mu_b = 0.035$ Poise ($g.cm^{-1}.s^{-1}$) and density $\rho_b = 1.06$ g/mL. CSF was assumed close to water having dynamic viscosity $\mu_c = 10^{-2}$ Poise and $\rho_b = 1$ g/mL.

The one dimensional model for incompressible and newtonian fluid flow in a compliant vessel may be derived from the Navier Stokes equations, under the following simplifying hypotheses.

When accounting for the fluid flow:

- *Axial Symmetry*, the dependance on θ is completely neglected. This implies that each axial section at a fixed z position remains circular at all times. We thus neglect any eventual collapse of the tube. Therefore, the vessel radius, R_1 (R_2), is solely function of z and t.
- *Constant pressure in a cross section*, the pressure is taken to be constant on each axial section, so that it depends only on z and t.
- *No body forces*, such as gravity.
- *Dominance of axial velocity*, the velocity components orthogonal to z axis are negligible compared to the component along z. This consideration is sometimes called the **Long Wave-Length Approximation.**

When accounting for the vessel structure:

- *Radial displacement*, the wall moves solely in the radial direction.
- *Wall thickness*, the effective wall thickness is relatively small and can be treated as a membrane.

- *Small deformations gradients.* We consider that the deformations gradients are relatively small, so that the structure behaves like a linear elastic solid.

4.2.2 3D Navier Stokes equations for incompressible fluids

Remarque 4.1
Vectors are indicated using bold letters while their components will be denoted by the same letter in normal typeface.

In Fluid mechanics, the fluid flow is governed by the following 3D incompressible Navier-Stokes equations,

$$\begin{cases} \boldsymbol{\nabla}.\boldsymbol{u} = 0, & (4.1) \\ \rho[\dfrac{\partial \boldsymbol{u}}{\partial t} + \boldsymbol{u}.\boldsymbol{\nabla}\boldsymbol{u}] + \boldsymbol{\nabla}.[p\mathbb{I} - \overline{\overline{\tau}}] = 0, & (4.2) \end{cases}$$

The unknowns are the fluid velocity $\boldsymbol{u} = (u_r, u_\theta, u_z)$, the pressure p and the shear stress tensor $\overline{\overline{\tau}}$. Due to the axisymmetric assumption, the shear stress tensor is defined as:

$$\overline{\overline{\tau}} = \begin{pmatrix} \tau_{rr} & 0 & \tau_{rz} \\ 0 & \tau_{\theta\theta} & 0 \\ \tau_{rz} & 0 & \tau_{zz} \end{pmatrix}$$

where $\mathbb{I}$ is the identity matrix.

Using the assumptions established previsouly, the 3D incompressible Navier-Stokes equations are reduced to the following system of equations ,

$$\begin{cases} \dfrac{1}{r}\dfrac{\partial(ru_r)}{\partial r} + \dfrac{\partial(u_z)}{\partial z} = 0, & (4.3) \\ \dfrac{\partial u_z}{\partial t} + u_r\dfrac{\partial u_z}{\partial r} + u_z\dfrac{\partial u_z}{\partial z} + \dfrac{1}{\rho}\dfrac{\partial p}{\partial z} = \dfrac{1}{\rho r}\dfrac{\partial(r\tau_{rz})}{\partial r}, & (4.4) \\ p = p(z,t), & (4.5) \end{cases}$$

where τ_{rz} is the wall shear stress defined as,

$$\tau_{rz} = \mu\frac{\partial u_z}{\partial r} \quad (4.6)$$

4.2.3 1D reduced Navier Stokes equations for a single or interior vessel

Remarque 4.2
*Subscript **1** is used for the inner tube whereas subscript **2** describes the outer tube.*

By integrating the reduced Navier-Stokes equations (4.3) and (4.4) on a generic axial section and taking advantage of the above assumptions, one obtains the following set of two partial differential equations,

$$\begin{cases} \dfrac{\partial A_1}{\partial t} + \dfrac{\partial Q_1}{\partial z} = 0, & (4.7) \\ \dfrac{\partial Q_1}{\partial t} + \dfrac{\partial}{\partial z}\left(\beta \dfrac{Q_1^2}{A_1}\right) + \dfrac{A_1}{\rho}\dfrac{\partial P_1}{\partial z} = \dfrac{2\pi}{\rho}\sqrt{\dfrac{\pi}{A_1}}\tau_{rz}|_{r=R_1}, & (4.8) \end{cases}$$

where P_1(z,t) is the mean pressure. A_1(z,t) and Q_1(z,t) denotes respectively the section area and the average volumetric flow. They are defined as,

$$A_1(z,t) = 2\pi \int_0^{R_1} r\mathrm{d}r, \qquad Q_1(z,t) = 2\pi \int_0^{R_1} u_z r\mathrm{d}r, \tag{4.9}$$

whereas β is a momentum correction factor defined as,

$$\beta(z,t) = 2\pi \frac{A_1}{Q_1^2} \int_0^{R_1} r u_z^2 \mathrm{d}r \tag{4.10}$$

The system of equations can be expressed alternatively in terms of variables (A_1, U_1, P_1). By simple manipulations, one gets,

$$\begin{cases} \dfrac{\partial A_1}{\partial t} + \dfrac{\partial (AU)_1}{\partial z} = 0, & (4.11) \\ \dfrac{\partial U_1}{\partial t} + \dfrac{U_1}{A_1}(1-\beta)\dfrac{\partial A_1}{\partial t} + \beta U_1 \dfrac{\partial U_1}{\partial z} + \dfrac{1}{\rho}\dfrac{\partial P_1}{\partial z} = \dfrac{2}{\rho}\sqrt{\dfrac{\pi}{A_1}}\tau_{rz}|_{r=R_1}, & (4.12) \end{cases}$$

On the one hand, the wall shear stress, τ_{rz}, as defined in (4.6) is a function of the velocity profile. A simple case of parabolic profile is assumed for this term. Therefore, we obtain,

$$\tau_{rz}|_{r=R_1} = \mu \frac{\partial u_z}{\partial r}|_{r=R_1} = -4\mu \frac{U_1}{R_1} \tag{4.13}$$

where $u_z = 2U_1 \left(1 - \frac{r^2}{R_1^2}\right)$.

On the other hand, the coefficient β, as defined in (4.10) is likewise a function of the velocity profile.
For a flat profile, $\beta = 1$ whereas for a parabolic profile $\beta = \frac{4}{3}$. We have here considered the choice $\beta = 1$ since it leads to considerable mathematical simplifications. Furthermore, previous work by Doulfoukar et al. [20] shows that even in the aorta β fluctuates around 1. Other types of profiles for the viscous term and the correction factor may be used [67, 66].

Finally, as the number of unknowns (P_1, A_1, U_1) exceeds the number of equations, we need to use an additional constraint in order to close this system. A common way to close the system is to explicitly provide an algebraic relationship, known as *the tube law*, which links the average section A_1 to the average transmural pressure P_t. The transmural pressure P_t is defined as,

$$(P_t)_1 = P_1 - P_{ext} \tag{4.14}$$

where P_{ext} is the pressure exerted to the vessel by its external environment (as external tissues or CSF). Depending on the geometry configuration, for a single or an external vessel, P_{ext} is taken constant, whereas for the interior tube of a coaxial vessel, P_{ext} is taken equal to the pressure of the external vessel.

Here we consider the case of a linear elastic tube law defined as,

$$(P_t)_1 = (E_l)_1 \left(\frac{A_1}{(A_0)_1} - 1\right), \tag{4.15}$$

where $(A_0)_1$ is the vessel area at zero transmural pressure and $(E_l)_1$ is a constant elastic Young's modulus. We thus neglect any eventual collapse of the tube, althoug this can be taken into account through a suitable tube law [55].
Moreover variations of the elastic properties of the wall, not treated in the present study, may be considered by letting the elastic Young's modulus $(E_l)_1$ be a function of the vessel area A_1. It may either simulate the different microanatomical features of the wall or consider the presence of a vascular prothesis like a stent implantation [58].

4.2.4 1D reduced Navier-Stokes equations in a system of coaxial tubes

Upon the simplifications taken above, the system of equations (4.7) and (4.8) become,

For a single or interior vessel ,

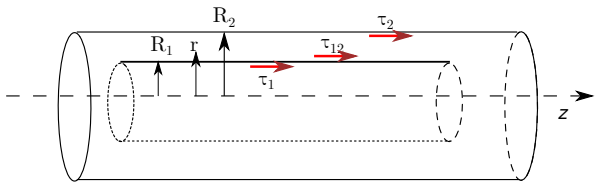

Figure 4.2: Wall shear stresses in a coaxial configuration

$$\begin{cases} \dfrac{\partial A_1}{\partial t} + \dfrac{\partial (A_1 U_1)}{\partial z} = 0, & (4.16) \\ \dfrac{\partial U_1}{\partial t} + U_1 \dfrac{\partial U_1}{\partial z} + \dfrac{1}{\rho}\dfrac{\partial P_1}{\partial z} = \dfrac{2}{\rho}\sqrt{\dfrac{\pi}{A_1}}\tau_1, & (4.17) \\ P_1 = (E_l)_1 \left(\dfrac{A_1}{(A_0)_1} - 1 \right) + P_2, & (4.18) \end{cases}$$

where,

$$\tau_1 = \mu \frac{\partial u_z}{\partial r} = -4\mu \frac{U_1}{R_1} \tag{4.19}$$

We recall that some vessels as the cerebral arteries (20), the pial network (21) and the intracerebral arteries (22) were regrouped into equivalent tubes. For example, the microcirculation (23) was represented by $N = 202000$ vessels having a total cross section area $A_1 = 38$ cm^2. The friction term of the right hand side of the momentum equation 4.17, referred as F_1 was therefore expressed in terms of the total cross-section area A_1 and the number of regrouped vessels N as follows,

$$F_1 = \frac{2}{\rho}\sqrt{\frac{\pi}{A_1}}\tau_1 = -N\frac{8\pi\mu}{\rho_1}\frac{U_1}{A_1} \tag{4.20}$$

For an annular vessel ,

$$\begin{cases} \dfrac{\partial A_2}{\partial t} + \dfrac{\partial U_2 (A_2 - A_1)}{\partial z} + \dfrac{\partial (U_1 A_1)}{\partial z} = 0 & (4.21) \\ \dfrac{\partial U_2}{\partial t} + U_2 \dfrac{\partial U_2}{\partial z} + \dfrac{1}{\rho}\dfrac{\partial P_2}{\partial z} = -\dfrac{2\sqrt{\pi}}{\rho(A_2 - A_1)}(\tau_{12}\sqrt{A_2} - \tau_2\sqrt{A_1}) & (4.22) \\ P_2 = (E_l)_2 \left(\dfrac{A_2}{(A_0)_2} - 1 \right) + P_{ext}, & (4.23) \end{cases}$$

where P_{ext} is taken constant for the annular space.
τ_{12} and τ_2 are respectively the wall shear stresses at $r = R_1$ and $r = R_2$ due to the flow of the annular fluid as displayed in figure (4.2).

A detailed construction of these wall shear stresses is given in Appendix (A). They are

defined as,

$$\begin{cases} \tau_{12} = \dfrac{2\mu U_2}{\gamma}\left(\dfrac{2R_1}{R_2^2} + \dfrac{1-\lambda^2}{R_1 \ln \lambda}\right) & (4.24) \\ \tau_2 = \dfrac{2\mu U_2}{\gamma}\left(\dfrac{2}{R_2} + \dfrac{1-\lambda^2}{R_2 \ln \lambda}\right) & (4.25) \end{cases}$$

where

$$\begin{cases} \gamma = 1 + \lambda^2 + \dfrac{1-\lambda^2}{\ln \lambda} & (4.26) \\ \lambda = \dfrac{R_1}{R_2} & (4.27) \end{cases}$$

Waves equations The relation between the pressure and area defines the intrinsic wave speed in a single, c_{01}, and a coaxial tube, c_{02} as follows

$$c_1 = \sqrt{\frac{A_1}{\rho_1}\frac{\mathrm{d}(P_1 - P_2)}{\mathrm{d}A_1}}, \qquad c_2 = \sqrt{\frac{A_2}{\rho_2}\frac{\mathrm{d}P_2}{\mathrm{d}A_2}} \tag{4.28}$$

Using (4.18) and (4.23), these wave speeds become

$$c_1 = \sqrt{\frac{(E_l)_1}{\rho_1}}, \qquad c_2 = \sqrt{\frac{(E_l)_2}{\rho_2}} \tag{4.29}$$

The analytical expressions of the waves modes resulting from the coupled system were given by Cirovic et Kim [15] as follow,

$$c_{1,2}^2 = \frac{1}{2}(c_s^2 + c_c^2) \pm \sqrt{\left(\frac{1}{2}(c_s^2 + c_c^2)\right)^2 - \alpha_{cs} c_s^2 c_c^2} \tag{4.30}$$

where $\alpha_{12} = 1 - \dfrac{A_1}{A_2}$.

4.3 Numerical scheme: the two steps Lax-Wendroff scheme

The numerical method used to solve the previous hyperbolic partial differential equations is the classical Lax-Wendroff finite difference schemes. This scheme is second-order accurate in space and time. It must satisfy the Courant-Friedrich-Lewy (CFL) criterion,

$$\frac{\delta x}{\delta t} > (U + c_0)$$

where c_0 is the speed of wave propagation defined in section 4.2.4 and U is the mean velocity.

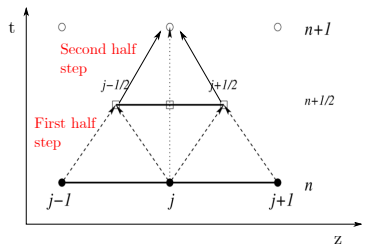

Figure 4.3: The Lax-Wendroff numerical scheme

Figure (4.3) displays the Lax-Wendroff numerical scheme. Each point $M(z_j, t^n)$ in the discretized spacetime grid (z, t) will have spatial and time coordinates defined by $z_j = j\Delta z$ and $t = n\Delta t$ where Δt is the time increment and Δz is the spatial increment.

First half step At the first half step, the system of equations is derived at the point $(j + \frac{1}{2}, n)$, to obtain the values of the section A and velocity U for half time step and half step grid $(j \pm \frac{1}{2}, n + \frac{1}{2})$

Continuity equation :

$$(A_1)^{n+1/2}_{j+1/2} = \frac{(A_1)^n_j + (A_1)^n_{j+1}}{2} - \frac{\Delta t}{2\Delta z}\left((A_1U_1)^n_{j+1} - (A_1U_1)^n_j\right)$$

Momentum equation :

$$(U_1)^{n+1/2}_{j+1/2} = \frac{(U_1)^n_j + (U_1)^n_{j+1}}{2} - \frac{\Delta t}{2\Delta z}\left(\left(\frac{U_1^2}{2} + \frac{P_1}{\rho}\right)^n_{j+1} - \left(\frac{U_1^2}{2} + \frac{P_1}{\rho}\right)^n_j\right) + \frac{\Delta t}{2}F^n_{j+1/2}$$

where

$$F^n_{j+1/2} = \frac{-2}{\rho}\sqrt{\pi}\left(\left(\frac{\tau_1}{\sqrt{A_1}}\right)^n_{j+1} + \left(\frac{\tau_1}{\sqrt{A_1}}\right)^n_j\right)$$

Tube law equation :

$$(P_1)^{n+1/2}_{j+1/2} = E_1\left(\frac{(A_1)^{n+1/2}_{j+1/2}}{(A_{10})_j} - 1\right) + (P_1)^{n+1/2}_{j+1/2}$$

Second half step At the second half step, the latter equations are derived at the point $(j, n + \frac{1}{2})$ to obtain the values of the section A and velocity U at $(j, n + 1)$.

Continuity equation :

$$(A_1)_j^{n+1} = (A_1)_j^n - \frac{\Delta t}{\Delta z}\left((A_1U_1))_{j+1/2}^{n+1/2} - (A_1U_1)_{j-1/2}^{n+1/2}\right)$$

Momentum equation :

$$(U_1)_j^n = (U_1)_j^n - \frac{\Delta t}{\Delta z}\left(\left(\frac{U_1^2}{2} + \frac{P_1}{\rho}\right)_{j+1/2}^{n+1/2} - \left(\frac{U_1^2}{2} + \frac{P_1}{\rho}\right)_{j-1/2}^{n+1/2}\right) + \Delta t F_j^{n+1}$$

where

$$F_j^{n+1} = \frac{-2}{\rho}\sqrt{\pi}\left(\left(\frac{\tau_1}{\sqrt{A_1}}\right)_{j+1/2}^{n+1/2} + \left(\frac{\tau_1}{\sqrt{A_1}}\right)_{j-1/2}^{n+1/2}\right)$$

Tube law equation :

$$(P_1)_j^{n+1} = E_{lc}\left(\frac{(A_1)_j^{n+1}}{(A_{10})_j} - 1\right) + (P_s)_{j+1/2}^{n+1/2}$$

4.4 Boundary conditions

Proper initial and boundary conditions are needed to finalize our mathematical formulation. Initial conditions do not have impact on the final solution as after a few simulations, the results did converge to a periodic state. At the cv, the boundary conditions consists of either the pressure since the area and pressure are related to each other by the tube law constitutive relationship or the velocity (flow). They are imposed at the inlet of the cv, i.e the paired carotid and vertebral arteries and the outlet of the cv, i.e the paired jugular veins.

In the theoretical and next chapter three, a time dependent pressure function was specified as an inflow and an outflow boundary conditions whereas in chapter five, a time dependant flow waveform driven from MRI velocites data was specified as inflow and an outflow boundary conditions.

For instance, in the case of a pressure inflow boundary condition P_1, the numerical boundary condition is written as,

$$(U_1)_0^{n+1} = (U_1)_0^n - \frac{\Delta t}{\Delta z}\left(\left(\frac{U_1^2}{2} + \frac{P_1}{\rho}\right)_1^n - \left(\frac{U_1^2}{2} + \frac{P_1}{\rho}\right)_0^n\right) + \Delta t F_0^n \tag{4.31}$$

where subscript 0 denotes the entry and subscript 1 is the point Δz distant from it.

Pressure inflow and outflow boundary conditions Following figure (4.4), a constant pressure of 5.832 mmHg, $P_b(outlet)$, is imposed at the outlet of the cerebral vasculature, i.e at the outlet of the jugular veins number 33 and 34.

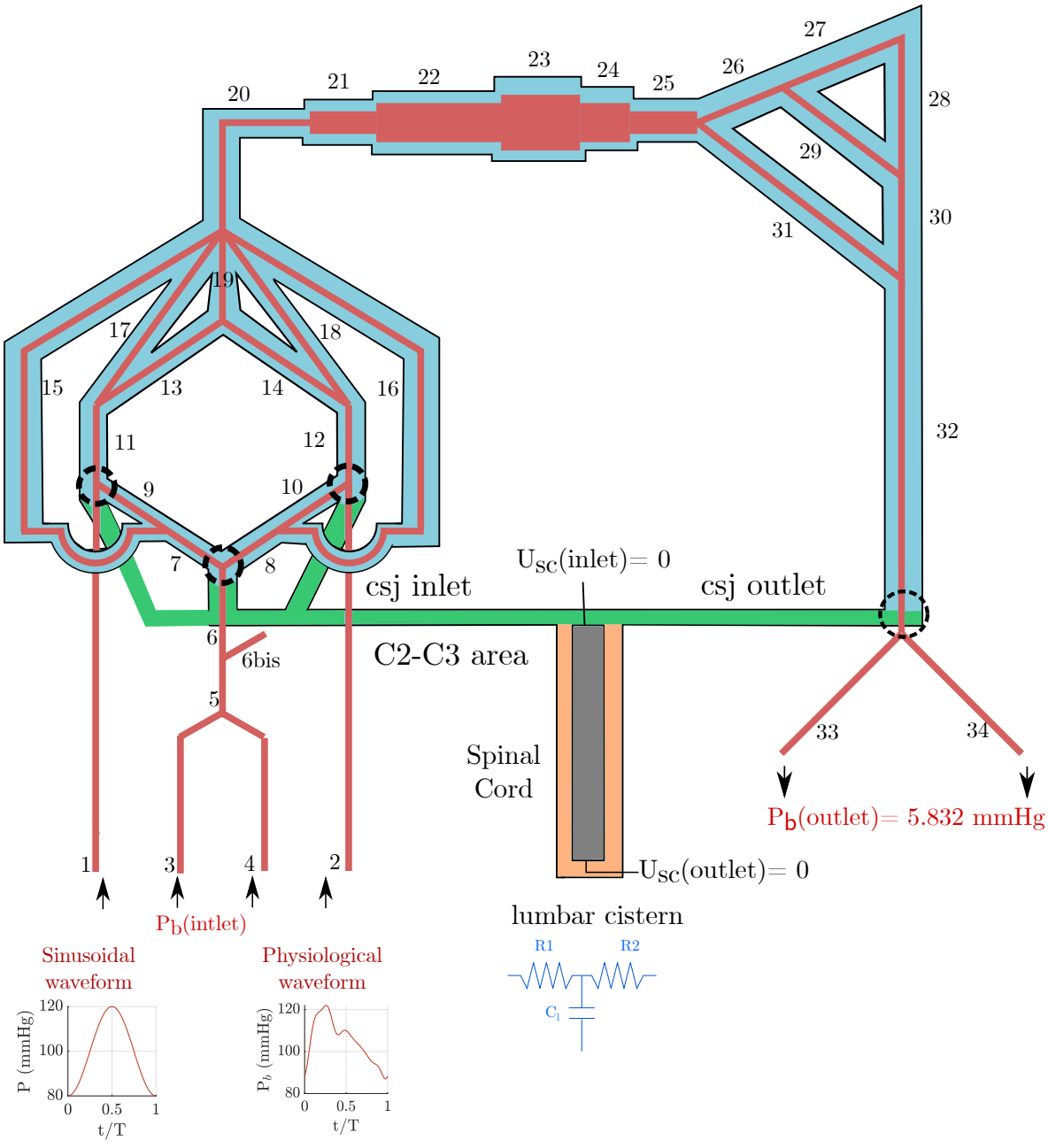

Figure 4.4: Boundary conditions of the 1D blood-CSF network

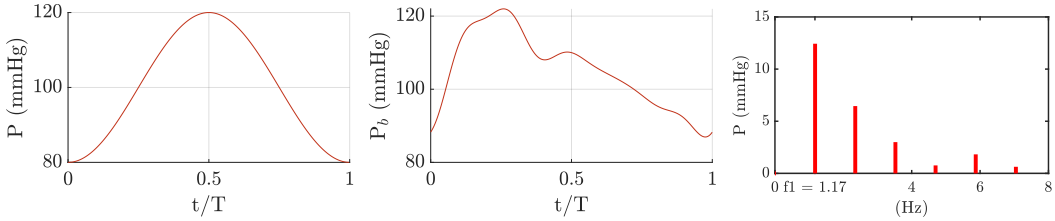

(a) A sinusoidal arterial pressure signal

(b) A physiological arterial pressure signal

(c) Fourier transform illustrating the first six harmonics

Figure 4.5: Pressure signals imposed at the inlet of the blood vascualture. Two waveforms are considered : a sinusoidal and a physiological one

A pressure signal, $P_b(inlet)$, is imposed at the inlet of the cerebral vasculature, i.e at the inlet of the carotid arteries 1 & 2 and the vertebral arteries 3 & 4. Two pressure waveforms have been considered :

- First, to model in the simplest way the arterial pressure, a sinusoidal arterial waveform, illustrated figure (4.5a), for one period of $T = 0.85$ s, a mean pressure of 100 mmHg, a systolic pressure of 120 mmHg and a diastolic one of 80 mmHg.

- Second, a physiological arterial waveform, illustrated figure 4.5b, for one period of $T = 0.85$ s, a mean pressure of 105.5 mmHg, a systolic pressure of 121.5 mmHg and a diastolic one of 87.15 mmHg.
  This waveform is obtained via Fourier decomposition, using *fft* matlab function, of a discrete signal acquired from [73] and re-sampled using the first six harmonic. We have considered that higher frequencies beyond the sixth harmonic did not add very much to the shape of the pulse waveform.

  Figure 4.5c displays the amplitude spectrum of these first six harmonics. The fundamental frequency is the heart rate $f_1 = 1.176$ Hz ($T = 0.85$ or 70 bpm). For a scale matter, the mean pressure value of 105.5 mmHg at zero Hz frequency is not plotted. This signal may be discretized with a Fourier series following :

$$P_1 = a_0 + \sum_{i=1}^{6} a_i \cos(iwt) + b_i \sin(iwt) \tag{4.32}$$

  where w is the signal pulsation, $w = \dfrac{2\pi}{T}$, and t is the time scale. The value index zero, a_0, corresponds to the mean value. Fourier coefficients a_i, b_i are listed in table (4.1). Twelve terms were used.

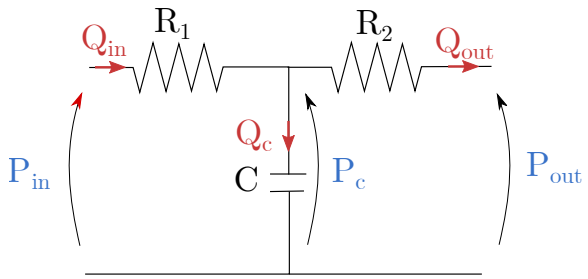

Figure 4.6: Three elements $R_1R_2C_lw$ Windkessel model

Coefficient	Value (mmHg)
a_0	105.5
a_1	-6.122
b_1	10.54
a_2	-5.025
b_2	3.867
a_3	-2.815
b_3	-0.7914
a_4	-0.5171
b_4	0.5097
a_5	-1.846
b_5	0.1619
a_6	-0.3149
b_6	-0.4563

Table 4.1: Mean value, a_0 and Fourier coefficients a_i, b_i, $i = 1, 2, ..., 6$ of (4.32) which captures the arterial pulsation

The lumbar terminal three elements Windkessel model A zero-dimensional (0-D) approach model governed by ordinary differential equations is used to relate pressure to flow at the outflow of the lumbar cistern using a three elements Windkessel model described in figure (4.6) where the proximal resitance R_1 is introduced to absorb the incoming waves and reduce artificial wave reflections. It corresponds to the characteristic impedance Z_l of lumbar vessel to match the propagation of forward travelling waves and defined as,

$$c_l = \sqrt{\frac{E_l u}{\rho_b}}, \quad Z_l = \rho \frac{c_l}{A_{0l}}$$

where c_l is the intrinsic lumbar segment wall wave speed, ρ_b the CSF density, $E_l u$ the lumbar segment elastic modulus and A_{0l} the lumbar segment cross sectional area at zero transmural pressure.

In the analogous electrical circuit described figure (4.6), Q_{in}, Q_{out} defines respectively the input flow and output flow rate due to proximal resistance R_1 and distal resistance R_2

whereas Q_c defines the flow rate of the capacitance C, P_{in}, P_{out} and P_c are respectively the inlet pressure, output pressure and capacitance pressure. The inlet and output flows Q_{in} and Q_{out} may be described following Ohm's low as,

$$Q_{in} = \frac{P_{in} - P_c}{R_1}, \qquad Q_{out} = \frac{P_c - P_{out}}{R_1} \tag{4.33}$$

Kirhoff's law states that $Q_{in} = Q_c + Q_{out}$ and finally the capacitance pressure is defined as,

$$\frac{\mathrm{d}P_c}{dt} = \frac{Q_c}{C} \tag{4.34}$$

A first order time discretization of the previous set of equations is written as,

$$\begin{cases} A_{in} = A_0^L - \dfrac{\Delta t}{\Delta x}\left((AU)_L^n - (AU)_{L-1}^n\right), & (4.35) \\ P_{in} = E_l(\dfrac{A_{in}}{A_{0in} - 1}), & (4.36) \\ Q_{in}^n = \dfrac{P_{in} - Pc^n}{R1}, & (4.37) \\ Q_{out}^n = \dfrac{Pc^n - Pout}{R2}, & (4.38) \\ Pc^{n+1} = Pc^n + \Delta t \dfrac{Q_{in}^n}{Q_{out}^n}, & (4.39) \\ Q_{in}^{n+1} = \dfrac{P_{in} - Pc^{n+1}}{R1}, & (4.40) \\ U_{in} = Q_{in}^{n+1}/A_{in} & (4.41) \end{cases}$$

where P_{out} is a constant pressure that was assumed equal to a mean intracranial pressure of 10 mmHg and $Pc^n = 0$ at the inital time step n=1.

4.5 Branching conditions

The 1D craniospinal model is characterized by the presence of branching. In this section, we will address the problem of accounting for interface conditions.

Several configurations are found in the geometry structure as modeled in figure (4.4) and detailed in B such as,

- *A bifurcation of vessels*, when a single (or coaxial) vessel bifurcates into two single (or coaxial vessels). For instance, between vessels 25, 26 and 31.
- *A junction of vessels* occurs when two single (or coaxial) vessel join into one single (or coaxial) vessel. For instance, between vessels 31, 30 and 32.
- Finally *an enlargement (or reduction) of vessels*, defines a branching between two single

(or coaxial) vessels of different cross-sectional areas. For instance, between vessels 20 and 21.

The flow in a branching configuration is intrinsically three-dimensional; yet it may still be represented by means of a 1D model. In a first stage we simplify the actual geometric structure by imposing that the branching is located exactly at one point and neglecting the effect of branching angles.

In the following formulation, we will only address the case of a widening or a narrowing of tubes. However, the methodology employed here is extended as well to the cases of a junction, enlargement or reduction of vessels in a single or coaxial configuration and moreover to the branching interfaces between the cerebral vasculature, the cranio-cervical junctions and the spinal subarachnoid spaces.

The following subscripts are used : 1 for the interior tube and 2 for the exterior tube.

case 1 : A widening or a narrowing of tubes

Interior tube

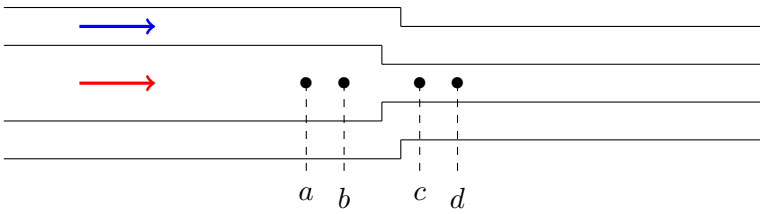

For the interior tube, the jump conditions between the points b and c are :

$$(AU)_{1b} = (AU)_{1c} \tag{4.42}$$

$$P_{1b} = P_{1c} \tag{4.43}$$

$$P_{1b} = El_{1b}\left(\frac{A_{1b}}{A_{01b}} - 1\right) + P_{2b} \tag{4.44}$$

$$P_{1c} = El_{1c}\left(\frac{A_{1c}}{A_{01c}} - 1\right) + P_{2c} \tag{4.45}$$

The equations (4.42) and (4.43) express the conservation of mass and pressure between b et c. We have 6 unkown terms and and we only have 4 equations. To complete this system, the conservation of mass equation was derived between a et b then between c et d :

$$\int_a^b \frac{\partial A_1}{\partial t}\mathrm{d}x + (AU)_{1b}^{n+1} - (AU)_{1a}^{n+1} = 0 \tag{4.46}$$

$$\int_c^d \frac{\partial A_1}{\partial t}\mathrm{d}x + (AU)_{1d}^{n+1} - (AU)_{1c}^{n+1} = 0 \tag{4.47}$$

The derivatives and integrals are evaluated using the difference finite method and the trapezoidal rule. Therefore, we obtain :

$$\frac{\Delta x_a}{2\Delta t_a}\left(A_{1a}^{n+1} - A_{1a}^{n} + A_{1b}^{n+1} - A_{1b}^{n}\right) + (AU)_{1b}^{n+1} - (AU)_{1a}^{n+1} = 0 \tag{4.48}$$

$$\frac{\Delta x_d}{2\Delta t_d}\left(A_{1d}^{n+1} - A_{1d}^{n} + A_{1c}^{n+1} - A_{1c}^{n}\right) + (AU)_{1d}^{n+1} - (AU)_{1c}^{n+1} = 0 \tag{4.49}$$

Using the equations (4.43), (4.44) and (4.45) and the pressure jump conditions of the exterior tubes ($P_{2b} = P_{2c}$), we obtain :

$$A_{1c} = \frac{El_{1b}}{El_{1c}}\frac{A_{01c}}{A_{01b}}A_{1b} + A_{01c}\left(1 - \frac{El_{1b}}{El_{1c}}\right) \tag{4.50}$$

By writing equation (4.50) for A_{1c}^{n+1} and A_{1c}^{n}, we obtain:

$$A_{1c}^{n+1} - A_{1c}^{n} = \frac{El_{1b}}{El_{1c}}\frac{A_{01c}}{A_{01b}}(A_{1b}^{n+1} - A_{1b}^{n}) \tag{4.51}$$

Put,

$$R_a = \left(\frac{\Delta x_a}{2\Delta t_a}\right), \qquad R_d = \left(\frac{\Delta x_d}{2\Delta t_d}\right), \qquad K_{1bc} = \frac{El_{1b}}{El_{1c}}\frac{A_{01c}}{A_{01b}}$$

By replacing (4.51) in equation (4.49) and by taking into account the conservation of mass equation (4.42), we obtain by adding (4.48) and (4.49) :

$$A_{1b}^{n+1} = A_{1b}^{n} + \frac{(AU)_{1a}^{n+1} - (AU)_{1d}^{n+1} - R_a(A_{1a}^{n+1} - A_{1a}^{n}) - R_d(A_{1d}^{n+1} - A_{1d}^{n})}{R_a + R_d K_{1bc}} \tag{4.52}$$

Using the same procedure, we obtain U_{1b}^{n+1} by subtracting the equation (4.49) from the equation (4.48).

$$\begin{aligned} U_{1b}^{n+1} =& \frac{(AU)_{1a}^{n+1} + (AU)_{1d}^{n+1} - R_a(A_{1a}^{n+1} - A_{1a}^{n}) + R_d(A_{1d}^{n+1} - A_{1d}^{n})}{2A_{1b}^{n+1}} \\ & - \frac{(R_a - R_d K_{1bc})(A_{1b}^{n+1} - A_{1b}^{n})}{2A_{1b}^{n+1}} \end{aligned} \tag{4.53}$$

4.5.0.1 Exterior tube

For the exterior tube, the jump conditions between the points b and c are :

$$((A_2 - A_1)U_2)_b = ((A_2 - A_1)U_2)_c \tag{4.54}$$

$$P_{2b} = P_{2c} \tag{4.55}$$

$$P_{2b} = El_{2b}\left(\frac{A_{2b}}{A_{02b}} - 1\right) \tag{4.56}$$

$$P_{2c} = El_{2c}\left(\frac{A_{2c}}{A_{02c}} - 1\right) \tag{4.57}$$

As for the interior tube, the conservation of mass equation was derived between a et b then between c et d. Therefore :

$$\int_a^b \frac{\partial A_2}{\partial t}\mathrm{d}x + \Big((A_2 - A_1)U_2 + A_1U_1)_b^{n+1} - ((A_2 - A_1)U_2 + A_1U_1)\Big)_a^{n+1} = 0$$

$$\int_c^d \frac{\partial A_2}{\partial t}\mathrm{d}x + \Big((A_2 - A_1)U_2 + A_1U_1)_d^{n+1} - ((A_2 - A_1)U_2 + A_1U_1)\Big)_c^{n+1} = 0$$

which gives,

$$\begin{aligned}&\frac{\Delta x_a}{2\Delta t_a}\left(A_{2a}^{n+1} - A_{2a}^n + A_{2b}^{n+1} - A_{2b}^n\right) + ((A_2 - A_1)U_2 + A_1U_1)_b^{n+1}\\ &- ((A_2 - A_1)U_2 + A_1U_1))_a^{n+1} = 0\end{aligned}$$

$$\begin{aligned}&\frac{\Delta x_d}{2\Delta t_d}\left(A_{2d}^{n+1} - A_{2d}^n + A_{2c}^{n+1} - A_{2c}^n\right) + ((A_2 - A_1)U_2 + A_1U_1)_d^{n+1}\\ &- ((A_2 - A_1)U_2 + A_1U_1))_c^{n+1} = 0\end{aligned}$$

As for the interior tube,

$$A_{2c}^{n+1} - A_{2c}^n = \frac{El_{2b}}{El_{2c}}\frac{A_{02c}}{A_{02b}}(A_{2b}^{n+1} - A_{2b}^n) \tag{4.58}$$

Put,

$$\Delta A = A_2 - A_1, \qquad R_a = \left(\frac{\Delta x_a}{2\Delta t_a}\right), \qquad R_d = \left(\frac{\Delta x_d}{2\Delta t_d}\right), \qquad K_{2bc} = \frac{El_{2b}}{El_{2c}}\frac{A_{02c}}{A_{02b}}$$

Using the jump condition for the interior tube, $(AU)_{1b} = (AU)_{1c}$, and by proceeding as for the interior tube we obtain :

$$\begin{aligned}A_{2b}^{n+1} =& A_{2b}^n + \frac{(\Delta AU_2 + A_1U_1)_a^{n+1} - (\Delta AU_2 + A_1U_1)_d^{n+1} - R_a(A_{2a}^{n+1} - A_{2a}^n)}{R_a + R_dK_{2bc}}\\ &- \frac{R_d(A_{2d}^{n+1} - A_{2d}^n)}{R_a + R_dK_{2bc}}\end{aligned} \tag{4.59}$$

$$\begin{aligned}U_{2b}^{n+1} =& \frac{(\Delta AU_2 + A_1U_1)_a^{n+1} + (\Delta AU_2 + A_1U_1)_d^{n+1} - R_a(A_{2a}^{n+1} - A_{2a}^n)}{2(\Delta A)_b^{n+1}}\\ &+ \frac{R_d(A_{2d}^{n+1} - A_{2d}^n) - 2(AU)_{1b}^{n+1} - (R_a - R_dK_{2bc})(A_{2b}^{n+1} - A_{2b}^n)}{2(\Delta A)_b^{n+1}}\end{aligned} \tag{4.60}$$

We notice that the parameters U, P and A of the two tubes are coupled. Therefore, first we could calculate A_{2b} using the equation (4.59).
From the equation (4.56), we obtain P_{2b}.
From the equation (4.55), we obtain P_{2c}.
From the equation (4.57), we obtain A_{2c}.
From the equation (4.52), we obtain A_{1b}.
From the equation (4.53), we obtain U_{1b}.
From the equation (4.44), we obtain P_{1b}.
From the equation (4.43), we obtain P_{1c}.
From the equation (4.45), we obtain A_{1c}.
From the equation (4.42), we obtain U_{1c}.
From the equation (4.60), we obtain U_{2b}.
From the equation (4.54), we obtain U_{2c}.

Chapter 5

Blood-CSF coupling effect on the cerebral vasculature and CSF dynamics

Sommaire

5.1 Introduction

This chapter first aims to investigate and analyze the main effects of coupling blood and CSF flow on pulse wave propagation. Several aspects are highlighted. During the first section, we analyse the effect of CSF pulsations on blood dynamics. Thus, two models are being compared, a model accounting for CSF coupling and a model lacking CSF coupling. In the second section, we investigate the effect of varying the CSF confinement or CSF volume. Finally, the third section elucidates the role played by the cranial and spinal CSF compartments compliance during vascular brain expansion.

General considerations The following outcomes will be considered:

- The mean pressure, $\bar{P}$, and mean flow, $\bar{Q}$.
- The pressure peak to peak or pulse pressure, P_{pp}, defined as the difference between the maximum and minimum pressure amplitudes. Usually for clinicians, the term *Pulse Pressure* accounts for the difference between the systolic and diastolic blood pressure.

- The peak flow, Q_p as 'p' for peak.
- The stroke volume, S_v, defined as the amount of blood or CSF displaced at each cardiac cycle.
- The pulse wave velocity (PWV) defined as the velocity at which a pulse wave propagates from site to site.
- The phase-lag. As we made the assumption that the driving force behind CSF pulsations is the arterial input, we used the carotid artery flow as the reference against which we compared blood and CSF flow. It is computed as the difference between two analogous points of two signals, divided by the total period of the wave. It is expressed in percentage of the cardiac cycle $\%cc$. The phase lag between the internal carotid and jugular peak flows or cervical CSF flows reflects the pulse wave velocity through the vessels between these 2 sites and can be used as a measure of vascular or CSF system compliance.

Remarque 5.1
*Recall that the following subscripts are used : 'c-m' refers to the curent model, the **c**oupled blood-CSF **m**odel, in contrast to 'u-m' for the **u**ncoupled blood model, i.e a model lacking CSF coupling. 'cv' refers to the **c**erebral **v**asculature. As for the CSF system, csas refers to the **c**ranial **s**ub**a**rachnoid **s**paces and ssas for spinal subarachnoid spaces.*

5.2 An arterial sinusoidal waveform

Boundary conditions First a sinusoidal input pressure with an apporpriate waveform is used to model in the simplest way the arterial pressure and reproduce the physiological conditions. The results of a physiological arterial waveform will be displayed in section 5.7. It features a systolic blood pressure of 120 mmHg, a diastolic blood pressure of 80 mmHg, and a period of T=0.85 s. However, temporal evolution results will be displayed in a dimensionless time (t/T). The arterial pressure was imposed at the inlet of the cerebral vasculature, i.e the paired carotids and vertebral arteries whereas a constant output pressure of 5.832 mmHg was assumed at the outlet of the jugular veins 33 & 34.

Computations were performed using the following values of the CSF network mechanical properties:a cranial CSF confinement at zero transmural pressure of $\lambda_{0cb} = 0.7$ It corresponds to a total CSF volume of 130 mL which lies in the range of MRI measured CSF volumes. The cranial and spinal dura mater were assigned an elastic modulus of $E_l = 10^7$ mmHg which yielded to a cranial sas compliance of 0.02 mL/mmHg and a spinal sas compliance of 0.01 mL/mmHg.

Arterial, venous and Spinal CSF flow Figure (5.1) displays pressure and flow of the carotid artery, the jugular vein and the cervical CSF flow. Table (5.1) details the maximum, mean and minimum amplitudes of pressure and flow. The model predicted a global cerebral

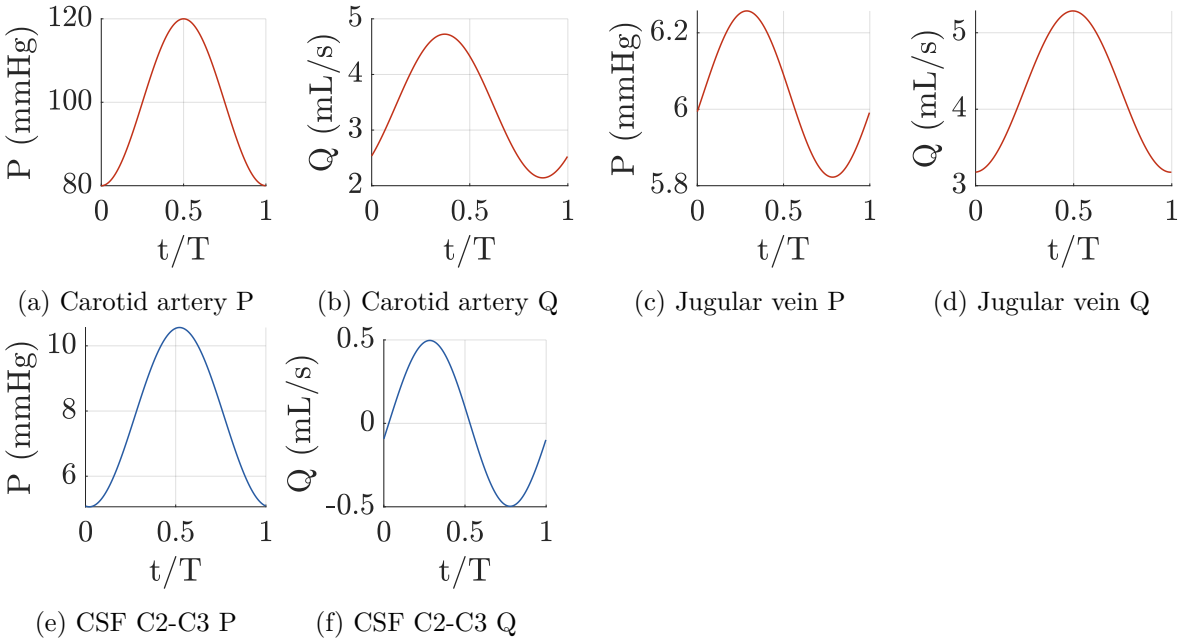

(a) Carotid artery P (b) Carotid artery Q (c) Jugular vein P (d) Jugular vein Q

(e) CSF C2-C3 P (f) CSF C2-C3 Q

Figure 5.1: Pressure and flow of the carotid artery, the jugular vein and the cervical CSF flow for a sinuoidal waveform

blood flow of 10.1 cm^3/s which corresponds for an average brain of 1400 g to a cerebral blood volume (CBV) of 43.2 mL.100 g^{-1}.min^{-1} which is within the normal range of CBF [61].

The model predicts a pulsatile spinal CSF flow with zero net flow, a CSF caudal flow during systole and a CSF rostral flow during diastole, a peak flow of 0.5 mL/s and a stroke volume of 0.2 mL which is in accordance with previous MRI observations [2, 24, 16, 5].

	Inlet carotid arteries 1 & 2	Inlet vertebral arteries 3 & 4	Outlet jugular veins 33 & 34	Cervical CSF
P_{max}, P_{mean}, P_{min} (mmHg)	120/100/80	120/100/80	6.2/5.8/6	10.5/7.8/5
Q_{max}, Q_{mean}, Q_{min} (mL/s)	4.7/3.4/2.1	2.3/1.6/0.8	5.3/4.2/3.1	0.5/10^{-6}/-0.5

Table 5.1: Maximum, mean and minimum pressure-flow amplitudes of carotid artery 1, jugular vein 33 and cervical CSF for a sinusoidal arterial waveform

Reynolds number and Womersley number Reynolds and Womersley numbers are the two nondimensional parameters used to specify pulsatile flow. The Reynolds number relates the ratio of inertial to viscous forces. Hereby, we considered the peak or systolic Reynolds R_p number (subscript p as peak). It was defined by,

$$R_p = \rho D \frac{u_p}{\mu} \tag{5.1}$$

It is based on the fluid peak velocity u_p, the fluid density ρ and kinematic voscosity μ. The characteritic dimension D was either the diameter for a circular tube or the hydraulic diameter for an annular tube. The hydraulic diameter being computed as $4.Area/perimeter$. For the cerebral vasculature, when vessels were regrouped into equivalent tubes such as the pial arteries or the microcirculation, the peak Reynolds number was computed based upon the real section and not the equivalent section.

Figure 5.2a displays the peak Reynolds number for the cv (in red) and the cranial sas (in blue). The maximum peak Reynolds number, $Re_p = 400$, for the cerebral vasculature was observed at the large carotid arteries (vessel number 1 and 2). The regrouped vessels such as the pial network (vessel 21), the intracerebral arteries (vessel 22) and the microcirculation (number 23) displayed, although not visible, low Reynolds numbers.

Our model predicts cranial CSF flow Reynolds number of less than 50. Gupta et al. [29] have performed 3D CFD simulations and reported Reynolds number of 114 and 20 in the anterior and cranial SAS. Howden et al. observed using CFD simulations a maximum Reynolds number of 15 in the ventricular system. Pahlavian et al. [53] and Loth at al. [42] performed respectively 3D and 2D CFD simulations in the cervical spine and reported respectively peak Reynolds number of 187 and 201. The current model predicts at the C2-C3 region a Reynolds number of 146 which is in agreement with the latter studies.

The Womersley number quantifies the transient inertial forces in proportion to viscous effects. It was defined as,

$$W_o = \frac{D}{2}\sqrt{\rho\frac{\omega}{\mu}} \tag{5.2}$$

where $w = 2\pi/T$ is the cardiac pulsation and D is either the diameter for a circular tube or the hydraulic diameter for an annular tube. Figure 5.2b displays the Womersley number of the cv (in red) and the cranial sas (in blue). Recall that for a circular tube, the Poiseuille velocity hypothesized in our mathematical formulation is theoretically only valid for a steady flow. However, it can be used as a first approximation for small values of Womersley numbers. For the cv and the cranial sas, the largest value of W_o is about 11 for the transverse sinus (number 32) and 4 for the annular cranial sas enclosing the transverse sinus. Their effects may be considered negligible relative to the whole network. Loth at al. [42] have quantified CSF flow Womersley numbers and has found it varying between 5 and 17. In this study, [42] has found the greatest Womersley number in the cervical and lumbar sas.

Recall that in our study, for a simplification matter, we have assumed a quasi-steady fow approximation. This approximation has led to assume a parabolic velocity profile in order to approximate the wall shear stress. The validity of this approximation in the annular and circular spinal subarachnoid space (SSS) is discussed in the undergoing publication of annexe C. In summary, the wall shear stress was found depending on two parameters, the Womersley number and the width of the annular SSS. We found that the more the annular SSS is narrow, the more the average wall shear stress of a quasi-steady fow approximation is valid.

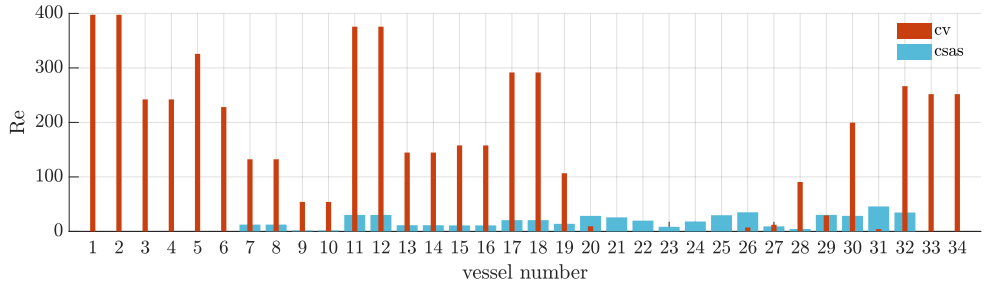

(a) Reynolds number

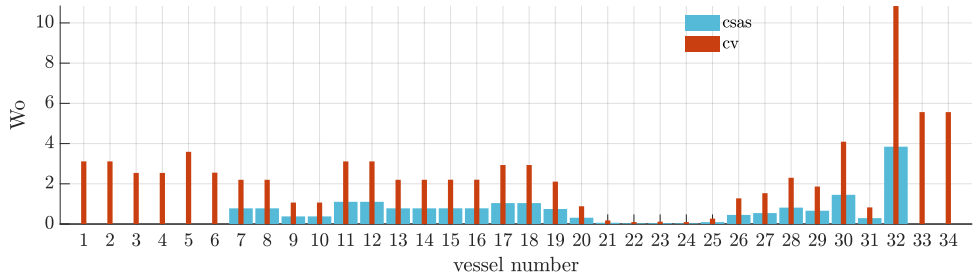

(b) Womersley number

Figure 5.2: Dimensionless Reynolds and Womersley number of the cerebral vasculature (cv) and the cranial subarachnoid spaces (csas)

Damping mechanisms due to CSF coupling For every organ in the human body, the arterial Windkessel properties of the vasculature are known to play a significant role in buffering arterial pulsations through elasticity of the blood vessels [71, 13]. In the brain, the arterial Winkessel mechanism is thought to buffer acute arterial pulsations, which may be harmful to the cerebral bed capillary network, to a more steady stream of blood. A physiologically important aspect of pulsatility in the cranium is the Windkessel effect, the dissipation of arterial pulsatility rendering capillary blood flow nearly pulseless. Moreover, Wagshul et al. [43] has suggest that due to abnormal compliance of patients with chronic hydrocephalus, CSF may also play a role as the *brain's shock absorber* by allowing dissipations of intracranial pulsations before they are able to reach the microcirculation. Later, the authors have performed changes in ICP in dogs and have hypothesized that the intracranial compartements appear to act as a notch filter (Band reject filter) attenuating the frequency of the heart rate relative to other frequencies [22, 74].

Pressure and flow of the cv can be divided following two groups: on the one hand the arterial network and on the other hand the more compliant venous network. Hereby, arterial vessel number 21 equivalent to the arterioles and venous vessel number 31 equivalent to the transverse sinuses were chosen respectively as representative of both the arterial and the venous network. A similar strategie was performed for the subarachnoid spaces. On the one hand, the cranial sas coaxial to the arterial system and on the other hand, the cranial sas coaxial to the venous system.

Figure (5.3) portrays from left to right the temporal distribution during a dimensionless

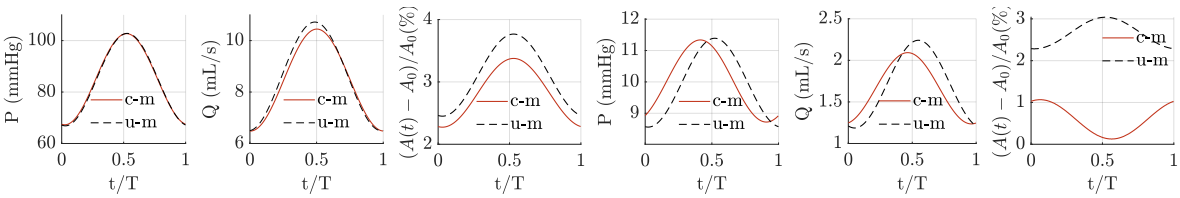

(a) Pressure (b) Flow (c) Area (d) Pressure (e) Flow (f) Area

Figure 5.3: From left to right : Pressure, flow and relative area temporal evolution of arterioles (vessel 21) followed by the transverse sinus (vessel 31). c-m: coupled model, u-m: uncoupled model

period (t/T) of pressure P, flow Q and relative section ($(A(t) - A_0)/A_0)$) of arterioles vessel 21 followed by the transverse sinuses 31. Solid lines denotes the current blood-CSF coupled model (c-m) and dashed lines refers to the uncoupled blood model ('u-m').

During a cardiac cycle blood pressure rises in systole and decreases in diastole (see subfigure (a) and (d)). Due to the pressure gradient or CPP, blood flow is positive and closely follows the pressure waveform (see subfigure (b) and (e)). Finally, the model predicts blood small area variation (see subfigure (c and (f)).

In the c-m model, CSF pulsations were found to cause a dampening and a phase lag of pressure and section relative to the uncoupled model u-m. The dampening was found to impact the maximum and the minimum amplitude. However, mean flow and pressure were not affected which implies that the maximum amplitude dampening is equal to the minimum amplitude dampening. Moreover, in the c-m model note that CSF flow causes compression of the venous vessels (see (f)).

Figure (5.4) displays the attenuation values of peak flow, $\%Q_p$, and peak to peak pressure, $\%P_{pp}$ accross the cv. Recall that the arterial network designates vessel 1 to 22 and the venous vessels designates vessels 24 to 34. Vessel 23 being the microcirculation. For example, the arterial system pulse pressure (vessel 1 or 2) was found decreased by less than $\sim 2\%$ whereas the venous system pulse pressure was found decreased by more than $\sim 6\%$. CSF flow causes more reduction to the compliant venous network than the arterial network.

Time delay of the cv relative to the carotid artery flow is displayed in figure (5.5) for the c-m and the u-m models. CSF pulsations slightly affect the phase lag in arteries whereas there is a significant reduced phase lag in the venous system. Note that the jugular vein peak flow was found to occur earlier due to confinement and mainly to the great cranial elastance. Hence, CSF coupling allows a faster transmission of the arterial pulsations to the venous vessels via the cranial subarachnoid space.

Cranial CSF flow Figure (5.6) portrays the temporal distribution during a dimensionless period (t/T) of flow, pressure and relative section of cranial subarachnoid spaces coaxial to the arterioles (number 21) and the transverse sinuses (number 31). Recall that blood and CSF pressure are coupled using the tube law equation established in section 4.2.3

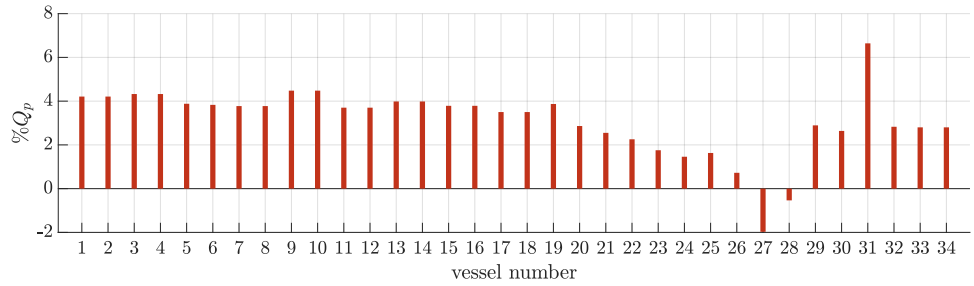

(a) Blood flow amplitude variation

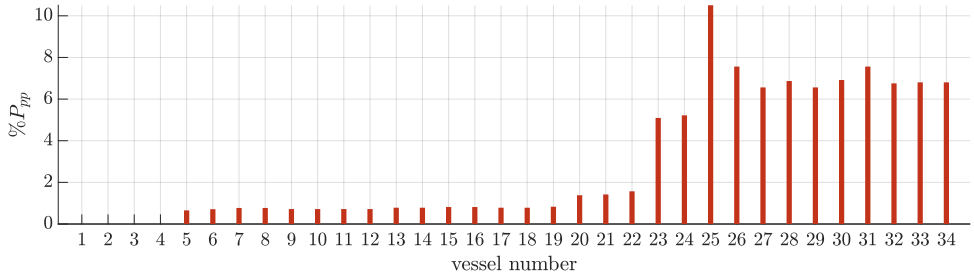

(b) Blood peak to peak pressure variation

Figure 5.4: Blood peak flow and blood peak to peak pressure damping accross the coaxial cerebral vasculature

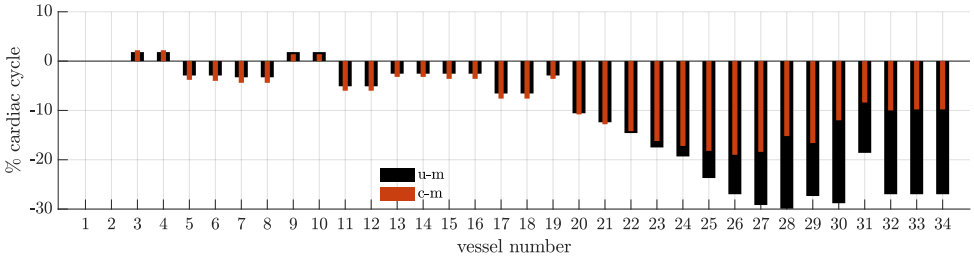

Figure 5.5: Phase lag to carotid artery flow. c-m: coupled-model, u-m: uncoupled-model

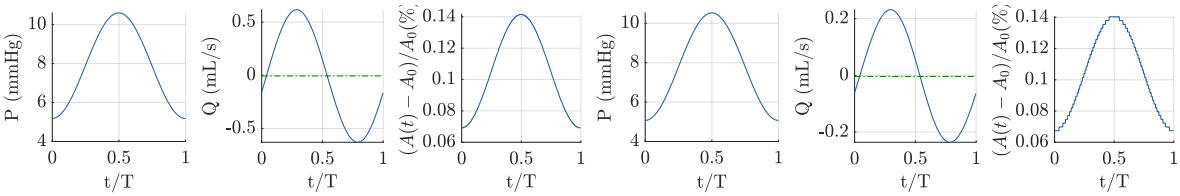

(a) Pressure (b) Flow (c) Area (d) Pressure (e) Flow (f) Area

Figure 5.6: From left to right, pressure, flow and relative area temporal evolution of cranial sas coaxial to arterioles (vessel 21) and coaxial to transverse sinus (vessel 31)

$P_c = P_b - (E_l)_b(A_b/(A_0)_b - 1)$ where P_c is the CSF pressure, P_b is the blood pressure, $(E_l)_b$ is the blood vessel elastance, A_b is the varying cross sectional area and $(A_0)_b$ is the cross-sectional area at zero transmurale pressure. Hence, cranial CSF pressure closely follows blood pressure waveform (see subfigure (a) and (d). Subfigures (b) and (e) displays cranial CSF flow. The model predicts a mean cranial CSF flow, in green dashed lines, close to zero implying that cranial CSF flow is pulsatile flowing forwards and backwards during a cardiac cycle. Finally, the model predicts small cranial sas area variation, subfigure (c) and (f).

Pressure drop accross the cerebral vasculature and intracranial pressure Recall that the cerebral vaculature is composed of 34 vessels where each blood vessel starting from the basilar artery bifurcation (vessel 7 & 8) to the transverse sinuses (vessel 32) is surrounded by the cranial subarachnoid spaces. Figure (5.7a) portrays the predicted mean pressure of the cerebral vasculature (cv). Figure shows that blood pressure drops unevenly as blood travels from arteries to arterioles, capillaries, venules, and veins, and encounters greater resistance. However, the site of the most precipitous drop, and the site of greatest resistance occurs at the arterioles (vessel 22). Arterioles admits a greatest elastance than previous vessels, a larger cross sectional area but individually a smaller diameter. This means more of the blood is in contact with the vessel wall, and therefore resistance increases. This explains why vasodilation and vasoconstriction of arterioles play more significant roles in regulating blood pressure than do the vasodilation and vasoconstriction of other vessels.

Figure (5.7b) portrays the predicted maximum, mean and minimum pressure of the csas (cv). CSF mean pressure remains roughly constant at about 8 mmHg. Cranial CSF peak to peak pressure are small despite large arterial peak to peak pressure of 40 mmHg. The CSF pressure steadiness is due to the availability of the compliant spinal canal to receive CSF. The model supports the theory of the spinal canal's role to attenuate CSF pressure amplitudes.

Blood and CSF fluids variations Figure (5.8) portrays volume temporal distribution of the total coaxial blood vessels, the arterial system, the venous system, the cranial and the spinal CSF. First of all, the brain vasculature volume, subfigure (a), was found to expands lesser due to CSF presence. Indeed, as the arterial volume variation, subfigure (b), is slightly affected by CSF pulsations, it is mainly the venous volume, subfigure (c) which is greatly attenuated. Moreover, during systole, i.e the first half-period, due to CSF presence the model

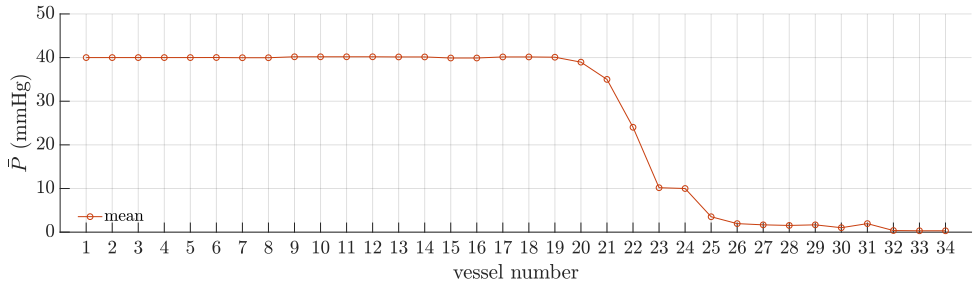

(a) Mean pressure of the cerebral vasculature (cv)

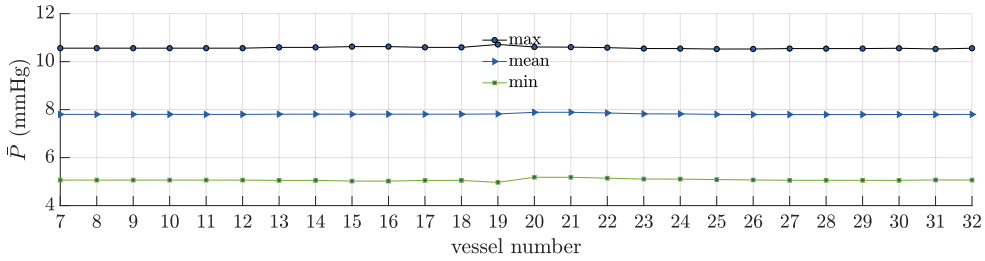

(b) Max., mean and min. of cranial CSF pressure

Figure 5.7: (a) Mean pressure of the cerebral vasculature (cv). (b) Max., mean and min. of cranial CSF pressure

predicts a compression of the venous system instead of dilatation in a model lacking CSF coupling.

Coaxial blood vessels were found to inflate and deflate by 0.26 mL, the same amount of spinal CSF stroke volume of 0.26 mL reported previously.

To explain fluids exchange between blood and CSF between the cranial and spinal vaults, their volumes were scaled and plotted in subfigure 5.8f. During the first half-period, arterial volume expansion is regulated by both venous volume and cranial CSF volume compression. The decrease in intracranial CSF volume is made possible by means of displacement of cranial CSF into the spinal sas which can expand by the compliance of the dural sac.

Our model supports the theory that during systole, the arterial volume expansion is regulated by two complementary damping mechanisms which are the venous compression and the spinal CSF volume increase.

5.3 Effect of varying the confinement and assessment of CSF viscosity

This section explores cranial CSF confinement effect on blood and CSF flow dynamics. A mentionned previously, the cranial CSF confinement is a dimensionless number which relates a blood vessel section to a cranial sas section at zero transmural pressure. $\boldsymbol{\lambda_{cb}}$, may range

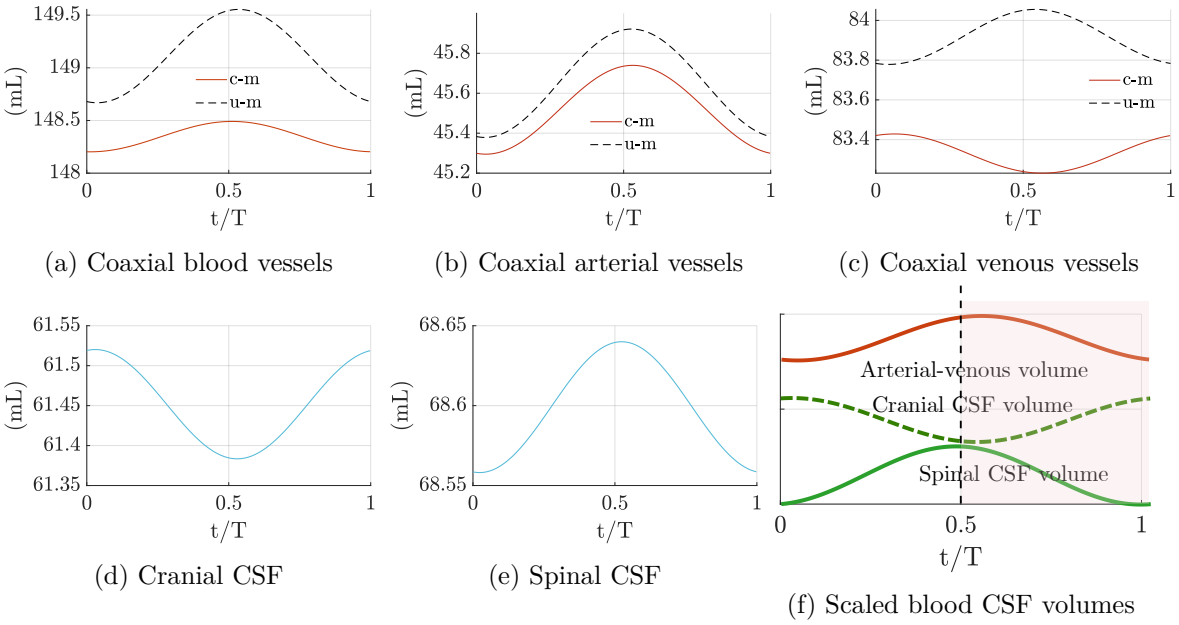

(a) Coaxial blood vessels (b) Coaxial arterial vessels (c) Coaxial venous vessels

(d) Cranial CSF (e) Spinal CSF (f) Scaled blood CSF volumes

Figure 5.8: Blood and CSF fluids exchanges between the arterial, venous vasculature and the cranial and spinal CSF.

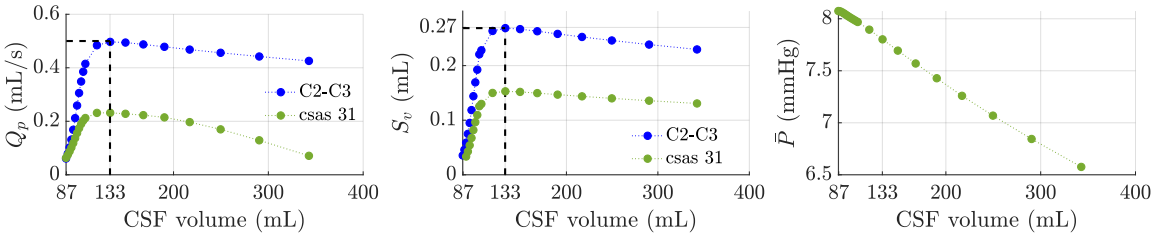

(a) Peak flow (b) Stroke volume (c) Mean pressure

Figure 5.9: Effect of CSF confinement or CSF volume on CSF peak flow, stroke volume and mean pressure

from **0.1** (a total CSF volume of 1400 mL, a cranial CSF volume of 1332 mL and a spinal CSF one of 68 mL) to **0.85** (a total CSF volume of 95 mL, a cranial CSF one of 28 mL and a spinal CSF one of 68 mL).

Figure (5.9) depicts CSF flow amplitude, stroke volume, mean pressure and pulse pressure as a function of confinement for spinal C2-C3 CSF flow and cranial sas coaxial to transverse sinuses 31.

CSF peak flow and stroke volume Cervical CSF and cranial sas peak flow and stroke volume reaches respectively an optimum for a CSF volume of 133 mL corresponding to a CSF confinement of $lambda_{cb}$=0.7. CSF confinement quantifies the importance of cerebral blood

section (volume) to cranial CSF section (volume),

$$\frac{volume(blood)}{volume(csf)} = \frac{\lambda_{cb}}{1-\lambda_{cb}} \tag{5.3}$$

In cranial sas 31, as λ_{cb} reaches towards 0.1 or as cranial CSF volume increases, cerebral blood volume is assumed to drag a great amount of cranial CSF volume, and consequently CSF flow drops. Whereas, as λ_{cb} reaches towards 0.9, or as cranial CSF volume decreases, there is more CSF contacting the vessel wall, thus higher friction and higher resistance and subsequently decreasing flow. This demonstrates the existence of a confinement at which CSF flow and stroke volume are maximal. A more theoretical investigation requires a closer look to the momentum conservation equation for an annular tube. Recall that the momentum equation of an annular tube was defined as,

$$\rho\frac{\partial Q_2}{\partial t} + \rho\frac{\partial}{\partial z}\left(\frac{Q_2^2}{A_2 - A_1}\right) + (A_2 - A_1)\frac{\partial P_2}{\partial z} = 2\pi(R_2\tau_2 - R_2\tau_{12}) \tag{5.4}$$

where the first term of the left hand side $\partial Q_2/\partial t$ represents the inertial forces, the second term portrays the convective term $\partial(Q_2^2/(A_2 - A_1))/\partial z$, the third term $(A_2 - A_1)\partial P_2/\partial z$ represents the pressure term and finally the right hand side displays the viscous term $2\pi(R_2\tau_2 - R_2\tau_{12})$. Figure (5.10) depicts temporal evolution of these four terms in cranial sas coaxial to transverse sinus 31 for three confinement values λ_{cb} =0.3, 0.5 and 0.7.

As displayed in figure (5.10) for a confinement of λ_{cb} =0.3, inertial forces (in blue line) dominate the viscous forces (in green line). For a confinement of λ_{cb} =0.5, inertial and viscous forces are of the same order of magnitude and finally for a confinement of λ_{cb} =0.7, viscous forces greatly dominates inertial forces. To finally assess the imbalance between inertial and viscous forces, figure (5.11) compares CSF maximum flow evolution for a viscous and non viscous CSF model. As expected, when considering CSF viscous, CSF maximum flow drops at lower confinement due to higher friction.

Loth et al. [42] numerical and experimental study showed that the pulsatile flow of the CSF in the spinal sas is characterised by relatively dominated inertia effects mainly near the cervical and lumbar area, i.e where spinal sas are the largest. However, as sas gets smaller, viscous effect increases and challenges inertia effect suggesting the need to account for CSF viscosity at least in small annular spaces as the cranial sas. Finally, it is important to note that the overall contribution of CSF viscosity is not negligible in the cranial sas and therefore may affect spinal CSF.

5.4 Effect of the cranio-spinal compliance

Recall that cerebral compliance is provided mainly by the intracranial venous system, the extracellular spaces and the CSF system. Intracranial compliance (ICC) represents the change in volume (ΔV) per unit change in pressure (ΔP), and is exactly the inverse of elastance. In

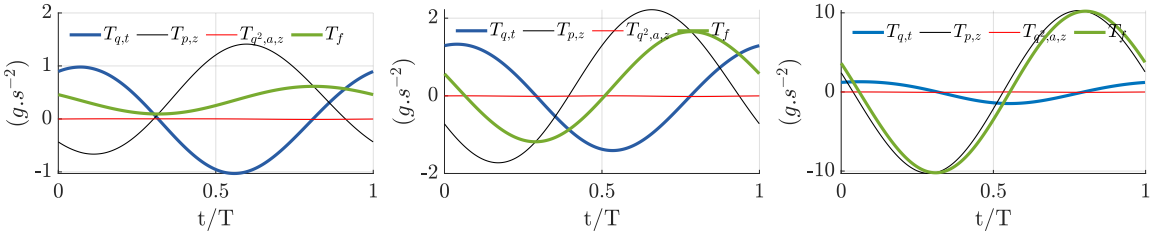

(a) λ_{cb}=0.3 (b) λ_{cb}=0.5 (c) λ_{cb}=0.7

Figure 5.10: Evolution during a cycle of the conservation of momentum terms for three different confinement λ_{cb}=0.3, 0.5 and 0.7 where $\boldsymbol{T_{q,t}} = \rho dQ_2/dt$, $\boldsymbol{T_{p,z}} = (A_2 - A_1)dp/dz$, $\boldsymbol{T_{q^2,a,z}} = d(A_{anr} * Q^2)/dz$ and $\boldsymbol{T_f} = 2\pi(R_2\tau_2 - R_1\tau_{12})$.

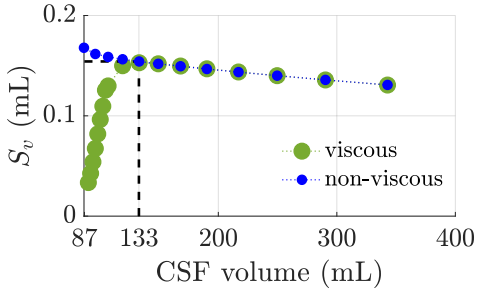

Figure 5.11: Effect of CSF viscosity on cranial CSF peak flow

other words, ICC determines the ability of the intracranial compartment to accommodate an increase in volume without a large increase in pressure. In this section, we investigate the effect of the craniospinal compliance of subarachnoid spaces on blood and CSF pulsations. Recall that the elastic Young modulus differs from the elastance which is the reciprocal of the compliance.

In order to allow analogy between the cranial and the spinal compliance, their respective elastic Young modulus will be expressed in terms of a volumetric compliance using the tube law equation. Morevoer, the three elements Windkessel compliance will be tuned in order to equal the compliance of the spinal dura mater.

Intrinsic relationship between a vessel compliance and the elastic modulus of its wall Recall that a vessel compliance expressed in $(mL/(dyne/cm^2)$ is defined as,

$$C = \Delta V/\Delta P \tag{5.5}$$

Moreover, in our mathematical formulation of the tube law equation, a linear relation was assumed beetween the transmural pressure P_t and the varying vessel cross-sectional area A (or vessel volume V) defined as,

$$P_t = E_l(\frac{A}{A_0} - 1) = E_l(\frac{V}{V_0} - 1) \tag{5.6}$$

where A_0 and V_0 are respectively the cross sectional area volume at zero transmural pressure and E_l is the Young modulus expressed in $dyne/cm^2$.

By combining the two previous equation (5.5) and (5.6), one might write,

$$\Delta P_t = E_l \frac{\Delta V}{V_0}, \quad \frac{\Delta V}{\Delta P_t} = \frac{V_0}{E_l}, \quad C_l = \frac{V_0}{E_l} \tag{5.7}$$

Using the latter equation, the cranial sas compliance will be defined as $C_l c = V_0 c / E_l c$ where $E_l c$ is the cranial dura mater elastic modulus and $V_0 c$ is the cranial CSF volume. In a similar manner, the spinal sas compliance will be defined as $C_l s = V_0 s / E_l s$ where $E_l s$ is the spinal dura mater elastic modulus and $V_0 s$ is the spinal CSF volume. Finally, as mentioned previously, the 3 element Windkessel compliance was assumed to be identical to spinal sas compliance.

5.5 Effect of varying the cranial subarachnoid spaces compliance

In this section, we investigate the cranial subarachnoid spaces compliance effect on blood and CSF dynamics. CSF volume was assumed to be 215 mL divided into a cranial CSF volume of 147 mL and a spinal CSF one of 68 mL which lie within the range of physiological CSF volume values [3, 63]. Usually, healthy physiological values of the Young elastic modulus of the dura mater ranges between 600 mmHg and 5.10^4 mmHg as described previously in section 3.4.1. In this study, for a theoretical perspective and to account for extreme cases of either very compliant or very rigid dura mater, the range of the dura mater elastic Young modulus was extended. Therefore, the cranial sas elastic modulus $E_l c$ was taken varying between 75 mmHg and $7.5.10^4$ mmHg which correponds to a cranial sas compliance varying between 0.002 and 2 mL/mmHg. The spinal sas elastic modulus was assumed equal to 10^3 mmHg whic implies a spinal compliance of 0.07 mL/mmHg. Finally, the 3 elements Winkessel compliance was assumed equal to 0.07 mL/mmHg.

Figure (5.12) displays cranial and spinal mean pressure, peak flow and stroke volume as a function of the cranial sas compliance. Regarding venous flow, displayed (a) and (b), as cranial sas compliance decreases, CSF pulsations were found to dampen venous peak flow and pulse pressure. Whereas, as cranial sas increases, the effect of the constraint on the venous flow weakens, and consequently peak flow and pulse pressure increase and tend to converge towards a model lacking CSF coupling.

The model predicts that decreasing intracranial compliance increases CSF mean pressure, pulse pressure and peak flow in the cranial and spinal vault. As demonstrated by several MRI studies of pathological disorders, decreased intracranial compliance severly affects intracranial pressure. For example, a previous study by Alperin et al. [4] has provided evidence that increasing ICC compliance by means of decompression surgery in Chiari Malformations has

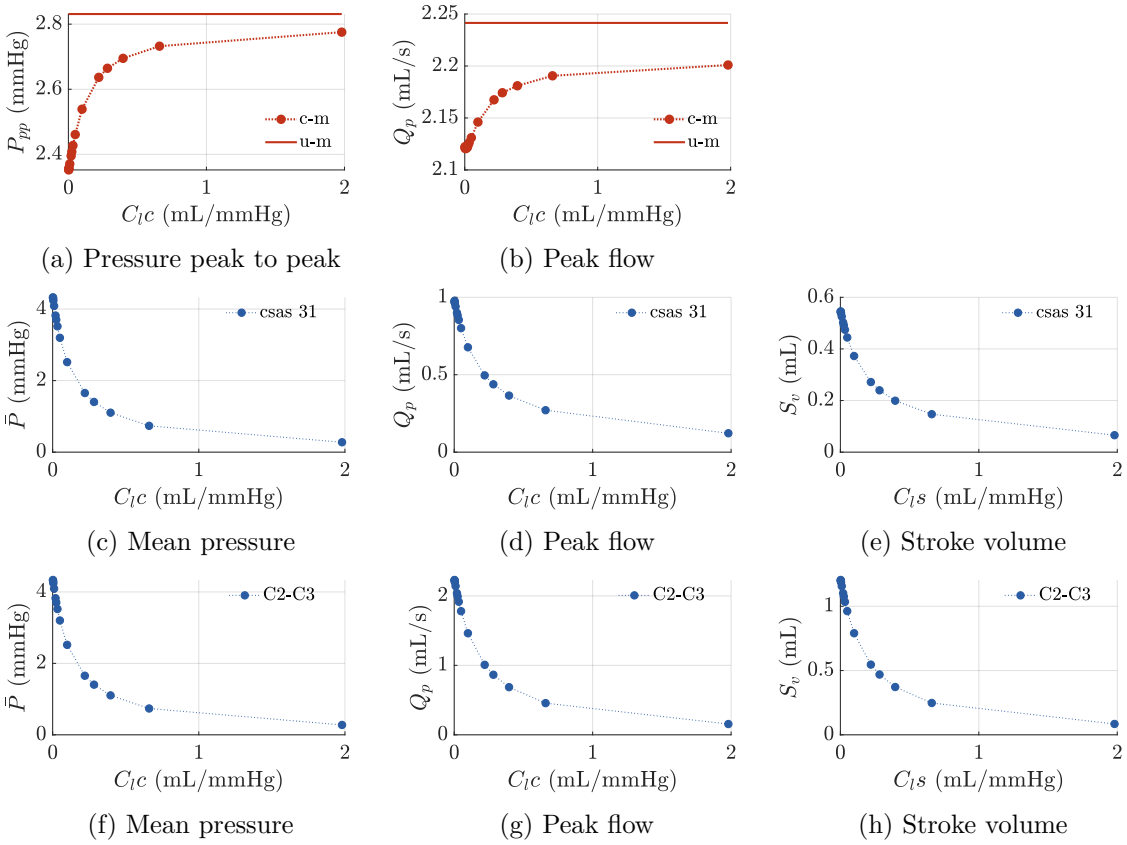

(a) Pressure peak to peak (b) Peak flow

(c) Mean pressure (d) Peak flow (e) Stroke volume

(f) Mean pressure (g) Peak flow (h) Stroke volume

Figure 5.12: Effect of intracranial compliance $C_l d$ on (working from top to bottom) venous flow, cranial CSF flow and spinal CSF flow

shown a great decrease in CSF pressure.

5.6 Effect of varying the spinal subarachnoid spaces compliance

In this section, we investigate the spinal subarachnoid spaces compliance effect on blood and CSF dynamics. CSF volume was assumed to be 215 mL divided into a cranial CSF volume of 147 mL and a spinal CSF one of 68 mL. The spinal sas elastic modulus $E_l c$ was taken varying between 37.5 mmHg and $7.5.10^4$ mmHg which correponds to a spinal sas compliance varying between 0.001 and 2 mL/mmHg. The cranial sas elastic modulus was assumed equal to $7.5.10^4$ mmHg which implies a cranial compliance of 0.002 mL/mmHg. Finally, the 3 elements Winkessel compliance was assumed varying and equal to the spinal sas compliance.

Figure (5.13) displays cranial and spinal CSF mean pressure, peak flow and stroke volume as a function of the spinal sas compliance. The curves distribution may be divided into two parts: a high compliance part and a low compliance part. In the low compliance part, despite

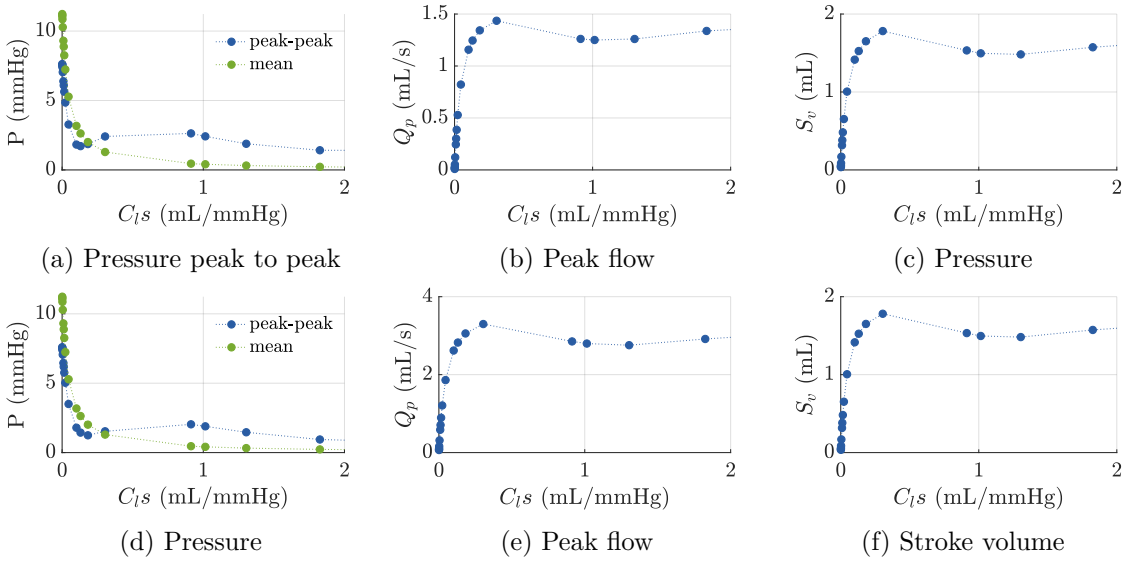

(a) Pressure peak to peak (b) Peak flow (c) Pressure

(d) Pressure (e) Peak flow (f) Stroke volume

Figure 5.13: Effect of spinal dura mater elasic modulus E_ld on cranial, spinal CSF and venous flow.

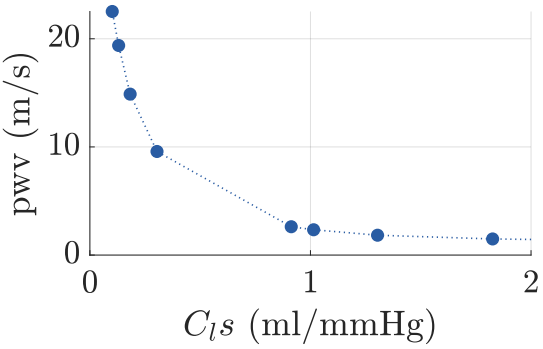

Figure 5.14: Spinal volumetric compliance effect on spinal CSF pulse wave velocity (pwv)

the increase in spinal compliance, cranial and cervical CSF display a plateau of pressure and a maximum followed by a plateau for peak flow and stroke volume. However, in the low compliance part, any small decrease in the spinal compliance elicit high increases in cranial and spinal pressure and consequently a decrease in cranial and spinal flow. This behaviour reminds the presure-volume curve linking intracranial pressure to intracranial compliance. In the high compliance part, spinal and cranial CSF pressure are steady, whereas as spinal compliance decrease, CSF fails to play its buffering role, thus resulting in an increase of pressure and ultimately a decrease of flow.

Figure (5.14) displays spinal CSF pulse wave velocity along the spinal sas between the cervical and the lumbar region. Spinal sas pwv was found to decrease under increasing spinal sas compliance. Moreover, the range of pulse wave velocity is in agreement with previous MRI studies as Kalata et al. [36] where, in this study, a novel MR sequence was used to acquire unsteady spinal CSF velocity measurements during the cardiac cycle.

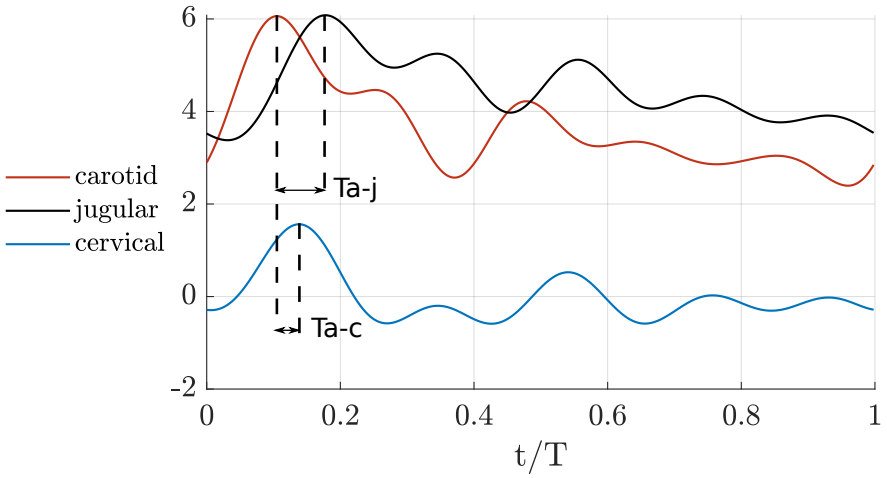

Figure 5.15: Carotid, jugular and CSF flow for a physiological input waveform

5.7 An arterial physiological waveform

In this section, we briefly presents the same results described before, although here we use a physiological input waveform.

Figure (5.15) displays the carotid, jugular and cervical CSF flow. The model predicted a global cerebral blood flow of 10.1 cm^3/s which corresponds for an average brain of 1400 g to a cerebral blood volume (CBV) of 43.2 mL.100 g^{-1}.min^{-1}.

The model predicts a pulsatile spinal CSF flow with zero net flow, a peak flow of 2.7 mL/s and a stroke volume of 0.6 mL. $Ta - v = 9.8$ and $Ta - c = 7.8$ are the times delay occuring between the venous and cervical CSF flow peaks compared to the arterial systolic flow peak. These times are expressed as a percentage of the cardiac cycle. CSF cervical peak flow was found to occur earlier than jugular peak flow.

Cerebral blood flow for a physiological and a sinusoidal waveform was found the same however CSF stroke volume computed from a physiological waveform was found greater and closer to physiological values [2].

	Inlet carotid arteries 1 & 2	Inlet vertebral arteries 3 & 4	Outlet jugular veins 33 & 34	Cervical CSF
P_{max}, P_{mean}, P_{min} (mmHg)	122/105/86	120/105/86	5.8/5.8/5.8	7.8/5/2.4
Q_{max}, Q_{mean}, Q_{min} (mL/s)	6/3.6/2.4	3.2/1.7/1	6/4.5/3.4	$1.5/10^{-6}$/-0.6

Table 5.2: Maximum, mean and minimum pressure-flow amplitudes of carotid artery 1, jugular vein 33 and cervical CSF for a physiological arterial waveform

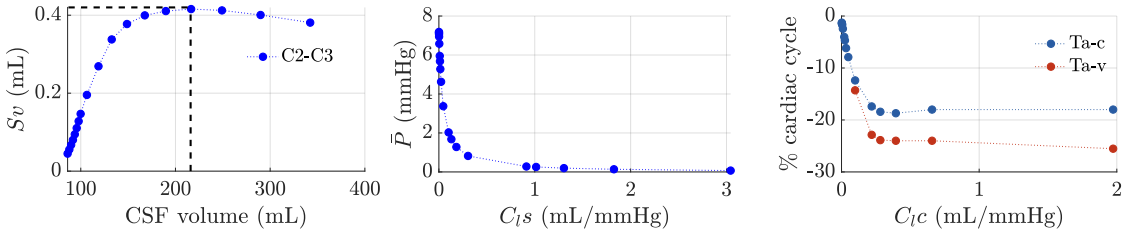

(a) Cervical peak flow (b) Mean cranial CSF pressure (c) Phase lag Ta-c and Ta-v

Figure 5.16: A physiological waveform: effect of CSF volume and cranio-spinal compliance on CSF flow. Ta-c: arterial to CSF cervical flow time delay, Ta-v: arterial to venous flow time delay

Effect of CSF volume and cranio-spinal compliance Simulations performed using a physiological arterial input showed overall similar distribution as using a sinusoidal waveform. We recall here the major results described before. Figure 5.16c displays for a physiological waveform the effect of CSF volume and cranio-spinal compliance. As mentioned previously, an optimum stroke volume was found. However, it was found at a CSF volume of 216 mL instead of 130 mL using a sinusoidal input. Once again, cranial CSF pressure was found to increase by decreasing overall cranio-spinal compliance. Finally, figure (5.16) portrays the carotid flow to venous flow and cervical flow delay as a function of intracranial compliance. Cervical flow and venous flow occured earlier under decreasing intracranial compliance. Note that cervical flow occurs earlier than venous flow.

5.8 Conclusion

The analysis of the 1-D has enable to identify the major CSF pulsations effect on the overall blood and CSF dynamics in the cranial and spinl vault. These preliminary results were able to capture the major features of blood and CSF dynamics which are in agreement with numerous MRI studies [2, 24, 16, 5].. In the first section, the model predicts that CSF pulsations appear to play a major role in damping cerebral pulsations mainly in the venous than the arterial one due to the compliant nature of the venous system. Although arterial pulsations were less attenuated than venous pulsations, it appears that our model supports the theory of Wagshul et al. [43] that CSF may also play a role as the *brain's shock absorber* and help the brain vasculature Windkessel mechanism by allowing dissipations of intracranial pulsations before they are able to reach the microcirculation.

The model predicts pulsatile cranial and spinal CSF flow with zero net flow. During a cardiac cycle, the total cerebral blood volume was found to inflate and deflate by approximately 0.26 mL whereas 0.26 mL of CSF volume was displaced into the spinal sas. Cranial CSF pressure was found to be steady accross the cranial sas and equal to 8 mmHg. Finally, the model predicts venous volume compression and spinal CSF dilation acting as a buffering mechanism to arterial volume expansion. Our model supports CSF crucial role in regulating cerebral volume expansion during the cardiac cycle.

In the second section, we have shown that an optimum CSF peak flow and srtoke volume occured at a intracranial CSF volume of 133 mL which corresponds to a mean physiological value of CSF volume. This optimum was demonstrated to be due to the imbalance forces between the inertial forces and the viscous forces. Thus, viscous dissipation of CSF flow have shown to have a major effect on CSF peak flow an pulse pressure.

In the third and fourth section, our model demonstrates that cranial and cervical flows are strongly impacted by intracranial and spinal compliance of the sas. Cervical CSF and jugular peak flow were found to occur earlier when decreasing intracranial compliance of the cranial sas. These results support numerous research and studies hypothesizing that this phase lag may be crucial factor in revealing craniospinal disorders. These results confirm findings in the litterature [6] indicating that in patients with a hydrocephalus condition, cervical CSF flow occured earlier than in healthy volunteers due to decreased intracranial compliance.

Finally, the CSF flow results support that greater spinal sas compliance results in greater CSF flow pwv reduction in the the spinal canal. These indicates that if the spinal sas compliance varies due to surgery involvment, then the CSF peak flow and pulse pressure might be modified.

This study have shown that, the main haemodynamic effects on flow wave propagation can be efficiently captured using a coupled 1D model of blood and CSF flow. However, the results presented emphasize the significant influence of CSF mechanical properties on blood and CSF flow waveforms. The next chapter will discuss the estimation of CSF volume and cranio-spinal compliance parameters in patient-specific simulations.

Chapter 6

Applications on patient specific Data

Sommaire

6.1 Introduction

In the previous chapter, the 1D coupled blood-CSF model have shown a great ability in capturing the main features of blood and CSF flows. However, the medical application of this 1D-modelling is subject to the availability of patient specific data such as pressure wave speeds, flow velocities and anatomical geometries. This is made possible thanks to recent and ongoing progress in medical imaging such as computer tomography, magnetic resonance and ultrasound technologies which offer great possibilities in providing velocity waveforms and local geometries.

In this chapter, CSF pressure and flow computed from the 1D blood-CSF model are compared against PC MRI flow. Four volunteers underwent MRI of the brain: 2 healthy and 2 suspected of a hydrocephalus condition.

This chapter is treated under three main headings. The first section provides the measurements data and their acquisition techniques. The second one explains how the 1D blood-CSF model were adapted using these data measurements. The third part consists of analysing and comparing CSF flow and pressure in vivo measurements against computationel outputs. The aim of using patient specific data is first to validate the outcomes of the coupled 1D blood-CSF model and hopefully provide insights by estimating major mechanical properties of patients.

Mean flow (mL/s)	RIC	LIC	RV	LV	RJ	LJ	AQ	C2-C3	4V	PC	ImB
N-1	5.7	5.6	0.6	0.9	0.3	7	0.02	0.05	0.01	-0.06	5.5
N-2	4.6	3.8	1.2	2.3	9.5	2	0.01	-0.02	-0.01	-0.3	0.4
H-1	2.1	3.3	0.6	1.5	5.4	1.3	$10^{-}3$	-0.05	0.03	0.08	0.8
H-2	3.2	3.7	0.2	0.3	1	1.5	-0.04	-0.02	0.02	0.07	4.9

Table 6.1: Mean blood and CSF flow

Section (cm^2)	RIC	LIC	RV	LV	RJ	LJ	AQ	C2-C3	4V	PC
N-1	0.22	0.27	0.05	0.06	0.08	0.41	0.04	1.2	0.08	1.4
N-2	0.25	0.21	0.12	0.15	0.65	0.1	0.08	1	0.03	1.1
H-1	0.16	0.2	0.07	0.11	0.58	0.19	0.07	1.3	0.04	1.6
H-2	0.22	0.23	0.03	0.03	0.06	0.07	0.05	2.1	0.01	1.5

Table 6.2: Section of blood and CSF

6.2 Data aquisition

Conventional morphologic sequences and PC-MRI measurements were acquired from *Bio FLow Image* Project directed by Phd Olivier Balédent at Amiens University in France using in-house image-processing software that automatically measured flow curves. The MRI measurements methods are detailed in Baledent et al. [5]. CSF flow acquisition was acquired through the C2-C3 subarachnoid space, the fourth ventricular, the aqueduct of Sylvius and the prepontine cistern. Section through C2 to C3 were selected to measure axial vascular flow at the right and left internal carotid (RIC and LIC) and right and left vertebral arteries (RV and LV) and in the right and left internal jugular veins (RJ and LJ). Two healthy volunteers and two patients suspected of a hydrocephalic disorder were investigated. The latter two patients are part of *proliphyc* project directed by neurosurgeon Dr. Eric Schmidt. *proliphyc* which aims to investigate the link between the CSF proteome (set of proteins) and neurological disorders.

Remarque 6.1
The following subscripts will be used in the following. RIC denotes for Right Internal Carotid, LIC for Left Internal Carotid, RV for Right Vertebral, LV for Left Vertebral, RJ for Right Jugular, LJ for Left Jugular, AQ for CSF Aqueduct region, C2-C3 for CSF second and third cervical region, 4V for fourth ventricle and PC for the Prepontine Cistern. N denotes for Normal CSF flow and H for suspected Hydrocephalus flow.

6.3 Patient specific 1D blood-CSF model

In the previous chapter, the boundary conditions used for the computations were blood pressure signals for the input and the ouput of the cerebral vasculature. The input pressure was assigned respectively a sinusoidal pressure and a more physiological one. It was imposed at the inlet of the carotids and the vertebrals artries. A steady pressure signal was imposed at

the outlet of the jugular veins. Here PC-MRI measurements were used as boundary conditions.

Table (6.1) and table (6.2) resume respectively mean flow and sections in each artery, vein and CSF region. Although, it is a small control population, it illustrates heterogeneity and dispersion of mean venous flow. Stoquart-El Sankari et al. [69] performed PC-MRI in 18 healthy volunteers in the supine position and showed that jugular outflow tends to favor the right jugular vein.

The last column *ImB* consist of the imbalance between arterial net flow and jugular net flow. This imbalance is described by several authors and is presumably due to accessory venous drainage pathways besides the jugular veins [19, 59, 69, 64]. In the supine posture, the venous outflow is primarily through the IJV while in the upright posture the IJV's were either partially or fully collapsed and the main pathway for venous drainage was the cerebral venous plexus. Usually in medical imaging, to account for this imbalance in order to produce an arteriovenous flow, which consists of the difference between the measured arterial curve and the measured venous curve, the venous outflow is scaled using a corrected factor, α, as α= mean arterial flow/mean venous flow [24, 5]. Venous outflow is therefore forced to equal arterial inflow.

In this study, to ensure a mass conservation between the arterial inflow and the jugular outflow. We have taken profit from vessel 6bis, which may act as an accessory venous drainage to impose at its boundary the imbalance between the measured arterial and jugular flow.

6.4 CSF network parameters

In the previous chapter, effect of the CSF network parameters were investigated. They consisted of the cranial CSF confinement or CSF volume, the spinal and cranial dura mater elastic modulus or in other words, the cranial and spinal sas compliance. In this chapter, cranial CSF confinement was taken ranged between $\lambda_{cb} = 0.1$ and $\lambda_{cb} = 0.85$. The cranial and spinal compliance was taken individually varying between 75 mmHg and $7.5.10^4$ mmHg which correponds to a cranial and spinal sas compliance varying between 0.002 and 2 mL/mmHg.

6.5 Comparison between PC-MRI flow and 1D model flow

PC-MRI C2-C3 CSF flow discrete signal is compared against computed C2-C3 CSF flow by means of normalised root mean square error, *nrmse*. It is defined as,

$$nrmse = \frac{\sqrt{\frac{\sum_{n=1}^{n=N}(Q_{mri}^n - Q_m^n)^2}{N}}}{\frac{\sum_{n=1}^{n=N}(Q_{mri}^n)^2}{N}} \tag{6.1}$$

where Q_{mri} is the measured PC-MRI flow, Q_m is the computed flow, N the number of samples of the signals. For example, a nrmse of 0.6 means a difference between measured and computed signal of 60%.

After running the simulations for various CSF volume and cranio-spinal compliance, the C2-C3 cervical flow having the smallest *nrmse* were extracted. They are displayed in figure (6.1). Table 6.3 resumes the deduced *nrmse*, CSF volume, cranial and spinal sas compliance and pulse wave velocity in the spinal canal.

Overall, general aspect of computed flow is in good agreement of the measured flow. Judging by the *nrmse* deviations, normal patients have shown better similarity than suspected hydrocephalic patients. Moreover, H2 patient had a significant CSF volume and a higher intracranial compliance. Finally, spinal compliance was found slightly higher in the hydrocephalic patients.

	nrmse	CSF volume (mL)	Intracranial sas compliance (mL/mmHg)	Spinal sas compliance (mL/mmHg)	spinal pwv (m/s)
N-1	0.36	164	$8.5.10^{-4}$	0.0951	6.5
N-2	0.46	153	$8.5.10^{-4}$	0.0847	11
H-1	0.68	148	5.10^{-4}	0.1042	7.7
H-2	0.63	314	0.0025	0.159	8.9

Table 6.3: Computed *nrmse*, CSF volume, cranial and spinal sas compliance and pulse wave velocity in the spinal canal for 4 patients

6.6 Conclusion

We have proposed a methodology and a strategy which uses MRI and geometry data of the carotid and vertebrals arteries to compute cervical CSF flow. Although, the number of individuals investigated was relatively small, comparison between computed CSF flow and MRI have shown good agreement. Results are promising but the control population is too small to provide conclusive remarks and suggest a clinical status of the patients. Quite likely, the cranio-spinal compliance is not the only issue involved in Hydrocephalus disorders as some forms are caused by altered CSF absorption at the arachnoid granulations. Nevertheless, it demonstrates the potential of the proposed 1d model for the investigation of CSF dynamics.

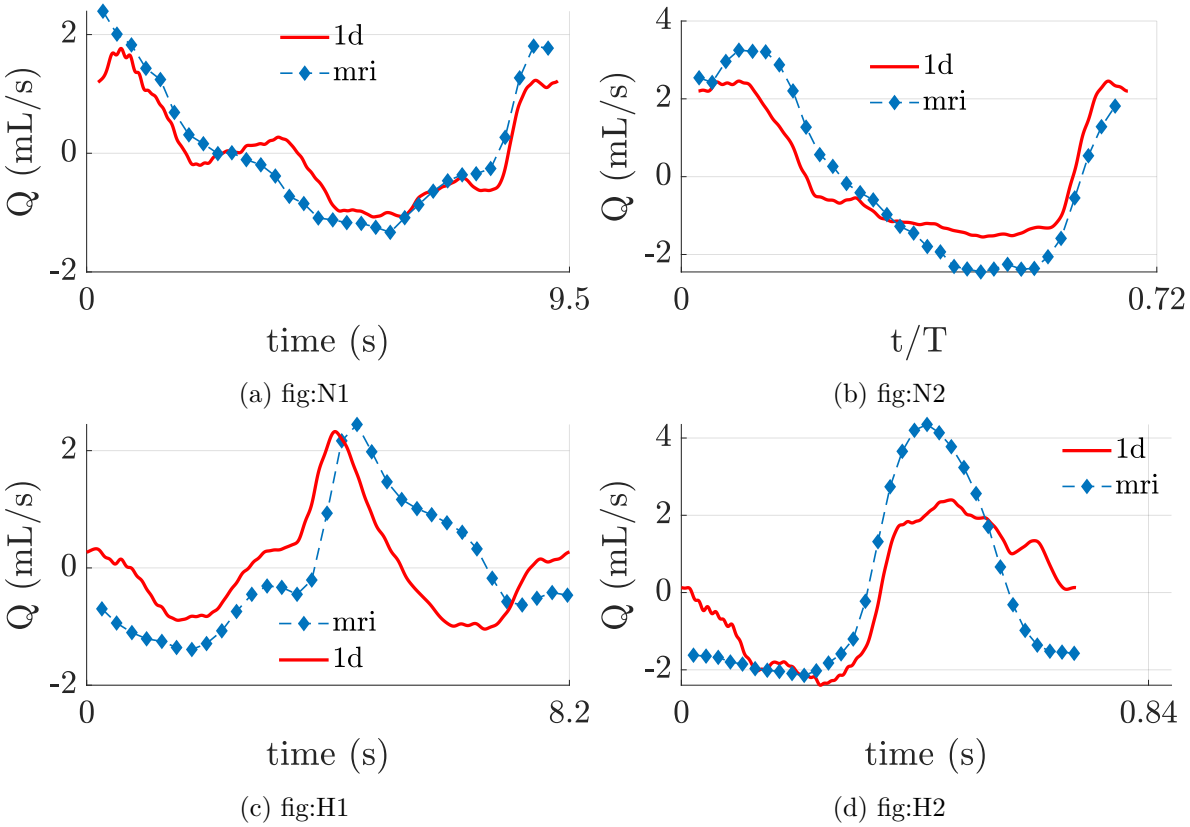

(a) fig:N1

(b) fig:N2

(c) fig:H1

(d) fig:H2

Figure 6.1: Cervical CSF flow computed from the current model and compared to measured PC-MRI flow

Conclusion and perspectives

6.7 Conclusion

The cerebrospinal fluid is a biological fluid embedded within the central nervous system. The fluid exhibits clear pulsatile motion superimposed by a bulk flow due to its production and absorption. MRI studies suggest that arterial pulsations and respiration are the main driving mechanisms behind CSF motion. In this work, we have focused on the arterial pulsations effect as the CSF motor function .

In the first chapter, we have first established a strong and necessary background of the central nervous system anatomy. We have given a particular attention to the CSF system which includes the ventricular system and the cranial and spinal subarachnoid spaces. Furthermore, we have described the brain blood supply and drainage and outlined the high variability of the cerebral vasculature architecture.

In the second chapter, we have described the geometry and mechanical properties of the proposed one-dimensional model. It consists in the cranial vault of the brain vasculature starting at the paired carotid and vertebral arteries and ending at the jugular veins. The blood vessels were enclosed within coaxial tubes representing the cranial subarachnoid spaces. The cranial vault was later coupled to a spinal compartment in which the spinal subarachnoid spaces encloses the spinal cord.

In the third chapter, we have established the one dimensional formulation of flow in a system of coaxial and compliant tubes. We have presented the Lax Wendroff numerical scheme and highlighted the branching conditions involved in the one dimensional architecture.

In the fourth chapter, we have explored the effect of accounting CSF pulsations on blood pulsations. Furthermore, we have quantified the effect of CSF volume and the cranio-spinal compliance on CSF flow dynamics. Our model was able to evidence cranial CSF pulsatility with zero net flow and CSF motion between the cranial and spinal compartments. The model predictions of CSF flow were in good agreement with clinical findings both in flow amplitude and stroke volume at the cervical region. The model have demonstrated a CSF volume at which CSF peak flow and stroke volume were optimal. Moreover, decreasing the cranio-spinal compliance have shown to increase cranial CSF pressure whereas peak cervical flow time delay was found to decrease. In the spinal compartment, the model predicted pulse wave velocity values in the ranges of previous MRI work.

Therefore, in the last chapter, we have compared the cervical CSF flow of our model to PC-MRI flow of 2 healthy patients and 2 patients with suspected hydrocephalus. The model showed good agreement with the measured flow but was unable to provide further insights regarding the medical status of the patients.

6.8 Perspectives

There remains some aspects on which future work might shed the lights upon. We suggest further investigations upon the following matters. Future studies might expand the ventricular system by taking into account aqueducts, ventricles and cisterns and therefore explores further coupling due to arterial pulsations. Later studies might also address the coupling between the spinal vasculature as the epidural vein plexus and spinal CSF flow. The latter has shown to largely influence CSF flow and pressure during abrupt increase of abdominal pressure like coughing or sneezing. Moreover, the current model is based on a constant section of the spinal subarachnoid spaces and spinal cord, although the spinal compartment shows a varying cross sectional area of both the spinal subarachnoid spaces and the spinal cord with an enlargement at the cervical and lumbar region. Cross sectional variations might bring an improvement to the current model in terms of pulse wave velocity and pulse pressure attenuation.

Much work remains to be done in expanding the model, but the integration of the major components of blood and CSF appears to provide a good start into understanding intracranial dynamics.

Appendix A

Wall shear stresses in an annular flow

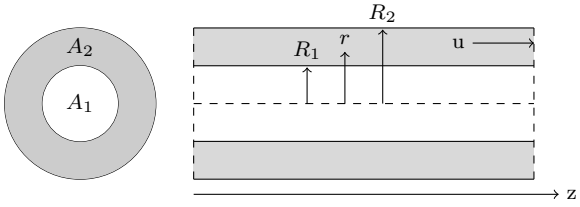

For a laminar flow in a cricular pipe, the pressure gradient is defined as,

$$\frac{\mathrm{d}P}{\mathrm{d}z} = \mu \frac{1}{r} \frac{\mathrm{d}}{\mathrm{d}r} \left(r \frac{\mathrm{d}u}{\mathrm{d}r} \right) \tag{A.1}$$

Following several derivations of the previous equation, we obtain the following expression of the longitudinal velocity u :

$$u = \frac{r^2}{4\mu} \frac{\mathrm{d}P}{\mathrm{d}z} + A \ln r + B \tag{A.2}$$

where A and B are derivatives constants.

In a annular flow, the no slip boundary conditions are written as:

$$\begin{cases} u_{(r=R_1)} = 0 & \text{(A.3)} \\ u_{(r=R_2)} = 0 & \text{(A.4)} \end{cases}$$

By replacing the latter equations in the longitudinal velocity expression A.2, we obtain the following system of equations :

$$\begin{cases} \frac{R_1^2}{4\mu} \frac{dP}{dz} + A \ln R_1 + B = 0 & \text{(A.5)} \\ \frac{R_2^2}{4\mu} \frac{dP}{dz} + A \ln R_2 + B = 0 & \text{(A.6)} \end{cases}$$

The resolution of this system allows to obtain the expressions of A et B which are :

$$\begin{cases} A = \dfrac{1}{4\mu}\dfrac{\mathrm{d}P}{\mathrm{d}z}\dfrac{R_1^2 - R_2^2}{\ln\frac{R_2}{R_1}} & \text{(A.7)} \\ B = \dfrac{1}{4\mu}\dfrac{\mathrm{d}P}{\mathrm{d}z}\left(-R_2^2 - \dfrac{R_1^2 - R_2^2}{\ln\frac{R_2}{R_1}}\ln R_2\right) & \text{(A.8)} \end{cases}$$

By replacing the latter equations in the longitudinal velocity expression A.2, the expression of u becomes :

$$u = \frac{1}{4\mu}R_2^2\frac{\mathrm{d}P}{\mathrm{d}z}\left(\left(\frac{r}{R_2}\right)^2 - 1 + \frac{1-\lambda^2}{\ln\lambda}\ln\frac{r}{R_2}\right) \tag{A.9}$$

where

$$a = \frac{R_2^2 - R_1^2}{\ln\frac{R_2}{R_1}}\lambda = \frac{R_1}{R_2}$$

Now, we will proceide at defining the mean velocity denoted U. Its expression is,

$$U = \frac{1}{\text{Annular section}}\int u\mathrm{d}S = \frac{1}{\pi(R_2^2 - R_1^2)}\int_{R_1}^{R_2} u2\pi r\mathrm{d}r$$

After multiple calculations and a partial integration, the expression of the mean velocity U becomes :

$$U = -\frac{1}{8\mu}R_2^2\frac{\mathrm{d}P}{\mathrm{d}z}\left(1 + \lambda^2 + \frac{1-\lambda^2}{\ln\lambda}\right)$$

From expressions A.9 et A.9, we deduce the algebraic relation linking the longitudinal velocity u to the mean velocity U :

$$u = 2U\left(\frac{1 - \left(\frac{r}{R_2}\right)^2 - \frac{1-\lambda^2}{\ln\lambda}\ln\frac{r}{R_2}}{1 + \lambda^2 + \frac{1-\lambda^2}{\ln\lambda}}\right)$$

Finally, let τ_{p1} and τ_{p2} be the wall shear stresses respectively at $r = R_1$ and $r = R_2$. Their expressions may be written as :

$$\begin{cases} \tau_{p1} = \tau_{p_{(r=R_1)}} = \mu\left(\dfrac{\mathrm{d}u}{\mathrm{d}r}\right)_{R_1} & \text{(A.10)} \\ \tau_{p2} = \tau_{p_{(r=R_2)}} = \mu\left(\dfrac{\mathrm{d}u}{\mathrm{d}r}\right)_{R_2} & \text{(A.11)} \end{cases}$$

In other words, after integrating the expression u, the wall shear stresses τ_{p1} and τ_{p2}

becomes :

$$\begin{cases} \tau_{ps1} = \dfrac{2\mu U}{\gamma}\left(\dfrac{2R_1}{R_2^2} + \dfrac{1-\lambda^2}{R_1 \ln \lambda}\right) & \text{(A.12)} \\ \tau_{ps2} = \dfrac{2\mu U}{\gamma}\left(\dfrac{2}{R_2} + \dfrac{1-\lambda^2}{R_2 \ln \lambda}\right) & \text{(A.13)} \end{cases}$$

where

$$\gamma = 1 + \lambda^2 + \frac{1-\lambda^2}{\ln \lambda}$$

Appendix B

Branching conditions

The following subscripts are used : 1 for the interior tube and 2 for the exterior tube.

B.0.0.1 Case 2

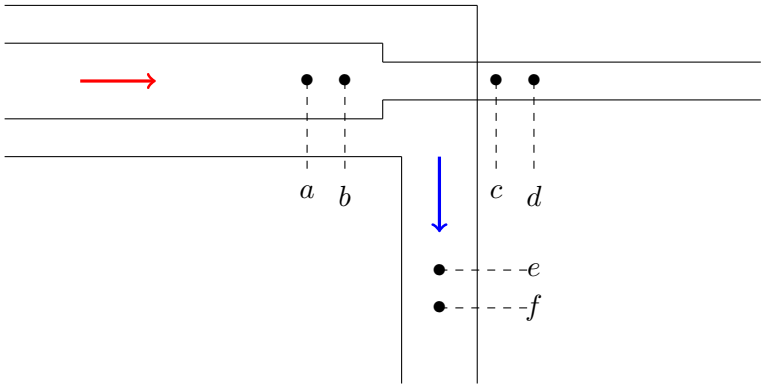

The jump conditions between the points b, c and e are :

$$(AU)_{1b} = (AU)_{1c} \tag{B.1}$$

$$((A_2 - A_1)U_2)_b = (AU)_{2e} \tag{B.2}$$

$$P_{1b} = P_{1c}$$

$$P_{2b} = P_{2e}$$

$$P_{1b} = El_{1b}\left(\frac{A_{1b}}{A_{01b}} - 1\right) + P_{2b} \tag{B.3}$$

$$P_{1c} = El_{1c}\left(\frac{A_{1c}}{A_{01c}} - 1\right) \tag{B.4}$$

$$P_{2b} = El_{2b}\left(\frac{A_{2b}}{A_{02b}} - 1\right) \tag{B.5}$$

$$P_{2e} = El_{2e}\left(\frac{A_{2e}}{A_{02e}} - 1\right) \tag{B.6}$$

$$\int_a^b \frac{\partial A_1}{\partial t}\mathrm{d}x + (AU)_{1b}^{n+1} - (AU)_{1a}^{n+1} = 0 \tag{B.7}$$

$$\int_c^d \frac{\partial A_1}{\partial t}\mathrm{d}x + (AU)_{1d}^{n+1} - (AU)_{1c}^{n+1} = 0 \tag{B.8}$$

$$\int_e^f \frac{\partial A_2}{\partial t}\mathrm{d}x + (AU)_{2f}^{n+1} - (AU)_{2e}^{n+1} = 0 \tag{B.9}$$

$$\int_a^b \frac{\partial A_2}{\partial t}\mathrm{d}x + \Big((A_2 - A_1)U_2 + A_1U_1)_b^{n+1} - ((A_2 - A_1)U_2 + A_1U_1)\Big)_a^{n+1} = 0 \tag{B.10}$$

Therefore,

$$\frac{\Delta x_a}{2\Delta t_a}\left(A_{1a}^{n+1} - A_{1a}^n + A_{1b}^{n+1} - A_{1b}^n\right) + (AU)_{1b}^{n+1} - (AU)_{1a}^{n+1} = 0 \tag{B.11}$$

$$\frac{\Delta x_d}{2\Delta t_d}\left(A_{1d}^{n+1} - A_{1d}^n + A_{1c}^{n+1} - A_{1c}^n\right) + (AU)_{1d}^{n+1} - (AU)_{1c}^{n+1} = 0 \tag{B.12}$$

$$\begin{aligned}&\frac{\Delta x_a}{2\Delta t_a}\left(A_{2a}^{n+1} - A_{2a}^n + A_{2b}^{n+1} - A_{2b}^n\right) + ((A_2 - A_1)U_2 + A_1U_1)_b^{n+1}\\ &- ((A_2 - A_1)U_2 + A_1U_1))_a^{n+1} = 0\end{aligned} \tag{B.13}$$

$$\frac{\Delta x_f}{2\Delta t_f}\left(A_{2f}^{n+1} - A_{2f}^n + A_{2e}^{n+1} - A_{2e}^n\right) + (AU)_{2f}^{n+1} - (AU)_{2e}^{n+1} = 0 \tag{B.14}$$

Given that,

$$A_{2e}^{n+1} - A_{2e}^n = \frac{El_{2b}}{El_{2e}}\frac{A_{02e}}{A_{02b}}(A_{2b}^{n+1} - A_{2b}^n) \tag{B.15}$$

$$A_{1c}^{n+1} - A_{1c}^n = \frac{El_{1b}}{El_{1c}}\frac{A_{01c}}{A_{01b}}(A_{1b}^{n+1} - A_{1b}^n) + \frac{El_{2b}}{El_{1c}}\frac{A_{01c}}{A_{02b}}(A_{2b}^{n+1} - A_{2b}^n) \tag{B.16}$$

Put,

$$R_a = \left(\frac{\Delta x_a}{2\Delta t_a}\right), \qquad R_d = \left(\frac{\Delta x_d}{2\Delta t_d}\right), \qquad R_f = \left(\frac{\Delta x_f}{2\Delta t_f}\right)$$

$$K_{1bc} = \frac{El_{1b}}{El_{1c}}\frac{A_{01c}}{A_{01b}}, \qquad K_{2be} = \frac{El_{2b}}{El_{2e}}\frac{A_{02e}}{A_{02b}}, \qquad K_{2b1c} = \frac{El_{2b}}{El_{1c}}\frac{A_{01c}}{A_{02b}}$$

By adding (B.11) and (B.12) and using (B.1) and (B.16),

$$\begin{aligned}&[R_a + R_dK_{1bc}](A_{1b}^{n+1} - A_{1b}^n) + R_dK_{2b1c}(A_{2b}^{n+1} - A_{2b}^n)\\ &= -R_a(A_{1a}^{n+1} - A_{1a}^n) - R_d(A_{1d}^{n+1} - A_{1d}^n) + (AU)_{1a}^{n+1} - (AU)_{1d}^{n+1}\end{aligned} \tag{B.17}$$

By substracting equation (B.12) from (B.11),

$$\begin{aligned}(AU)_{1b}^{n+1} &= \frac{1}{2}(-[R_a - R_dK_{1bc}](A_{1b}^{n+1} - A_{1b}^n) + R_dK_{2b1c}(A_{2b}^{n+1} - A_{2b}^n)\\ &- R_a(A_{1a}^{n+1} - A_{1a}^n) + R_d(A_{1d}^{n+1} - A_{1d}^n) + (AU)_{1a}^{n+1} + (AU)_{1d}^{n+1})\end{aligned} \tag{B.18}$$

By adding (B.13) and (B.14) and using (B.2) and (B.15),

$$[R_a + R_f K_{2be}](A_{2b}^{n+1} - A_{2b}^n) + R_f(A_{2f}^{n+1} - A_{2f}^n) + R_a(A_{2a}^{n+1} - A_{2a}^n) + (AU)_{2f}^{n+1} + (AU)_{1b}^{n+1} - ((A_2 - A_1)U_2 + A_1U_1))_a^{n+1} = 0 \tag{B.19}$$

By replacing (B.18) in (B.19),

$$\begin{aligned}[\frac{-R_a}{2} + \frac{R_d K_{1bc}}{2}](A_{1b}^{n+1} - A_{1b}^n) + [R_a + R_f K_{2be} + \frac{R_d K_{2b1c}}{2}](A_{2b}^{n+1} - A_{2b}^n) \\ = \frac{R_a}{2}(A_{1a}^{n+1} - A_{1a}^n) - \frac{R_d}{2}(A_{1d}^{n+1} - A_{1d}^n) - \frac{(AU)_{1a}^{n+1}}{2} - \frac{(AU)_{1d}^{n+1}}{2} \\ - R_f(A_{2f}^{n+1} - A_{2f}^n) - R_a(A_{2a}^{n+1} - A_{2a}^n) - (AU)_{2f}^{n+1} \\ + ((A_2 - A_1)U_2 + A_1U_1))_a^{n+1}\end{aligned} \tag{B.20}$$

Using equations (B.17) and (B.20),

$$\begin{pmatrix} A_{1b}^{n+1} - A_{1b}^n \\ A_{2b}^{n+1} - A_{2b}^n \end{pmatrix} = M^{-1} \begin{pmatrix} Z_1 \\ Z_2 \end{pmatrix} \tag{B.21}$$

with,

$$M = \begin{pmatrix} R_a + R_d K_{1bc} & R_d K_{2b1c} \\ \frac{-R_a}{2} + \frac{R_d K_{1bc}}{2} & R_a + R_f K_{2be} + \frac{R_d K_{2b1c}}{2} \end{pmatrix}$$

And,

$$Z_1 = -R_a(A_{1a}^{n+1} - A_{1a}^n) - R_d(A_{1d}^{n+1} - A_{1d}^n) + (AU)_{1a}^{n+1} - (AU)_{1d}^{n+1}$$

$$\begin{aligned}Z_2 =& \frac{R_a}{2}(A_{1a}^{n+1} - A_{1a}^n) - \frac{R_d}{2}(A_{1d}^{n+1} - A_{1d}^n) - \frac{(AU)_{1a}^{n+1}}{2} - \frac{(AU)_{1d}^{n+1}}{2} \\ & - R_f(A_{2f}^{n+1} - A_{2f}^n) - R_a(A_{2a}^{n+1} - A_{2a}^n) - (AU)_{2f}^{n+1} \\ & + ((A_2 - A_1)U_2 + A_1U_1))_a^{n+1}\end{aligned}$$

By susbstracting (B.14) from (B.13), we obtain

$$[R_a - R_f K_{2be}](A_{2b}^{n+1} - A_{2b}^n) + R_a(A_{2a}^{n+1} - A_{2a}^n) - R_f(A_{2f}^{n+1} - A_{2f}^n) + 2\,(AU)_{2e}^{n+1} - (AU)_{2f}^{n+1} + (AU)_{1b}^{n+1} - ((A_2 - A_1)U_2 + A_1U_1))_a^{n+1} = 0$$

Therefore,

$$U_{2e}^{n+1} = \frac{1}{2A_{2e}^{n+1}}(-[R_a - R_f K_{2be}](A_{2b}^{n+1} - A_{2b}^n) - R_a(A_{2a}^{n+1} - A_{2a}^n) \tag{B.22}$$

$$+ R_f(A_{2f}^{n+1} - A_{2f}^n) + (AU)_{2f}^{n+1} - (AU)_{1b}^{n+1} + ((A_2 - A_1)U_2 + A_1U_1))_a^{n+1}) \tag{B.23}$$

From equation (B.21), we obtain A_{1b}^{n+1} and A_{2b}^{n+1}.

From equation (B.3) and (B.5) ,we obtain P_{1b}^{n+1} and P_{2b}^{n+1}. Immediately, we obtain P_{1c}^{n+1} and P_{2e}^{n+1}.
From equation (B.4) and (B.6) ,we obtain A_{1c}^{n+1} and A_{2e}^{n+1}.
From equation (B.11) or (B.18), we obtain U_{1b}^{n+1}.
From equation (B.12) or (B.1), we obtain U_{1c}^{n+1}.
From equation (B.14) or (B.23), we obtain U_{2e}^{n+1}.
From equation (B.13) or(B.2), we obtain U_{2b}^{n+1}.

B.0.0.2 case 3

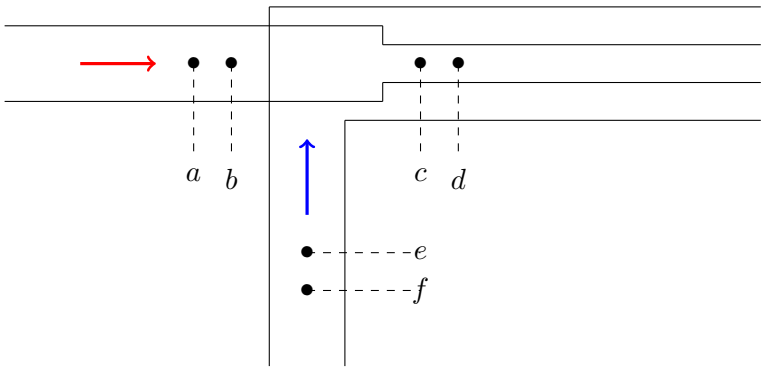

The jump conditions between the points b, c and e are :

$$(AU)_{1b} = (AU)_{1c} \tag{B.24}$$

$$(AU)_{2e} = [(A_2 - A_1)U_2]_c \tag{B.25}$$

$$P_{1b} = P_{1c}$$

$$P_{2e} = P_{2c}$$

$$P_{1b} = El_{1b}\left(\frac{A_{1b}}{A_{01b}} - 1\right) \tag{B.26}$$

$$P_{1c} = El_{1c}\left(\frac{A_{1c}}{A_{01c}} - 1\right) + P_{2c} \tag{B.27}$$

$$P_{2c} = El_{2c}\left(\frac{A_{2c}}{A_{02c}} - 1\right) \tag{B.28}$$

$$P_{2e} = El_{2e}\left(\frac{A_{2e}}{A_{02e}} - 1\right) \tag{B.29}$$

Given that,

$$\int_a^b \frac{\partial A_1}{\partial t}\mathrm{d}x + (AU)_{1b}^{n+1} - (AU)_{1a}^{n+1} = 0 \tag{B.30}$$

$$\int_f^e \frac{\partial A_2}{\partial t}\mathrm{d}x + (AU)_{2e}^{n+1} - (AU)_{2f}^{n+1} = 0 \tag{B.31}$$

$$\int_c^d \frac{\partial A_1}{\partial t}\mathrm{d}x + (AU)_{1d}^{n+1} - (AU)_{1c}^{n+1} = 0 \tag{B.32}$$

$$\int_c^d \frac{\partial A_2}{\partial t}\mathrm{d}x + \Big((A_2 - A_1)U_2 + A_1U_1)_d^{n+1} - ((A_2 - A_1)U_2 + A_1U_1)\Big)_c^{n+1} = 0 \tag{B.33}$$

Therefore,

$$\frac{\Delta x_a}{2\Delta t_a}\left(A_{1a}^{n+1} - A_{1a}^n + A_{1b}^{n+1} - A_{1b}^n\right) + (AU)_{1b}^{n+1} - (AU)_{1a}^{n+1} = 0 \tag{B.34}$$

$$\frac{\Delta x_f}{2\Delta t_f}\left(A_{2f}^{n+1} - A_{2f}^n + A_{2e}^{n+1} - A_{2e}^n\right) + (AU)_{2e}^{n+1} - (AU)_{2f}^{n+1} = 0 \tag{B.35}$$

$$\frac{\Delta x_d}{2\Delta t_d}\left(A_{1d}^{n+1} - A_{1d}^n + A_{1c}^{n+1} - A_{1c}^n\right) + (AU)_{1d}^{n+1} - (AU)_{1c}^{n+1} = 0 \tag{B.36}$$

$$\begin{aligned}&\frac{\Delta x_d}{2\Delta t_d}\left(A_{2d}^{n+1} - A_{2d}^n + A_{2c}^{n+1} - A_{2c}^n\right) + ((A_2 - A_1)U_2 + A_1U_1)_d^{n+1}\\ &- ((A_2 - A_1)U_2 + A_1U_1))_c^{n+1} = 0\end{aligned} \tag{B.37}$$

Given that,

$$A_{2c}^{n+1} - A_{2c}^n = \frac{El_{2e}}{El_{2c}}\frac{A_{02c}}{A_{02e}}(A_{2e}^{n+1} - A_{2e}^n) \tag{B.38}$$

$$A_{1c}^{n+1} - A_{1c}^n = \frac{El_{1b}}{El_{1c}}\frac{A_{01c}}{A_{01b}}(A_{1b}^{n+1} - A_{1b}^n) - \frac{El_{2e}}{El_{1c}}\frac{A_{01c}}{A_{02e}}(A_{2e}^{n+1} - A_{2e}^n) \tag{B.39}$$

Put,

$$R_a = \left(\frac{\Delta x_a}{2\Delta t_a}\right), \qquad R_d = \left(\frac{\Delta x_d}{2\Delta t_d}\right), \qquad R_f = \left(\frac{\Delta x_f}{2\Delta t_f}\right)$$

$$K_{1bc} = \frac{El_{1b}}{El_{1c}}\frac{A_{01c}}{A_{01b}}, \qquad K_{2ec} = \frac{El_{2e}}{El_{2c}}\frac{A_{02c}}{A_{02e}}, \qquad K_{2e1c} = \frac{El_{2e}}{El_{1c}}\frac{A_{01c}}{A_{02e}}$$

By adding (B.34) and (B.36) and using (B.24) and (B.39),

$$\begin{aligned}&[R_a + R_dK_{1bc}](A_{1b}^{n+1} - A_{1b}^n) - R_dK_{2e1c}(A_{2e}^{n+1} - A_{2e}^n)\\ &= -R_a(A_{1a}^{n+1} - A_{1a}^n) - R_d(A_{1d}^{n+1} - A_{1d}^n) + (AU)_{1a}^{n+1} - (AU)_{1d}^{n+1}\end{aligned} \tag{B.40}$$

By substracting equation (B.36) from (B.34),

$$\begin{aligned}&[R_a - R_dK_{1bc}](A_{1b}^{n+1} - A_{1b}^n) + R_dK_{2e1c}(A_{2e}^{n+1} - A_{2e}^n) + R_a(A_{1a}^{n+1} - A_{1a}^n)\\ &- R_d(A_{1d}^{n+1} - A_{1d}^n) - (AU)_{1a}^{n+1} - (AU)_{1d}^{n+1} + 2(AU)_{1c}^{n+1}) = 0\end{aligned} \tag{B.41}$$

Therefore,

$$(AU)_{1c}^{n+1} = \frac{1}{2}(-[R_a - R_d K_{1bc}](A_{1b}^{n+1} - A_{1b}^{n}) - R_d K_{2e1c}(A_{2e}^{n+1} - A_{2e}^{n}) \\ - R_a(A_{1a}^{n+1} - A_{1a}^{n}) + R_d(A_{1d}^{n+1} - A_{1d}^{n}) + (AU)_{1a}^{n+1} + (AU)_{1d}^{n+1} \tag{B.42}$$

By adding (B.35) and (B.37) and using (B.25) and (B.38),

$$[R_f + R_d K_{2ec}](A_{2e}^{n+1} - A_{2e}^{n}) + R_f(A_{2f}^{n+1} - A_{2f}^{n}) + R_d(A_{2d}^{n+1} - A_{2d}^{n}) \\ - (AU)_{2f}^{n+1} - (AU)_{1c}^{n+1} + ((A_2 - A_1)U_2 + A_1U_1))_d^{n+1} = 0 \tag{B.43}$$

By replacing (B.42) in (B.43),

$$[\frac{R_a}{2} - \frac{R_d K_{1bc}}{2}](A_{1b}^{n+1} - A_{1b}^{n}) + [R_f + R_d K_{2ec} + \frac{R_d K_{2e1c}}{2}](A_{2e}^{n+1} - A_{2e}^{n}) \\ = -\frac{R_a}{2}(A_{1a}^{n+1} - A_{1a}^{n}) + \frac{R_d}{2}(A_{1d}^{n+1} - A_{1d}^{n}) + \frac{(AU)_{1a}^{n+1}}{2} + \frac{(AU)_{1d}^{n+1}}{2} \\ - R_f(A_{2f}^{n+1} - A_{2f}^{n}) - R_d(A_{2d}^{n+1} - A_{2d}^{n}) + (AU)_{2f}^{n+1} \\ - ((A_2 - A_1)U_2 + A_1U_1))_d^{n+1} \tag{B.44}$$

Using equations (B.40) and (B.44),

$$\begin{pmatrix} A_{1b}^{n+1} - A_{1b}^{n} \\ A_{2e}^{n+1} - A_{2e}^{n} \end{pmatrix} = M^{-1} \begin{pmatrix} Z_1 \\ Z_2 \end{pmatrix} \tag{B.45}$$

with,

$$M = \begin{pmatrix} R_a + R_d K_{1bc} & -R_d K_{2e1c} \\ \frac{R_a}{2} - \frac{R_d K_{1bc}}{2} & R_f + R_d K_{2ec} + \frac{R_d K_{2e1c}}{2} \end{pmatrix}$$

And,

$$Z_1 = -R_a(A_{1a}^{n+1} - A_{1a}^{n}) - R_d(A_{1d}^{n+1} - A_{1d}^{n}) + (AU)_{1a}^{n+1} - (AU)_{1d}^{n+1}$$

$$Z_2 = -\frac{R_a}{2}(A_{1a}^{n+1} - A_{1a}^{n}) + \frac{R_d}{2}(A_{1d}^{n+1} - A_{1d}^{n}) + \frac{(AU)_{1a}^{n+1}}{2} + \frac{(AU)_{1d}^{n+1}}{2} \\ - R_f(A_{2f}^{n+1} - A_{2f}^{n}) - R_d(A_{2d}^{n+1} - A_{2d}^{n}) + (AU)_{2f}^{n+1} \\ - ((A_2 - A_1)U_2 + A_1U_1))_d^{n+1}$$

By susbstracting (B.37) from (B.35), we obtain

$$[R_f - R_d K_{2ec}](A_{2e}^{n+1} - A_{2e}^{n}) + R_f(A_{2f}^{n+1} - A_{2f}^{n}) - R_d(A_{2d}^{n+1} - A_{2d}^{n}) \\ - (AU)_{2f}^{n+1} - ((A_2 - A_1)U_2 + A_1U_1))_d^{n+1} + (AU)_{1c}^{n+1} + 2\,(AU)_{2e}^{n+1} = 0$$

Therefore,

$$U_{2e}^{n+1} = \frac{1}{2A_{2e}^{n+1}}(-[R_f - R_d K_{2ec}](A_{2e}^{n+1} - A_{2e}^{n}) - R_f(A_{2f}^{n+1} - A_{2f}^{n}) + R_d(A_{2d}^{n+1} - A_{2d}^{n}) + (AU)_{2f}^{n+1} + ((A_2 - A_1)U_2 + A_1U_1))_d^{n+1} - (AU)_{1c}^{n+1}) \quad \text{(B.46)}$$

From equation (B.45), we obtain A_{1b}^{n+1} and A_{2e}^{n+1}.
From equation (B.26) and (B.29) ,we obtain P_{1b}^{n+1} and P_{2e}^{n+1}. Immediately, we obtain P_{1c}^{n+1} and P_{2c}^{n+1}.
From equation (B.27) and (B.28), we obtain A_{1c}^{n+1} and A_{2c}^{n+1}.
From equation (B.36) or (B.42), we obtain U_{1c}^{n+1}.
From equation (B.34) or (B.24), we obtain U_{1b}^{n+1}.
From equation (B.35) or (B.46), we obtain U_{2e}^{n+1}.
From equation (B.37) or (B.25), we obtain U_{2c}^{n+1}.

B.1 A jonction of tubes

B.1.1 Case 1

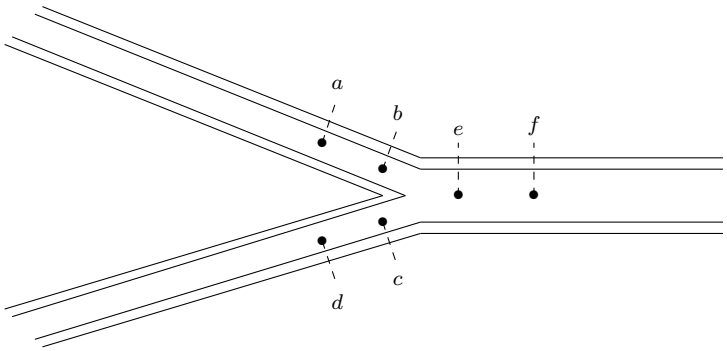

B.1.1.1 Interior tube

For the interior tube, the jump conditions between the points b, c and e are :

$$(AU)_{1b} + (AU)_{1c} = (AU)_{1e} \quad \text{(B.47)}$$

$$P_{1b} = P_{1c} = P_{1e} \quad \text{(B.48)}$$

$$P_{1e} = El_{1e}\left(\frac{A_{1e}}{A_{01e}} - 1\right) + P_{2e} \quad \text{(B.49)}$$

$$P_{1c} = El_{1c}\left(\frac{A_{1c}}{A_{01c}} - 1\right) + P_{2c} \quad \text{(B.50)}$$

$$P_{1b} = El_{1b}\left(\frac{A_{1b}}{A_{01b}} - 1\right) + P_{2b} \tag{B.51}$$

The conservation of mass equation was derived between a and b, d and c, e and f. We obtain :

$$\frac{\Delta x_f}{2\Delta t_f}\left(A_{1f}^{n+1} - A_{1f}^{n} + A_{1e}^{n+1} - A_{1e}^{n}\right) + (AU)_{1f}^{n+1} - (AU)_{1e}^{n+1} = 0 \tag{B.52}$$

$$\frac{\Delta x_a}{2\Delta t_a}\left(A_{1a}^{n+1} - A_{1a}^{n} + A_{1b}^{n+1} - A_{1b}^{n}\right) + (AU)_{1b}^{n+1} - (AU)_{1a}^{n+1} = 0 \tag{B.53}$$

$$\frac{\Delta x_d}{2\Delta t_d}\left(A_{1d}^{n+1} - A_{1d}^{n} + A_{1c}^{n+1} - A_{1c}^{n}\right) + (AU)_{1c}^{n+1} - (AU)_{1d}^{n+1} = 0 \tag{B.54}$$

Given that,

$$A_{1b}^{n+1} - A_{1b}^{n} = \frac{El_{1e}}{El_{1b}}\frac{A_{01b}}{A_{01e}}(A_{1e}^{n+1} - A_{1e}^{n})$$
$$A_{1c}^{n+1} - A_{1c}^{n} = \frac{El_{1e}}{El_{1c}}\frac{A_{01c}}{A_{01e}}(A_{1e}^{n+1} - A_{1e}^{n})$$

Put,

$$R_a = \left(\frac{\Delta x_a}{2\Delta t_a}\right), \qquad R_d = \left(\frac{\Delta x_d}{2\Delta t_d}\right), \qquad R_f = \left(\frac{\Delta x_f}{2\Delta t_f}\right)$$
$$K_{1eb} = \frac{El_{1e}}{El_{1b}}\frac{A_{01b}}{A_{01e}}, \qquad K_{1ec} = \frac{El_{1e}}{El_{1c}}\frac{A_{01c}}{A_{01e}}$$

Adding (B.52), (B.53), (B.54) gives

$$\begin{aligned} A_{1e}^{n+1} = & A_{1e}^{n} + \frac{(AU)_{1a}^{n+1} + (AU)_{1d}^{n+1} - (AU)_{1f}^{n+1} - R_a(A_{1a}^{n+1} - A_{1a}^{n})}{R_f + R_aK_{1eb} + R_dK_{1ec}} \\ & \frac{-R_d(A_{1d}^{n+1} - A_{1d}^{n}) - R_f(A_{1f}^{n+1} - A_{1f}^{n})}{R_f + R_aK_{1eb} + R_dK_{1ec}} \end{aligned} \tag{B.55}$$

Substracting (B.52) from (B.53) and (B.54) gives

$$\begin{aligned} U_{1e}^{n+1} = & \frac{(AU)_{1a}^{n+1} + (AU)_{1d}^{n+1} + (AU)_{1f}^{n+1} - R_a(A_{1a}^{n+1} - A_{1a}^{n}) - R_d(A_{1d}^{n+1} - A_{1d}^{n})}{2A_{1e}^{n+1}} \\ & \frac{+R_f(A_{1f}^{n+1} - A_{1f}^{n}) + (R_f - R_aK_{1eb} - R_dK_{1ec})(A_{1e}^{n+1} - A_{1e}^{n})}{2A_{1e}^{n+1}} \end{aligned} \tag{B.56}$$

B.1.1.2 Exterior tube

For the exterior tube, the jump conditions between the points b, c and e are :

$$((A_2 - A_1)U_2)_b + ((A_2 - A_1)U_2)_c = ((A_2 - A_1)U_2)_e \tag{B.57}$$

$$P_{2b} = P_{2c} = P_{2e} \tag{B.58}$$

$$P_{2e} = El_{2e}\left(\frac{A_{2e}}{A_{02e}} - 1\right) \tag{B.59}$$

$$P_{2b} = El_{2b}\left(\frac{A_{2b}}{A_{02b}} - 1\right) \tag{B.60}$$

$$P_{2c} = El_{2c}\left(\frac{A_{2c}}{A_{02c}} - 1\right) \tag{B.61}$$

The conservation of mass equation was derived between a et b, d et c and e et f. We obtain :

$$\begin{aligned}&\frac{\Delta x_a}{2\Delta t_a}\left(A_{2b}^{n+1} - A_{2b}^{n} + A_{2a}^{n+1} - A_{2a}^{n}\right) + ((A_2 - A_1)U_2 + A_1U_1)_b^{n+1} \\ &- ((A_2 - A_1)U_2 + A_1U_1)_a^{n+1} = 0\end{aligned} \tag{B.62}$$

$$\begin{aligned}&\frac{\Delta x_d}{2\Delta t_d}\left(A_{2d}^{n+1} - A_{2d}^{n} + A_{2c}^{n+1} - A_{2c}^{n}\right) + ((A_2 - A_1)U_2 + A_1U_1)_c^{n+1} \\ &- ((A_2 - A_1)U_2 + A_1U_1)_d^{n+1} = 0\end{aligned} \tag{B.63}$$

$$\begin{aligned}&\frac{\Delta x_f}{2\Delta t_f}\left(A_{2f}^{n+1} - A_{2f}^{n} + A_{2e}^{n+1} - A_{2e}^{n}\right) + ((A_2 - A_1)U_2 + A_1U_1)_f^{n+1} \\ &- ((A_2 - A_1)U_2 + A_1U_1)_e^{n+1} = 0\end{aligned} \tag{B.64}$$

Put,

$$\begin{aligned}\Delta A =& A_2 - A_1, & R_a =& \left(\frac{\Delta x_a}{2\Delta t_a}\right), & R_d =& \left(\frac{\Delta x_d}{2\Delta t_d}\right) \\ R_f =& \left(\frac{\Delta x_f}{2\Delta t_f}\right), & K_{2eb} =& \frac{El_{2e}}{El_{2b}}\frac{A_{02b}}{A_{02e}}, & K_{2ec} =& \frac{El_{2e}}{El_{2c}}\frac{A_{02c}}{A_{02e}}\end{aligned}$$

Adding (B.62), (B.63) and (B.64) gives

$$\begin{aligned}A_{2e}^{n+1} =& A_{2e}^{n} + \frac{(\Delta AU_2 + A_1U_1)_a^{n+1} + (\Delta AU_2 + A_1U_1)_d^{n+1}}{R_f + R_aK_{2eb} + R_dK_{2ec}} \\ &\frac{-(\Delta AU_2 + A_1U_1)_f^{n+1} - R_a(A_{2a}^{n+1} - A_{2a}^{n}) - R_d(A_{2d}^{n+1} - A_{2d}^{n})}{R_f + R_aK_{2eb} + R_dK_{2ec}} \\ &\frac{-R_f(A_{2f}^{n+1} - A_{2f}^{n})}{R_f + R_aK_{2eb} + R_dK_{2ec}}\end{aligned} \tag{B.65}$$

Substracting (B.62), (B.63) from (B.64) gives

$$
\begin{aligned}
U_{2e}^{n+1} = & \frac{(\Delta AU_2 + A_1U_1)_a^{n+1} + (\Delta AU_2 + A_1U_1)_d^{n+1} + (\Delta AU_2 + A_1U_1)_f^{n+1}}{2(A_2 - A_1)_e^{n+1}} \\
& \frac{+R_f(A_{2f}^{n+1} - A_{2f}^n) - R_a(A_{2a}^{n+1} - A_{2a}^n) - R_d(A_{2d}^{n+1} - A_{2d}^n)}{2(A_2 - A_1)_e^{n+1}} \\
& \frac{+(R_f - R_aK_{2eb} - R_dK_{2ec})(A_{2e}^{n+1} - A_{2e}^n) - 2(AU)_{1e}^{n+1}}{2(A_2 - A_1)_e^{n+1}}
\end{aligned}
\tag{B.66}
$$

We notice that the parametres U, P and A of the two tubes are coupled.
Therefore, first we could calculate A_{2e} using the equation (B.65).
From the equation (B.59), we obtain P_{2e}. Immediately we obtain P_{2b} and P_{2c}.
From the equation (B.60) and (B.61), we obtain A_{2c} and A_{2b}.
From the equation (B.55), we obtain A_{1e}.
From the equation (B.56), we obtain U_{1e}.
From the equation (B.49), we obtain P_{1e}. Immediately we obtain P_{1b} and P_{1c}.
From the equation (B.50) and (B.51), we obtain A_{1c} and A_{1b}.
From the equation (B.53) and (B.54), we obtain U_{1c} and U_{1b}.
From the equation (B.66), we obtain U_{2e}.
From the equation (B.62) and (B.63), we obtain U_{2c} and U_{2b}.

B.1.2 Case 2

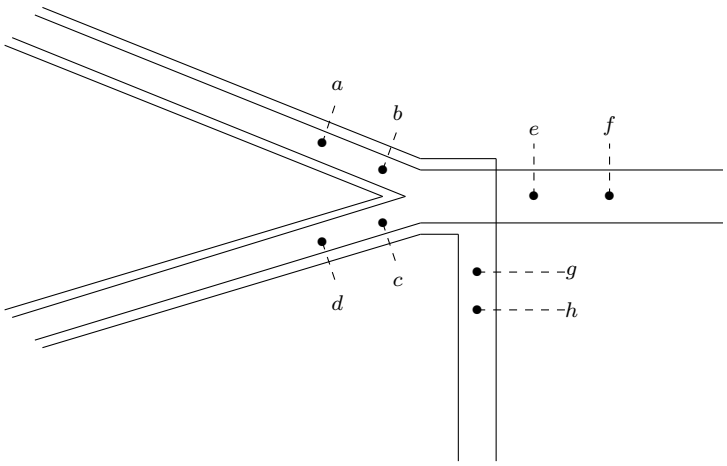

The jump conditions between the points b, c, e and g are :

$$(AU)_{1b} + (AU)_{1c} = (AU)_{1e} \tag{B.67}$$

$$P_{1b} = P_{1c} = P_{1e} \tag{B.68}$$

$$P_{1e} = El_{1e}\left(\frac{A_{1e}}{A_{01e}} - 1\right) \tag{B.69}$$

$$P_{1c} = El_{1c}\left(\frac{A_{1c}}{A_{01c}} - 1\right) + P_{2c} \tag{B.70}$$

$$P_{1b} = El_{1b}\left(\frac{A_{1b}}{A_{01b}} - 1\right) + P_{2b} \tag{B.71}$$

$$((A_2 - A_1)U_2)_b + ((A_2 - A_1)U_2)_c = (AU)_{2g} \tag{B.72}$$

$$P_{2b} = P_{2c} = P_{2g} \tag{B.73}$$

$$P_{2g} = El_{2g}\left(\frac{A_{2g}}{A_{02g}} - 1\right) \tag{B.74}$$

$$P_{2b} = El_{2b}\left(\frac{A_{2b}}{A_{02b}} - 1\right) \tag{B.75}$$

$$P_{2c} = El_{2c}\left(\frac{A_{2c}}{A_{02c}} - 1\right) \tag{B.76}$$

Giving that,

$$\frac{\Delta x_a}{2\Delta t_a}\left(A_{1a}^{n+1} - A_{1a}^{n} + A_{1b}^{n+1} - A_{1b}^{n}\right) + (AU)_{1b}^{n+1} - (AU)_{1a}^{n+1} = 0 \tag{B.77}$$

$$\frac{\Delta x_d}{2\Delta t_d}\left(A_{1d}^{n+1} - A_{1d}^{n} + A_{1c}^{n+1} - A_{1c}^{n}\right) + (AU)_{1c}^{n+1} - (AU)_{1d}^{n+1} = 0 \tag{B.78}$$

$$\frac{\Delta x_f}{2\Delta t_f}\left(A_{1f}^{n+1} - A_{1f}^{n} + A_{1e}^{n+1} - A_{1e}^{n}\right) + (AU)_{1f}^{n+1} - (AU)_{1e}^{n+1} = 0 \tag{B.79}$$

$$\frac{\Delta x_a}{2\Delta t_a}\left(A_{2b}^{n+1} - A_{2b}^{n} + A_{2a}^{n+1} - A_{2a}^{n}\right) + ((A_2 - A_1)U_2 + A_1U_1)_b^{n+1} - ((A_2 - A_1)U_2 + A_1U_1)_a^{n+1} = 0 \tag{B.80}$$

$$\frac{\Delta x_d}{2\Delta t_d}\left(A_{2d}^{n+1} - A_{2d}^{n} + A_{2c}^{n+1} - A_{2c}^{n}\right) + ((A_2 - A_1)U_2 + A_1U_1)_c^{n+1} - ((A_2 - A_1)U_2 + A_1U_1)_d^{n+1} = 0 \tag{B.81}$$

$$\frac{\Delta x_h}{2\Delta t_h}\left(A_{2h}^{n+1} - A_{2h}^{n} + A_{2g}^{n+1} - A_{2g}^{n}\right) + (AU)_{2h}^{n+1} - (AU)_{2g}^{n+1} = 0 \tag{B.82}$$

And,

$$A_{2b}^{n+1} - A_{2b}^{n} = \frac{El_{2g}}{El_{2b}}\frac{A_{02b}}{A_{02g}}(A_{2g}^{n+1} - A_{2g}^{n}) \tag{B.83}$$

$$A_{2c}^{n+1} - A_{2c}^{n} = \frac{El_{2g}}{El_{2c}} \frac{A_{02c}}{A_{02g}} (A_{2g}^{n+1} - A_{2g}^{n}) \tag{B.84}$$

$$A_{1c}^{n+1} - A_{1c}^{n} = \frac{El_{1e}}{El_{1c}} \frac{A_{01c}}{A_{01e}} (A_{1e}^{n+1} - A_{1e}^{n}) - \frac{El_{2g}}{El_{1c}} \frac{A_{01c}}{A_{02g}} (A_{2g}^{n+1} - A_{2g}^{n}) \tag{B.85}$$

$$A_{1b}^{n+1} - A_{1b}^{n} = \frac{El_{1e}}{El_{1b}} \frac{A_{01b}}{A_{01e}} (A_{1e}^{n+1} - A_{1e}^{n}) - \frac{El_{2g}}{El_{1b}} \frac{A_{01b}}{A_{02g}} (A_{2g}^{n+1} - A_{2g}^{n}) \tag{B.86}$$

By adding (B.77), (B.78) and (B.79) and using (B.85) and (B.86),

$$\begin{aligned}
&[R_f + R_a K_{1eb} + R_d K_{1ec}](A_{1e}^{n+1} - A_{1e}^{n}) - (R_a K_{2g1b} + R_d K_{2g1c})(A_{2g}^{n+1} - A_{2g}^{n}) \\
&= -R_a(A_{1a}^{n+1} - A_{1a}^{n}) - R_d(A_{1d}^{n+1} - A_{1d}^{n}) - R_f(A_{1f}^{n+1} - A_{1f}^{n}) + (AU)_{1a}^{n+1} \\
&+ (AU)_{1d}^{n+1} - (AU)_{1f}^{n+1}
\end{aligned} \tag{B.87}$$

Writing (B.79)-(B.77)-(B.78) gives,

$$\begin{aligned}
&[R_f - R_a K_{1eb} - R_d K_{1ec}](A_{1e}^{n+1} - A_{1e}^{n}) + (R_a K_{2g1b} + R_d K_{2g1c})(A_{2g}^{n+1} - A_{2g}^{n}) \\
&- R_a(A_{1a}^{n+1} - A_{1a}^{n}) - R_d(A_{1d}^{n+1} - A_{1d}^{n}) + R_f(A_{1f}^{n+1} - A_{1f}^{n}) + (AU)_{1a}^{n+1} \\
&+ (AU)_{1d}^{n+1} + (AU)_{1f}^{n+1} - 2\,(AU)_{1e}^{n+1}
\end{aligned} \tag{B.88}$$

Therefore,

$$\begin{aligned}
(AU)_{1e}^{n+1} =& \frac{1}{2}([R_f - R_a K_{1eb} - R_d K_{1ec}](A_{1e}^{n+1} - A_{1e}^{n}) \\
&+ (R_a K_{2g1b} + R_d K_{2g1c})(A_{2g}^{n+1} - A_{2g}^{n}) - R_a(A_{1a}^{n+1} - A_{1a}^{n}) \\
&- R_d(A_{1d}^{n+1} - A_{1d}^{n}) + R_f(A_{1f}^{n+1} - A_{1f}^{n}) + (AU)_{1a}^{n+1} \\
&+ (AU)_{1d}^{n+1} + (AU)_{1f}^{n+1})
\end{aligned} \tag{B.89}$$

Writing (B.80), (B.81) and (B.82) and using (B.83) and (B.84),

$$\begin{aligned}
&[R_h + R_a K_{2gb} + R_d K_{2gc}](A_{2g}^{n+1} - A_{2g}^{n}) + R_h(A_{2h}^{n+1} - A_{2h}^{n}) + R_a(A_{2a}^{n+1} - A_{2a}^{n}) \\
&+ R_d(A_{2d}^{n+1} - A_{2d}^{n}) + (AU)_{1e}^{n+1} - ((A_2 - A_1)U_2 + A_1 U_1)_{a}^{n+1} \\
&- ((A_2 - A_1)U_2 + A_1 U_1)_{d}^{n+1} + (AU)_{2h}^{n+1} = 0
\end{aligned} \tag{B.90}$$

By replacing (B.89) in (B.90),

$$
\begin{aligned}
&[\frac{R_f}{2} - \frac{R_a K_{1eb}}{2} - \frac{R_d K_{1ec}}{2}](A_{1e}^{n+1} - A_{1e}^{n}) \\
&+ (\frac{R_a K_{2g1b}}{2} + \frac{R_d K_{2g1c}}{2} + R_h + R_a K_{2gb} + R_d K_{2gc})(A_{2g}^{n+1} - A_{2g}^{n}) \\
&= \frac{R_a}{2}(A_{1a}^{n+1} - A_{1a}^{n}) + \frac{R_d}{2}(A_{1d}^{n+1} - A_{1d}^{n}) - \frac{R_f}{2}(A_{1f}^{n+1} - A_{1f}^{n}) \qquad \text{(B.91)} \\
&- \frac{(AU)_{1a}^{n+1}}{2} - \frac{(AU)_{1d}^{n+1}}{2} - \frac{(AU)_{1f}^{n+1}}{2} - R_h(A_{2h}^{n+1} - A_{2h}^{n}) - R_a(A_{2a}^{n+1} - A_{2a}^{n}) \\
&- R_d(A_{2d}^{n+1} - A_{2d}^{n}) + ((A_2 - A_1)U_2 + A_1U_1)_a^{n+1} + ((A_2 - A_1)U_2 + A_1U_1)_d^{n+1} \\
&- (AU)_{2h}^{n+1} \qquad \text{(B.92)}
\end{aligned}
$$

Using equations (B.87) and (B.92)

$$
\begin{pmatrix} A_{1e}^{n+1} - A_{1e}^{n} \\ A_{2g}^{n+1} - A_{2g}^{n} \end{pmatrix} = M^{-1} \begin{pmatrix} Z_1 \\ Z_2 \end{pmatrix} \qquad \text{(B.93)}
$$

with,

$$
M = \begin{pmatrix} R_f + R_a K_{1eb} + R_d K_{1ec} & -R_a K_{2g1b} - R_d K_{2g1c} \\ \frac{R_f}{2} - \frac{R_a K_{1eb}}{2} - \frac{R_d K_{1ec}}{2} & \frac{R_a K_{2g1b}}{2} + \frac{R_d K_{2g1c}}{2} + R_h + R_a K_{2gb} + R_d K_{2gc} \end{pmatrix}
$$

And,

$$
\begin{aligned}
Z_1 = &- R_a(A_{1a}^{n+1} - A_{1a}^{n}) - R_d(A_{1d}^{n+1} - A_{1d}^{n}) - R_f(A_{1f}^{n+1} - A_{1f}^{n}) + (AU)_{1a}^{n+1} \\
&+ (AU)_{1d}^{n+1} - (AU)_{1f}^{n+1}
\end{aligned}
$$

$$
\begin{aligned}
Z_2 = &\frac{R_a}{2}(A_{1a}^{n+1} - A_{1a}^{n}) + \frac{R_d}{2}(A_{1d}^{n+1} - A_{1d}^{n}) - \frac{R_f}{2}(A_{1f}^{n+1} - A_{1f}^{n}) \\
&- \frac{(AU)_{1a}^{n+1}}{2} - \frac{(AU)_{1d}^{n+1}}{2} - \frac{(AU)_{1f}^{n+1}}{2} - R_h(A_{2h}^{n+1} - A_{2h}^{n}) \\
&- R_a(A_{2a}^{n+1} - A_{2a}^{n}) - R_d(A_{2d}^{n+1} - A_{2d}^{n}) + ((A_2 - A_1)U_2 + A_1U_1)_a^{n+1} \\
&+ ((A_2 - A_1)U_2 + A_1U_1)_d^{n+1} - (AU)_{2h}^{n+1}
\end{aligned}
$$

(B.82)-(B.80)-(B.81)

$$
\begin{aligned}
&[R_h - R_a K_{2gb} - R_d K_{2gc}](A_{2g}^{n+1} - A_{2g}^{n}) - (AU)_{1e}^{n+1} + (AU)_{2h}^{n+1} \\
&+ ((A_2 - A_1)U_2 + A_1U_1)_a^{n+1} + ((A_2 - A_1)U_2 + A_1U_1)_d^{n+1} - 2\,(AU)_{2g}^{n+1} = 0
\end{aligned}
$$

Therefore,

$$U_{2g}^{n+1} = \frac{1}{2A_{2g}^{n+1}}([R_h - R_a K_{2gb} - R_d K_{2gc}](A_{2g}^{n+1} - A_{2g}^{n}) - (AU)_{1e}^{n+1} + (AU)_{2h}^{n+1}$$
$$+ ((A_2 - A_1)U_2 + A_1 U_1)_a^{n+1} + ((A_2 - A_1)U_2 + A_1 U_1)_d^{n+1}) \tag{B.94}$$

where

$$R_a = \left(\frac{\Delta x_a}{2\Delta t_a}\right), \qquad R_d = \left(\frac{\Delta x_d}{2\Delta t_d}\right), \qquad R_f = \left(\frac{\Delta x_f}{2\Delta t_f}\right)$$
$$R_h = \left(\frac{\Delta x_h}{2\Delta t_h}\right), \qquad K_{1eb} = \frac{El_{1b}}{El_{1e}}\frac{A_{01e}}{A_{01b}}, \qquad K_{1ec} = \frac{El_{1c}}{El_{1e}}\frac{A_{01e}}{A_{01c}}$$
$$K_{2gb} = \frac{El_{2g}}{El_{2b}}\frac{A_{02b}}{A_{02g}}, \qquad K_{2gc} = \frac{El_{2g}}{El_{2c}}\frac{A_{02c}}{A_{02g}}, \qquad K_{2g1b} = \frac{El_{2g}}{El_{1b}}\frac{A_{01b}}{A_{02g}}$$
$$K_{2g1c} = \frac{El_{2g}}{El_{1c}}\frac{A_{01c}}{A_{02g}}$$

From equation (B.93), we obtain A_{1e}^{n+1} and A_{2g}^{n+1}.
From equation (B.69) and (B.74) ,we obtain P_{1e}^{n+1} and P_{2g}^{n+1}. Immediately, we obtain P_{1b}^{n+1}, P_{1c}^{n+1}, P_{2b}^{n+1}, P_{2c}^{n+1}.
From equation (B.70), (B.71), (B.75) and (B.76) ,we obtain A_{1b}^{n+1}, A_{1c}^{n+1}, A_{2b}^{n+1}, A_{2c}^{n+1}.
From equation (B.89) or (B.79), we obtain U_{1e}^{n+1}.
From equation (B.77) and (B.78) we obtain U_{1b}^{n+1} and U_{1c}^{n+1}.
From equation (B.94) or (B.82), we obtain U_{2g}^{n+1}.
From equation (B.80) and (B.81) we obtain U_{2b}^{n+1} and U_{2c}^{n+1} .

B.1.3 Case 3

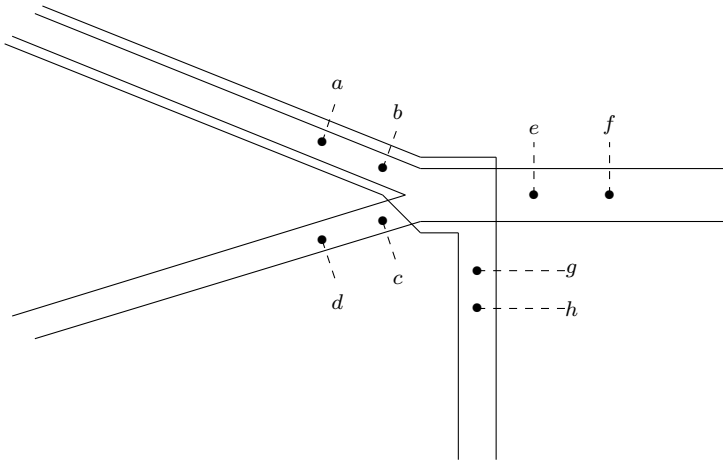

The jump conditions between the points b, c, e and g are :

$$(AU)_{1b} + (AU)_{1c} = (AU)_{1e} \tag{B.95}$$

$$P_{1b} = P_{1c} = P_{1e} \tag{B.96}$$

$$P_{1e} = El_{1e}\left(\frac{A_{1e}}{A_{01e}} - 1\right) \tag{B.97}$$

$$P_{1c} = El_{1c}\left(\frac{A_{1c}}{A_{01c}} - 1\right) \tag{B.98}$$

$$P_{1b} = El_{1b}\left(\frac{A_{1b}}{A_{01b}} - 1\right) + P_{2b} \tag{B.99}$$

$$((A_2 - A_1)U_2)_b = (AU)_{2g} \tag{B.100}$$

$$P_{2b} = P_{2g} \tag{B.101}$$

$$P_{2g} = El_{2g}\left(\frac{A_{2g}}{A_{02g}} - 1\right) \tag{B.102}$$

$$P_{2b} = El_{2b}\left(\frac{A_{2b}}{A_{02b}} - 1\right) \tag{B.103}$$

Given that,

$$\frac{\Delta x_a}{2\Delta t_a}\left(A_{1a}^{n+1} - A_{1a}^{n} + A_{1b}^{n+1} - A_{1b}^{n}\right) + (AU)_{1b}^{n+1} - (AU)_{1a}^{n+1} = 0 \tag{B.104}$$

$$\frac{\Delta x_d}{2\Delta t_d}\left(A_{1d}^{n+1} - A_{1d}^{n} + A_{1c}^{n+1} - A_{1c}^{n}\right) + (AU)_{1c}^{n+1} - (AU)_{1d}^{n+1} = 0 \tag{B.105}$$

$$\frac{\Delta x_f}{2\Delta t_f}\left(A_{1f}^{n+1} - A_{1f}^{n} + A_{1e}^{n+1} - A_{1e}^{n}\right) + (AU)_{1f}^{n+1} - (AU)_{1e}^{n+1} = 0 \tag{B.106}$$

$$\begin{aligned}&\frac{\Delta x_a}{2\Delta t_a}\left(A_{2b}^{n+1} - A_{2b}^{n} + A_{2a}^{n+1} - A_{2a}^{n}\right) + ((A_2 - A_1)U_2 + A_1U_1)_b^{n+1} \\ &- ((A_2 - A_1)U_2 + A_1U_1)_a^{n+1} = 0\end{aligned} \tag{B.107}$$

$$\frac{\Delta x_h}{2\Delta t_h}\left(A_{2h}^{n+1} - A_{2h}^{n} + A_{2g}^{n+1} - A_{2g}^{n}\right) + (AU)_{2h}^{n+1} - (AU)_{2g}^{n+1} = 0 \tag{B.108}$$

And,

$$A_{2b}^{n+1} - A_{2b}^{n} = \frac{El_{2g}}{El_{2b}}\frac{A_{02b}}{A_{02g}}(A_{2g}^{n+1} - A_{2g}^{n}) \tag{B.109}$$

$$A_{1c}^{n+1} - A_{1c}^{n} = \frac{El_{1e}}{El_{1c}}\frac{A_{01c}}{A_{01e}}(A_{1e}^{n+1} - A_{1e}^{n}) \tag{B.110}$$

$$A_{1b}^{n+1} - A_{1b}^{n} = \frac{El_{1e}}{El_{1b}} \frac{A_{01b}}{A_{01e}} (A_{1e}^{n+1} - A_{1e}^{n}) - \frac{El_{2g}}{El_{1b}} \frac{A_{01b}}{A_{02g}} (A_{2g}^{n+1} - A_{2g}^{n}) \tag{B.111}$$

Put,

$$R_a = \left(\frac{\Delta x_a}{2\Delta t_a}\right) \qquad R_d = \left(\frac{\Delta x_d}{2\Delta t_d}\right) \qquad R_f = \left(\frac{\Delta x_f}{2\Delta t_f}\right)$$
$$R_h = \left(\frac{\Delta x_h}{2\Delta t_h}\right) \qquad K_{1eb} = \frac{El_{1e}}{El_{1b}} \frac{A_{01b}}{A_{01e}} \qquad K_{1ec} = \frac{El_{1e}}{El_{1c}} \frac{A_{01c}}{A_{01e}}$$
$$K_{2gb} = \frac{El_{2g}}{El_{2b}} \frac{A_{02b}}{A_{02g}} \qquad K_{2g1b} = \frac{El_{2g}}{El_{1b}} \frac{A_{01b}}{A_{02g}}$$

By adding (B.104), (B.105) and (B.106) and using (B.110) and (B.111),

$$\begin{aligned}
&[R_f + R_a K_{1eb} + R_d K_{1ec}](A_{1e}^{n+1} - A_{1e}^{n}) - R_a K_{2g1b}(A_{2g}^{n+1} - A_{2g}^{n}) \\
&= -R_a(A_{1a}^{n+1} - A_{1a}^{n}) - R_d(A_{1d}^{n+1} - A_{1d}^{n}) - R_f(A_{1f}^{n+1} - A_{1f}^{n}) + (AU)_{1a}^{n+1} \\
&+ (AU)_{1d}^{n+1} - (AU)_{1f}^{n+1}
\end{aligned} \tag{B.112}$$

Writing (B.106)+(B.105)-(B.104) gives,

$$\begin{aligned}
&[R_f - R_a K_{1eb} + R_d K_{1ec}](A_{1e}^{n+1} - A_{1e}^{n}) + R_a K_{2g1b}(A_{2g}^{n+1} - A_{2g}^{n}) - R_a(A_{1a}^{n+1} - A_{1a}^{n}) \\
&+ R_d(A_{1d}^{n+1} - A_{1d}^{n}) + R_f(A_{1f}^{n+1} - A_{1f}^{n}) + (AU)_{1f}^{n+1} - (AU)_{1d}^{n+1} + (AU)_{1a}^{n+1} \\
&- 2\,(AU)_{1b}^{n+1} = 0
\end{aligned} \tag{B.113}$$

Therefore,

$$\begin{aligned}
(AU)_{1b}^{n+1} = &\frac{1}{2}([R_f - R_a K_{1eb} + R_d K_{1ec}](A_{1e}^{n+1} - A_{1e}^{n}) + R_a K_{2g1b}(A_{2g}^{n+1} - A_{2g}^{n}) \\
&- R_a(A_{1a}^{n+1} - A_{1a}^{n}) + R_d(A_{1d}^{n+1} - A_{1d}^{n}) + R_f(A_{1f}^{n+1} - A_{1f}^{n}) \\
&+ (AU)_{1f}^{n+1} - (AU)_{1d}^{n+1} + (AU)_{1a}^{n+1})
\end{aligned} \tag{B.114}$$

By adding (B.107) and (B.108) and using (B.109) and (B.84),

$$\begin{aligned}
&[R_h + R_a K_{2gb}](A_{2g}^{n+1} - A_{2g}^{n}) + R_h(A_{2h}^{n+1} - A_{2h}^{n}) + R_a(A_{2a}^{n+1} - A_{2a}^{n}) \\
&+ (AU)_{1b}^{n+1} - ((A_2 - A_1)U_2 + A_1 U_1)_a^{n+1} + (AU)_{2h}^{n+1} = 0
\end{aligned} \tag{B.115}$$

By replacing (B.114) in (B.115),

$$
\begin{aligned}
&[\frac{R_f}{2} - \frac{R_a K_{1eb}}{2} + \frac{R_d K_{1ec}}{2}](A_{1e}^{n+1} - A_{1e}^{n}) \\
&+ [\frac{R_a K_{2g1b}}{2} + R_h + R_a K_{2gb}](A_{2g}^{n+1} - A_{2g}^{n}) \\
&= \frac{(AU)_{1d}^{n+1}}{2} - \frac{(AU)_{1a}^{n+1}}{2} - \frac{(AU)_{1f}^{n+1}}{2} + \frac{R_a}{2}(A_{1a}^{n+1} - A_{1a}^{n}) - \frac{R_d}{2}(A_{1d}^{n+1} - A_{1d}^{n}) \\
&- \frac{R_f}{2}(A_{1f}^{n+1} - A_{1f}^{n}) - R_h(A_{2h}^{n+1} - A_{2h}^{n}) - R_a(A_{2a}^{n+1} - A_{2a}^{n}) \\
&+ ((A_2 - A_1)U_2 + A_1 U_1)_a^{n+1} - (AU)_{2h}^{n+1}
\end{aligned} \tag{B.116}
$$

Using equations (B.112) and (B.92)

$$
\begin{pmatrix} A_{1e}^{n+1} - A_{1e}^{n} \\ A_{2g}^{n+1} - A_{2g}^{n} \end{pmatrix} = M^{-1} \begin{pmatrix} Z_1 \\ Z_2 \end{pmatrix} \tag{B.117}
$$

with,

$$
M = \begin{pmatrix} R_f + R_a K_{1eb} + R_d K_{1ec} & -R_a K_{2g1b} \\ \frac{R_f}{2} - \frac{R_a K_{1eb}}{2} + \frac{R_d K_{1ec}}{2} & \frac{R_a K_{2g1b}}{2} + R_h + R_a K_{2gb} \end{pmatrix}
$$

And,

$$
\begin{aligned}
Z_1 = &- R_a(A_{1a}^{n+1} - A_{1a}^{n}) - R_d(A_{1d}^{n+1} - A_{1d}^{n}) - R_f(A_{1f}^{n+1} - A_{1f}^{n}) + (AU)_{1a}^{n+1} \\
&+ (AU)_{1d}^{n+1} - (AU)_{1f}^{n+1}
\end{aligned}
$$

$$
\begin{aligned}
Z_2 = &\frac{(AU)_{1d}^{n+1}}{2} - \frac{(AU)_{1a}^{n+1}}{2} - \frac{(AU)_{1f}^{n+1}}{2} + \frac{R_a}{2}(A_{1a}^{n+1} - A_{1a}^{n}) - \frac{R_d}{2}(A_{1d}^{n+1} - A_{1d}^{n}) \\
&- \frac{R_f}{2}(A_{1f}^{n+1} - A_{1f}^{n}) - R_h(A_{2h}^{n+1} - A_{2h}^{n}) - R_a(A_{2a}^{n+1} - A_{2a}^{n}) \\
&+ ((A_2 - A_1)U_2 + A_1 U_1)_a^{n+1} - (AU)_{2h}^{n+1}
\end{aligned}
$$

Writing (B.108)-(B.107) gives,

$$
\begin{aligned}
&[R_h - R_a K_{2gb}](A_{2g}^{n+1} - A_{2g}^{n}) + R_h(A_{2h}^{n+1} - A_{2h}^{n}) - R_a(A_{2a}^{n+1} - A_{2a}^{n}) \\
&+ (AU)_{2h}^{n+1} - 2(AU)_{2g}^{n+1} - (AU)_{1b}^{n+1} + ((A_2 - A_1)U_2 + A_1 U_1)_a^{n+1} = 0
\end{aligned} \tag{B.118}
$$

Therefore,

$$
\begin{aligned}
U_{2g}^{n+1} = &\frac{1}{2A_{2g}^{n+1}}([R_h - R_a K_{2gb}](A_{2g}^{n+1} - A_{2g}^{n}) + R_h(A_{2h}^{n+1} - A_{2h}^{n}) \\
&- R_a(A_{2a}^{n+1} - A_{2a}^{n}) + (AU)_{2h}^{n+1} - (AU)_{1b}^{n+1} \\
&+ ((A_2 - A_1)U_2 + A_1 U_1)_a^{n+1})
\end{aligned} \tag{B.119}
$$

From equation (B.117), we obtain A_{1e}^{n+1} and A_{2g}^{n+1}.
From equation (B.97) and (B.102) ,we obtain P_{1e}^{n+1} and P_{2g}^{n+1}. Immediately, we obtain P_{1b}^{n+1}, P_{1c}^{n+1} and P_{2b}^{n+1}.
From equation (B.98), (B.99) and (B.103), we obtain A_{1c}^{n+1}, A_{1b}^{n+1} and A_{2b}^{n+1}.
From equation (B.104) or (B.114), we obtain U_{1b}^{n+1}.
From equation (B.105) and (B.106) we obtain U_{1c}^{n+1} and U_{1e}^{n+1}.
From equation (B.119) or (B.108), we obtain U_{2g}^{n+1}.
From equation (B.100) or (B.107) we obtain U_{2b}^{n+1}.

B.2 A Bifurcation of tubes

B.2.1 Case 1

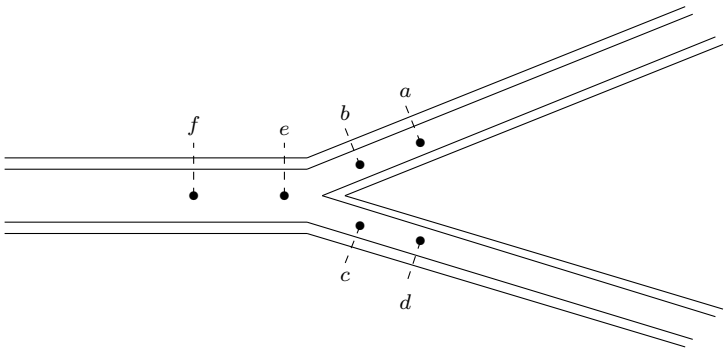

B.2.1.1 Interior tube

For the interior tube, the jump conditions between the points b, c and e are :

$$(AU)_{1b} + (AU)_{1c} = (AU)_{1e} \tag{B.120}$$

$$P_{1b} = P_{1c} = P_{1e} \tag{B.121}$$

$$P_{1e} = El_{1e}\left(\frac{A_{1e}}{A_{01e}} - 1\right) + P_{2e} \tag{B.122}$$

$$P_{1c} = El_{1c}\left(\frac{A_{1c}}{A_{01c}} - 1\right) + P_{2c} \tag{B.123}$$

$$P_{1b} = El_{1b}\left(\frac{A_{1b}}{A_{01b}} - 1\right) + P_{2b} \tag{B.124}$$

The conservation of mass equation was derived between a et b, d et c and e et f. We obtain :

$$\frac{\Delta x_f}{2\Delta t_f}\left(A_{1f}^{n+1} - A_{1f}^{n} + A_{1e}^{n+1} - A_{1e}^{n}\right) + (AU)_{1e}^{n+1} - (AU)_{1f}^{n+1} = 0 \tag{B.125}$$

$$\frac{\Delta x_a}{2\Delta t_a}\left(A_{1a}^{n+1}-A_{1a}^{n}+A_{1b}^{n+1}-A_{1b}^{n}\right)+(AU)_{1a}^{n+1}-(AU)_{1b}^{n+1}=0 \tag{B.126}$$

$$\frac{\Delta x_d}{2\Delta t_d}\left(A_{1d}^{n+1}-A_{1d}^{n}+A_{1c}^{n+1}-A_{1c}^{n}\right)+(AU)_{1d}^{n+1}-(AU)_{1c}^{n+1}=0 \tag{B.127}$$

Giving that,

$$A_{1b}^{n+1}-A_{1b}^{n}=\frac{El_{1e}}{El_{1b}}\frac{A_{01b}}{A_{01e}}(A_{1e}^{n+1}-A_{1e}^{n})$$
$$A_{1c}^{n+1}-A_{1c}^{n}=\frac{El_{1e}}{El_{1c}}\frac{A_{01c}}{A_{01e}}(A_{1e}^{n+1}-A_{1e}^{n})$$

Put,

$$R_a=\left(\frac{\Delta x_a}{2\Delta t_a}\right),\qquad R_d=\left(\frac{\Delta x_d}{2\Delta t_d}\right),\qquad R_f=\left(\frac{\Delta x_f}{2\Delta t_f}\right)$$
$$K_{1eb}=\frac{El_{1e}}{El_{1b}}\frac{A_{01b}}{A_{01e}},\qquad K_{1ec}=\frac{El_{1e}}{El_{1c}}\frac{A_{01c}}{A_{01e}}$$

Adding (B.125), (B.126) and (B.127) gives,

$$\begin{aligned}A_{1e}^{n+1}=&A_{1e}^{n}+\frac{(AU)_{1f}^{n+1}-(AU)_{1a}^{n+1}-(AU)_{1d}^{n+1}-R_a(A_{1a}^{n+1}-A_{1a}^{n})}{R_f+R_aK_{1eb}+R_dK_{1ec}}\\&\frac{-R_d(A_{1d}^{n+1}-A_{1d}^{n})-R_f(A_{1f}^{n+1}-A_{1f}^{n})}{R_f+R_aK_{1eb}+R_dK_{1ec}}\end{aligned} \tag{B.128}$$

Substracting (B.125) and (B.126) from (B.127) gives,

$$\begin{aligned}U_{1e}^{n+1}=&\frac{(AU)_{1a}^{n+1}+(AU)_{1d}^{n+1}+(AU)_{1f}^{n+1}+R_a(A_{1a}^{n+1}-A_{1a}^{n})+R_d(A_{1d}^{n+1}-A_{1d}^{n})}{2A_{1e}^{n+1}}\\&\frac{-R_f(A_{1f}^{n+1}-A_{1f}^{n})-(R_f-R_aK_{1eb}-R_dK_{1ec})(A_{1e}^{n+1}-A_{1e}^{n})}{2A_{1e}^{n+1}}\end{aligned} \tag{B.129}$$

B.2.1.2 Exterior tube

For the exterior tube, the jump conditions between the points b, c and e are :

$$((A_2-A_1)U_2)_b+((A_2-A_1)U_2)_c=((A_2-A_1)U_2)_e \tag{B.130}$$

$$P_{2b}=P_{2c}=P_{2e} \tag{B.131}$$

$$P_{2e}=El_{2e}\left(\frac{A_{2e}}{A_{02e}}-1\right) \tag{B.132}$$

$$P_{2b} = El_{2b}\left(\frac{A_{2b}}{A_{02b}} - 1\right) \tag{B.133}$$

$$P_{2c} = El_{2c}\left(\frac{A_{2c}}{A_{02c}} - 1\right) \tag{B.134}$$

The conservation of mass equation was derived between a et b, d et c and e et f. We obtain :

$$\begin{aligned}&\frac{\Delta x_a}{2\Delta t_a}\left(A_{2b}^{n+1} - A_{2b}^{n} + A_{2a}^{n+1} - A_{2a}^{n}\right) + ((A_2 - A_1)U_2 + A_1U_1)_a^{n+1} \\ &- ((A_2 - A_1)U_2 + A_1U_1)_b^{n+1} = 0\end{aligned} \tag{B.135}$$

$$\begin{aligned}&\frac{\Delta x_d}{2\Delta t_d}\left(A_{2d}^{n+1} - A_{2d}^{n} + A_{2c}^{n+1} - A_{2c}^{n}\right) + ((A_2 - A_1)U_2 + A_1U_1)_d^{n+1} \\ &- ((A_2 - A_1)U_2 + A_1U_1)_c^{n+1} = 0\end{aligned} \tag{B.136}$$

$$\begin{aligned}&\frac{\Delta x_f}{2\Delta t_f}\left(A_{2f}^{n+1} - A_{2f}^{n} + A_{2e}^{n+1} - A_{2e}^{n}\right) + ((A_2 - A_1)U_2 + A_1U_1)_e^{n+1} \\ &- ((A_2 - A_1)U_2 + A_1U_1)_f^{n+1} = 0\end{aligned} \tag{B.137}$$

Put,

$$\begin{aligned}\Delta A =& A_2 - A_1, & R_a =& \left(\frac{\Delta x_a}{2\Delta t_a}\right), & R_d =& \left(\frac{\Delta x_d}{2\Delta t_d}\right) \\ R_f =& \left(\frac{\Delta x_f}{2\Delta t_f}\right), & K_{2eb} =& \frac{El_{2e}}{El_{2b}}\frac{A_{02b}}{A_{02e}}, & K_{2ec} =& \frac{El_{2e}}{El_{2c}}\frac{A_{02c}}{A_{02e}}\end{aligned}$$

Adding (B.135), (B.136) and (B.137) gives, :

$$\begin{aligned}A_{2e}^{n+1} =& A_{2e}^{n} + \frac{(\Delta AU_2 + A_1U_1)_f^{n+1} - (\Delta AU_2 + A_1U_1)_a^{n+1}}{R_f + R_aK_{2eb} + R_dK_{2ec}} \\ &\frac{-(\Delta AU_2 + A_1U_1)_d^{n+1} - R_a(A_{2a}^{n+1} - A_{2a}^{n}) - R_d(A_{2d}^{n+1} - A_{2d}^{n})}{R_f + R_aK_{2eb} + R_dK_{2ec}} \\ &\frac{-R_f(A_{2f}^{n+1} - A_{2f}^{n})}{R_f + R_aK_{2eb} + R_dK_{2ec}}\end{aligned} \tag{B.138}$$

Substracting (B.135) and (B.136) from (B.137) gives,

$$\begin{aligned} U_{2e}^{n+1} = & \frac{(\Delta AU_2 + A_1U_1)_a^{n+1} + (\Delta AU_2 + A_1U_1)_d^{n+1} + (\Delta AU_2 + A_1U_1)_f^{n+1}}{2(A_2 - A_1)_e^{n+1}} \\ & \frac{-R_f(A_{2f}^{n+1} - A_{2f}^n) + R_a(A_{2a}^{n+1} - A_{2a}^n) + R_d(A_{2d}^{n+1} - A_{2d}^n)}{2(A_2 - A_1)_e^{n+1}} \\ & \frac{-(R_f - R_aK_{2eb} - R_dK_{2ec})(A_{2e}^{n+1} - A_{2e}^n) - 2(AU)_{1e}^{n+1}}{2(A_2 - A_1)_e^{n+1}} \end{aligned} \tag{B.139}$$

We notice that the parametres U, P and A of the two tubes are coupled.
Therefore, first we could calculate A_{2e} using the equation (B.138).
From the equation (B.132), we obtain P_{2e}. Immediately we obtain P_{2b} and P_{2c}.
From the equation (B.133) and (B.134), we obtain A_{2c} and A_{2b}.
From the equation (B.128), we obtain A_{1e}.
From the equation (B.129), we obtain U_{1e}.
From the equation (B.122), we obtain P_{1e}. Immediately we obtain P_{1b} and P_{1c}.
From the equation (B.123) and (B.124), we obtain A_{1c} and A_{1b}.
From the equation (B.126) and (B.127), we obtain U_{1c} and U_{1b}.
From the equation (B.139), we obtain U_{2e}.
From the equation (B.135) and (B.136), we obtain U_{2c} and U_{2b}.

B.2.2 Case 2

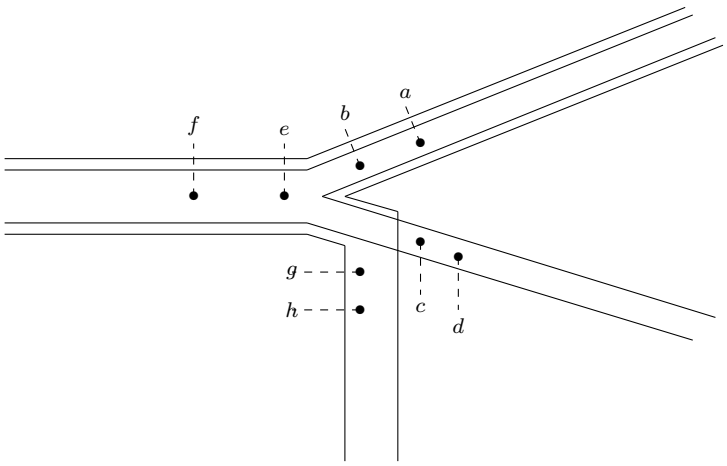

The jump conditions between the points b, c, e and g are :

$$(AU)_{1b} + (AU)_{1c} = (AU)_{1e} \tag{B.140}$$

$$P_{1b} = P_{1c} = P_{1e} \tag{B.141}$$

$$P_{1e} = El_{1e}\left(\frac{A_{1e}}{A_{01e}} - 1\right) + P_{2e} \tag{B.142}$$

$$P_{1c} = El_{1c}\left(\frac{A_{1c}}{A_{01c}} - 1\right) \tag{B.143}$$

$$P_{1b} = El_{1b}\left(\frac{A_{1b}}{A_{01b}} - 1\right) + P_{2b} \tag{B.144}$$

$$((A_2 - A_1)U_2)_b + (AU)_{2g} = ((A_2 - A_1)U_2)_e \tag{B.145}$$

$$P_{2b} = P_{2e} = P_{2g} \tag{B.146}$$

$$P_{2g} = El_{2g}\left(\frac{A_{2g}}{A_{02g}} - 1\right) \tag{B.147}$$

$$P_{2b} = El_{2b}\left(\frac{A_{2b}}{A_{02b}} - 1\right) \tag{B.148}$$

$$P_{2e} = El_{2e}\left(\frac{A_{2e}}{A_{02e}} - 1\right) \tag{B.149}$$

Giving that,

$$\frac{\Delta x_a}{2\Delta t_a}\left(A_{1a}^{n+1} - A_{1a}^{n} + A_{1b}^{n+1} - A_{1b}^{n}\right) + (AU)_{1a}^{n+1} - (AU)_{1b}^{n+1} = 0 \tag{B.150}$$

$$\frac{\Delta x_d}{2\Delta t_d}\left(A_{1d}^{n+1} - A_{1d}^{n} + A_{1c}^{n+1} - A_{1c}^{n}\right) + (AU)_{1d}^{n+1} - (AU)_{1c}^{n+1} = 0 \tag{B.151}$$

$$\frac{\Delta x_f}{2\Delta t_f}\left(A_{1f}^{n+1} - A_{1f}^{n} + A_{1e}^{n+1} - A_{1e}^{n}\right) + (AU)_{1e}^{n+1} - (AU)_{1f}^{n+1} = 0 \tag{B.152}$$

$$\frac{\Delta x_a}{2\Delta t_a}\left(A_{2b}^{n+1} - A_{2b}^{n} + A_{2a}^{n+1} - A_{2a}^{n}\right) + ((A_2 - A_1)U_2 + A_1U_1)_a^{n+1} - ((A_2 - A_1)U_2 + A_1U_1)_b^{n+1} = 0 \tag{B.153}$$

$$\frac{\Delta x_f}{2\Delta t_f}\left(A_{2e}^{n+1} - A_{2e}^{n} + A_{2f}^{n+1} - A_{2f}^{n}\right) + ((A_2 - A_1)U_2 + A_1U_1)_e^{n+1} - ((A_2 - A_1)U_2 + A_1U_1)_f^{n+1} = 0 \tag{B.154}$$

$$\frac{\Delta x_h}{2\Delta t_h}\left(A_{2h}^{n+1} - A_{2h}^{n} + A_{2g}^{n+1} - A_{2g}^{n}\right) + (AU)_{2h}^{n+1} - (AU)_{2g}^{n+1} = 0 \tag{B.155}$$

And,

$$A_{2b}^{n+1} - A_{2b}^{n} = \frac{El_{2g}}{El_{2b}}\frac{A_{02b}}{A_{02g}}(A_{2g}^{n+1} - A_{2g}^{n}) \tag{B.156}$$

$$A_{2e}^{n+1} - A_{2e}^{n} = \frac{El_{2g}}{El_{2e}} \frac{A_{02e}}{A_{02g}} (A_{2g}^{n+1} - A_{2g}^{n}) \tag{B.157}$$

$$A_{1c}^{n+1} - A_{1c}^{n} = \frac{El_{1e}}{El_{1c}} \frac{A_{01c}}{A_{01e}} (A_{1e}^{n+1} - A_{1e}^{n}) + \frac{El_{2g}}{El_{1c}} \frac{A_{01c}}{A_{02g}} (A_{2g}^{n+1} - A_{2g}^{n}) \tag{B.158}$$

$$A_{1b}^{n+1} - A_{1b}^{n} = \frac{El_{1e}}{El_{1b}} \frac{A_{01b}}{A_{01e}} (A_{1e}^{n+1} - A_{1e}^{n}) \tag{B.159}$$

By adding (B.150), (B.151) and (B.152) and using (B.140), (B.158) and (B.159),

$$\begin{aligned}
&[R_f + R_a K_{1eb} + R_d K_{1ec}](A_{1e}^{n+1} - A_{1e}^{n}) + R_d K_{2g1c}(A_{2g}^{n+1} - A_{2g}^{n}) \\
&= -R_a(A_{1a}^{n+1} - A_{1a}^{n}) - R_d(A_{1d}^{n+1} - A_{1d}^{n}) - R_f(A_{1f}^{n+1} - A_{1f}^{n}) - (AU)_{1a}^{n+1} \\
&- (AU)_{1d}^{n+1} + (AU)_{1f}^{n+1}
\end{aligned} \tag{B.160}$$

Writing (B.150)+(B.152)-(B.151) gives,

$$\begin{aligned}
&[R_f + R_a K_{1eb} - R_d K_{1ec}](A_{1e}^{n+1} - A_{1e}^{n}) - R_d K_{2g1c}(A_{2g}^{n+1} - A_{2g}^{n}) \\
&+ R_a(A_{1a}^{n+1} - A_{1a}^{n}) - R_d(A_{1d}^{n+1} - A_{1d}^{n}) + R_f(A_{1f}^{n+1} - A_{1f}^{n}) + (AU)_{1a}^{n+1} \\
&- (AU)_{1d}^{n+1} - (AU)_{1f}^{n+1} + 2\,(AU)_{1c}^{n+1}
\end{aligned} \tag{B.161}$$

Therefore,

$$\begin{aligned}
(AU)_{1c}^{n+1} =& \frac{1}{2}(-[R_f + R_a K_{1eb} - R_d K_{1ec}](A_{1e}^{n+1} - A_{1e}^{n}) + R_d K_{2g1c}(A_{2g}^{n+1} - A_{2g}^{n}) \\
&- R_a(A_{1a}^{n+1} - A_{1a}^{n}) + R_d(A_{1d}^{n+1} - A_{1d}^{n}) - R_f(A_{1f}^{n+1} - A_{1f}^{n}) \\
&- (AU)_{1a}^{n+1} + (AU)_{1d}^{n+1} + (AU)_{1f}^{n+1})
\end{aligned} \tag{B.162}$$

By adding (B.153), (B.154) and (B.155) and using (B.156), (B.157), (B.140) and (B.145),

$$\begin{aligned}
&[R_h + R_a K_{2gb} + R_f K_{2ge}](A_{2g}^{n+1} - A_{2g}^{n}) + R_a(A_{2a}^{n+1} - A_{2a}^{n}) + R_f(A_{2f}^{n+1} - A_{2f}^{n}) \\
&+ R_h(A_{2h}^{n+1} - A_{2h}^{n}) + ((A_2 - A_1)U_2 + A_1 U_1)_a^{n+1} - ((A_2 - A_1)U_2 + A_1 U_1)_f^{n+1} \\
&+ (AU)_{2h}^{n+1} + (AU)_{1c}^{n+1} = 0
\end{aligned} \tag{B.163}$$

By replacing (B.162) in (B.163)

$$
\begin{aligned}
&(-\frac{R_f}{2} - \frac{R_a K_{1eb}}{2} + \frac{R_d K_{1ec}}{2}](A_{1e}^{n+1} - A_{1e}^{n}) \\
&+ [\frac{R_d K_{21gc}}{2} + R_h + R_a K_{2gb} + R_f K_{2ge}](A_{2g}^{n+1} - A_{2g}^{n}) = \\
&\frac{R_a}{2}(A_{1a}^{n+1} - A_{1a}^{n}) - \frac{R_d}{2}(A_{1d}^{n+1} - A_{1d}^{n}) + \frac{R_f}{2}(A_{1f}^{n+1} - A_{1f}^{n}) + \frac{(AU)_{1a}^{n+1}}{2} \\
&- \frac{(AU)_{1d}^{n+1}}{2} - \frac{(AU)_{1f}^{n+1}}{2} - R_a(A_{2a}^{n+1} - A_{2a}^{n}) - R_f(A_{2f}^{n+1} - A_{2f}^{n}) \\
&- R_h(A_{2h}^{n+1} - A_{2h}^{n}) - ((A_2 - A_1)U_2 + A_1 U_1)_a^{n+1} + ((A_2 - A_1)U_2 + A_1 U_1)_f^{n+1} \\
&- (AU)_{2h}^{n+1}
\end{aligned}
\tag{B.164}
$$

Using equations (B.160) and (B.164)

$$
\begin{pmatrix} A_{1e}^{n+1} - A_{1e}^{n} \\ A_{2g}^{n+1} - A_{2g}^{n} \end{pmatrix} = M^{-1} \begin{pmatrix} Z_1 \\ Z_2 \end{pmatrix} \tag{B.165}
$$

with,

$$
M = \begin{pmatrix} R_f + R_a K_{1eb} + R_d K_{1ec} & R_d K_{2g1c} \\ -\frac{R_f}{2} - \frac{R_a K_{1eb}}{2} + \frac{R_d K_{1ec}}{2} & \frac{R_d K_{2g1c}}{2} + R_h + R_a K_{2gb} + R_f K_{2ge} \end{pmatrix}
$$

And,

$$
\begin{aligned}
Z_1 = &- R_a(A_{1a}^{n+1} - A_{1a}^{n}) - R_d(A_{1d}^{n+1} - A_{1d}^{n}) - R_f(A_{1f}^{n+1} - A_{1f}^{n}) - (AU)_{1a}^{n+1} \\
&- (AU)_{1d}^{n+1} + (AU)_{1f}^{n+1}
\end{aligned}
$$

$$
\begin{aligned}
Z_2 = &\frac{R_a}{2}(A_{1a}^{n+1} - A_{1a}^{n}) - \frac{R_d}{2}(A_{1d}^{n+1} - A_{1d}^{n}) + \frac{R_f}{2}(A_{1f}^{n+1} - A_{1f}^{n}) + \frac{(AU)_{1a}^{n+1}}{2} \\
&- \frac{(AU)_{1d}^{n+1}}{2} - \frac{(AU)_{1f}^{n+1}}{2} - R_a(A_{2a}^{n+1} - A_{2a}^{n}) - R_f(A_{2f}^{n+1} - A_{2f}^{n}) \\
&- R_h(A_{2h}^{n+1} - A_{2h}^{n}) - ((A_2 - A_1)U_2 + A_1 U_1)_a^{n+1} \\
&+ ((A_2 - A_1)U_2 + A_1 U_1)_f^{n+1} - (AU)_{2h}^{n+1}
\end{aligned}
$$

Writing (B.154)+(B.153)-(B.155) gives,

$$
\begin{aligned}
&[-R_h + R_a K_{2gb} + R_f K_{2ge}](A_{2g}^{n+1} - A_{2g}^{n}) + R_a(A_{2a}^{n+1} - A_{2a}^{n}) \\
&+ R_f(A_{2f}^{n+1} - A_{2f}^{n}) - R_h(A_{2h}^{n+1} - A_{2h}^{n}) + ((A_2 - A_1)U_2 + A_1 U_1)_a^{n+1} \\
&- ((A_2 - A_1)U_2 + A_1 U_1)_f^{n+1} - (AU)_{2h}^{n+1} + 2(AU)_{2g}^{n+1} + (AU)_{1c}^{n+1} \\
&= 0
\end{aligned}
$$

Therefore,

$$\begin{aligned} U_{2g}^{n+1} =& \frac{1}{2A_{2g}^{n+1}}([R_h - R_a K_{2gb} - R_f K_{2ge}](A_{2g}^{n+1} - A_{2g}^{n}) - R_a(A_{2a}^{n+1} - A_{2a}^{n}) \\ & - R_f(A_{2f}^{n+1} - A_{2f}^{n}) + R_h(A_{2h}^{n+1} - A_{2h}^{n}) - ((A_2 - A_1)U_2 + A_1U_1)_a^{n+1} \\ & + ((A_2 - A_1)U_2 + A_1U_1)_f^{n+1} + (AU)_{2h}^{n+1} - (AU)_{1c}^{n+1}) \end{aligned} \tag{B.166}$$

From equation (B.165), we obtain A_{1e}^{n+1} and A_{2g}^{n+1}.
From equation (B.142) and (B.147) ,we obtain P_{1e}^{n+1} and P_{2g}^{n+1}. Immediately, we obtain P_{1b}^{n+1}, P_{1c}^{n+1}, P_{2b}^{n+1}, P_{2e}^{n+1}.
From equation (B.143), (B.144), (B.148) and (B.149), we obtain A_{1c}^{n+1}, A_{1b}^{n+1}, A_{2b}^{n+1} and A_{2e}^{n+1}.
From equation (B.162) or (B.151), we obtain U_{1c}^{n+1}.
From equation (B.150) and (B.152) we obtain U_{1b}^{n+1} and U_{1e}^{n+1}.
From equation (B.166) or (B.155), we obtain U_{2g}^{n+1}.
From equation (B.153) and (B.154) we obtain U_{2b}^{n+1} and U_{2e}^{n+1}.

Appendix C

A one dimensional model of the Cerebrospinal Fluid Flow in the spinal canal: study of the fluid viscosity and the steady/unsteady flow effects

---

The following article has been submited to the Physics of Fluids journal and is currently undergoing reviews.

A one dimensional model of the Cerebrospinal Fluid Flow in the spinal canal: study of the fluid viscosity and the steady/unsteady flow effects

Maher M., Cathalifaud P., Zagzoule M.

Institut de Mécanique des Fluides de Toulouse (IMFT), Université de Toulouse, CNRS, INPT, UPS, Toulouse, France

Abstract

In this study, a one dimensional-model (1-D) for the flow in elastic pipes is used to simulate the dynamics of the Cerebrospinal Fluid (CSF) in the spinal canal. The modelling is based around two coaxial tubes filled with CSF. The inner tube represents the Spinal Cord (SC) and the outer one represents the Spinal Subarachnoid Space (SSS). The conservation of mass and momentum in 1D is applied to the two coupled tubes. The modelling accounts for the viscosity of the CSF. Specific attention is given to the effect of the CSF viscosity on the wave propagtion modes. Moreover, this work confronts the wall shear stress of a quasi-steady flow approximation used in 1-D modelling against the wall shear stress for an unsteady flow in an annuli.

Keywords: Spinal canal, coaxial tubes, 1D model, Cerebropsinal Fluid, conicity, viscosity

1. Introduction

The Cerebrospinal fluid (CSF) is a fluid close to water which is mainly contained in cavities in the brain called ventricles and anatomic spaces called cranial and spinal subarachnoid spaces (SSS). The SSS is an annular space surrounding the spinal cord (SC). Three protective membranes, called the meninges lies within

the spinal cord. The pia-matter adheres to the surface of the spinal cord. The dura-matter and the arachnoid-matter envelop the SSS.

The CSF circulation depends on the arterial pulse wave and displays a pulsating motion between the cranial and the spinal compartment. Additional factors such as the respiratory waves and the subject's posture also modulates the CSF dynamics (Haughton and Mardal, 2014; Sakka et al., 2011).

CSF velocity wave in the spinal canal is of interest as a potential indicator of CSF system pressure and compliance. It is considered an important factor influencing the pathogenesis of craniospinal disorder such as hydrocephalus, chiari malformation and syringomyelia (Luciano and Dombrowski, 2007; Flanagan, 2015). Several analytical (Lockey et al., 1975; Cirovic, 2009; Cirovic and Kim, 2012; Elliott et al., 2017; Berkouk et al., 2003; Carpenter et al., 2003) and computational studies (Bertram, 2009; Bertram et al., 2005) have used the idealised geometry of coaxial and compliant tubes to understand the dynamics of the CSF in the spinal canal. Based on MRI flow measurements in a healthy volunteer, Loth et al. (2001) computed a linearized Navier-Stokes model of the CSF flow in the spinal subarachnoid space (SSS). It has been observed that the Womersley number ranged from 5 to 17. It relates flow pulsatility (unsteady or inertial forces) to fluid viscosity (viscous forces), and is used to characterize flow dynamics. For normal physiological flow rates and CSF fluid properties, results have shown that for large annular gaps, inertial effects tend to dominate the flow field and for small annular gaps, viscous effect dominate the flow. Reduction of the SSS radius occur in CSF related disorders. For example in Chiari malformations where the cerebellar tonsils herniates into the cervical spinal canal or in syringomyelia where spinal cord swells. This reduction will change the hydrodynamic system from interia dominated to mixed (inertia+viscous) an in extreme cases, to a viscous dominated flow. Since then in posterior studies, to the best of our knowledge, the CSF viscosity is usually being neglected in 1-D modelling of the flow in the spinal canal. In this study, we developp a one-dimensionnal (1-D) modelling of the spinal canal as coaxial and compliant tubes with particular attention to the viscosity of the CSF in the SSS.

Furthermore, when accounting for the CSF viscosity, in order to solve the 1-D governing equation, one must make an assumption on the local velocity profile or the unsteady nature of the flow for a proper estimation of the wall shear stresses in both circular and annular section. The Womersley number gives a strong indication on the profile. In general, for $W_o < 1$, in a circular tube the fluid velocity profile is parabolic and the flow rate is in phase with the pressure gradient. The fluid profile loses its parabolic shape when $Wo > 1$, and a phase lag between pressure and flow rate becomes more pronounced as the Womersley number reaches ten or more (Womersley, 1955).

The present work first presents the 1-D geometry and governing equations for a viscous CSF. The wall shear stresses in the coaxial geometry are evaluated on the assumption of a quasi-steady flow state. Next, wave propagation modes are characterized. An analytical solution of the wave equation is proposed for an inviscid CSF flow and for a viscous one. Finally, using the work of Tsangaris (1984), an analytical solution of the wall shear stresses in annular section of a viscous flow due ton an oscillating pressure is presented. The limitations of the quasi-steady flow assumption in an annular section is discussed. Accordingly, the theoretical study of an unsteady flow in a circular annuli can be viewed as fundamental and independent of the particular application to the spinal CSF system.

2. Geometry and approximations

The idealized geometry around which the theory is based is illustrated in Figure 1. It consists of two coaxial and elastic tubes. The inner tube represents the SC which is envelopped by the pia-matter. The outer tube represents the SSS and is filled with CSF. The dura-matter envelops the SSS.

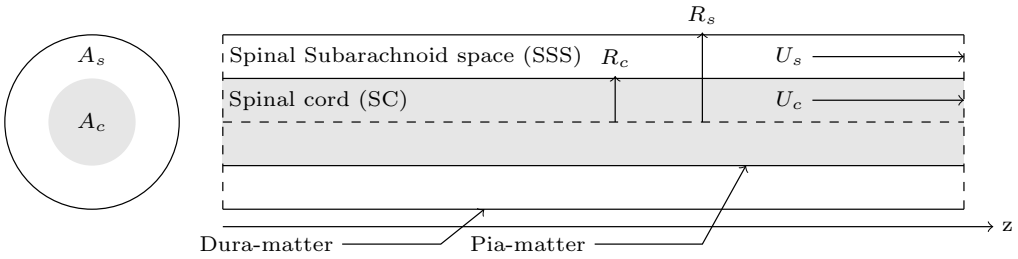

Figure 1: Idealised geometry of the spinal canal. The inner and elastic tube represents the spinal cord and is envelopped by the pia-matter. The outter and elastic tube represents the spinal subarachnoid space and is envelopped by the dura-matter.

In this work, for simplification reason, we have chosen to consider to cosnider the SC a thin walled tube filled with CSF. Actually, the SC consists of nervous tissues.

We consider the CSF as a viscous ($\mu_{csf} = 10^{-3}$ Pa.s^{-1}), incompressible and newtonian fluid. We make the hypothesis that the wave length is long compared to the tubes radius and that the flow is axisymmetric. Therefore, by integrating the fluid mass and momemtum conservation equations over the cross-sections of the SC and the SSS, we obtain the 1-D flow model for the spinal CSF flow.

3. Governing equations

The governing equations consists of two coupled 1-D system for the SC and for the SSS. Suffices c and s denotes respectively for the SC and the SSS. For the SC, we have

$$\begin{cases} \dfrac{\partial A_c}{\partial t} + \dfrac{\partial (U_c A_c)}{\partial z} = 0 \\ \dfrac{\partial U_c}{\partial t} + U_c \dfrac{\partial U_c}{\partial z} + \dfrac{1}{\rho}\dfrac{\partial P_c}{\partial z} = \dfrac{2\sqrt{\pi}}{\rho\sqrt{A_c}}\tau_c \end{cases} \tag{1}$$

For the SSS, we have

$$\begin{cases} \dfrac{\partial A_s}{\partial t} + \dfrac{\partial U_s(A_s - A_c)}{\partial z} + \dfrac{\partial (U_c A_c)}{\partial z} = 0 \\ \dfrac{\partial U_s}{\partial t} + U_s \dfrac{\partial U_s}{\partial z} + \dfrac{1}{\rho}\dfrac{\partial P_s}{\partial z} = -\dfrac{2\sqrt{\pi}}{\rho(A_s - A_c)}(\sqrt{A_s}\tau_{cs} - \sqrt{A_c}\tau_{sd}) \end{cases} \tag{2}$$

where z and t are respectively axial coordinate and time, A is the cross-sectional area, U and P are the axial velocity and pressure of the CSF respectively averaged over the cross sectional area, τ_c is the wall shear stress at $(r = R_c)$ due to the friction between the CSF in the SC and the pia-matter, τ_{cs} is the wall shear stress at $(r = R_c)$ due to the friction between the CSF in the SSS and the pia-matter and τ_{sd} the wall shear stress at $(r = R_s)$ due to the friction between the CSF in the SSS and the dura-matter.

The wall shear stresses τ_c, τ_{cs} and τ_{sd} are expressed as

$$\begin{cases} \tau_c = \mu \left(\dfrac{\partial u_c}{\partial r} \right)_{r=R_c} \\ \tau_{cs} = \mu \left(\dfrac{\partial u_s}{\partial r} \right)_{r=R_c} \\ \tau_{sd} = \mu \left(\dfrac{\partial u_s}{\partial r} \right)_{r=R_s} \end{cases}$$

At this point to solve the system of the coupled equations, we need to make an assumption on the local velocity profile in order to obtain an estimation of the above wall shear stresses. For a simplification matter, we assume a quasi-steady flow approximation. "Quasi steady" does not mean "approximately steady" (i.e, not changing very much in time). Rather "Quasi steady" means that at any time the instantaneous fow rate is determined by the instantaneous pressure gradient. In the last section of this paper, we will discuss the validity of this hypothesis in the SSS.

For the SC, this assumption leads to the commonly known Hagen-Poiseuille flow whose velocity profile is

$$u_c = 2U_c \left(1 - \left(\frac{r}{R_{c0}} \right)^2 \right)$$

According to (3), the wall shear stress, τ_c, is thus given by

$$\tau_c = -4\mu \frac{U_c}{R_{c0}}$$

For the SSS, giving the pressure gradient for a laminar steady flow in a straight rigid tube

$$\frac{\partial p_s}{\partial z} = \mu \frac{1}{r} \frac{\partial}{\partial r} \left(r \frac{\partial u_s}{\partial r} \right)$$

And using the no-slip boundary conditions at $(r = R_c)$ and $(r = R_s)$

$$\begin{cases} u_{s(r=R_c)} = 0 \\ u_{s(r=R_s)} = 0 \end{cases}$$

We obtain the axial velocity u_s

$$u_s = \frac{1}{4\mu} R_{s0}^2 \frac{\partial p_s}{\partial z} \left(\left(\frac{r}{R_{s0}} \right)^2 - 1 + \frac{1-\lambda^2}{\ln \lambda} \ln \left(\frac{r}{R_{s0}} \right) \right) \tag{3}$$

where $\lambda = \dfrac{R_{c0}}{R_{s0}}$.

Introducing the averaged axial velocity

$$U_s = \frac{1}{\pi(R_{s0}^2 - R_{c0}^2)} \int_{R_{c0}}^{R_{s0}} u_s 2\pi r \mathrm{d}r = -\frac{1}{8\mu} R_{s0}^2 \frac{\partial p_s}{\partial z} \left(1 + \lambda^2 + \frac{1-\lambda^2}{\ln \lambda} \right)$$

We obtain the expression of the axial velocity u_s in an annuli as a function of the averaged axial velocity U_s

$$u_s = 2U_s \left(\frac{1 - \left(\frac{r}{R_{s0}} \right)^2 - \frac{1-\lambda^2}{\ln \lambda} \ln \left(\frac{r}{R_{s0}} \right)}{1 + \lambda^2 + \frac{1-\lambda^2}{\ln \lambda}} \right) \tag{4}$$

After derivating the expression of u_s, we obtain

$$\tau_{cs} = \frac{2\mu U_s}{\gamma} \left(\frac{2R_{c0}}{R_{s0}^2} + \frac{1-\lambda^2}{R_{c0} \ln \lambda} \right)$$

$$\tau_{sd} = \frac{2\mu U_s}{\gamma} \left(\frac{2}{R_{s0}} + \frac{1-\lambda^2}{R_{s0} \ln \lambda} \right)$$

where $\gamma = 1 + \lambda^2 + \dfrac{1-\lambda^2}{\ln \lambda}$.

Strictly speaking, the above wall shear stresses hold for a steady flow in a rigid tube, but they are considered acceptable for a quasi-steady flow and for small perturbations.

Finally, to close the system of the governing equations (1) and (2), we introduce a relation between the pressure and the cross-section area which is commonly called a tube law. In our model, the transmural pressure is related to the cross section area through the following elastic linear tube law

$$\Delta P = E_l \left(\frac{A}{A_0} - 1 \right) \tag{5}$$

where ΔP is the transmural pressure, E_l is the elastance of the tube and denotes its mechanical properties, A_0 is the cross-section area at zero transmural pressure. Using this tube law for the SC and SSS tubes and assuming a constant pressure surrounding the dura-matter, we obtain

$$\begin{cases} \Delta P = P_c - P_s = E_{lc}\left(\dfrac{A_c}{A_{0c}} - 1\right) \\ P_s = E_{ls}\left(\dfrac{A_s}{A_{0s}} - 1\right) \end{cases} \tag{6}$$

where E_{lc} is the elastance of the pia-matter and E_{ls} is the elastance of the dura-matter. E_{lc} and E_{ls} are assumed constant.

The solution of the coupled system (1), (2) and (6) is numerically solved using the two step Lax Wendroff Scheme. One-dimensional grid with 1001 nodes and a time step increment of 2.10^{-5} is used. The convergence criteria was 10^{-6} of the residual imbalance of the mass conservation.

4. Waves equations

When free from any constraint, the speeds of the Young's mode in the pia-matter, c_c, and in the dura-matter, c_s, are as follow

$$c_c = \sqrt{\frac{A_c}{\rho}\frac{\mathrm{d}(P_c - P_s)}{\mathrm{d}A_c}} \tag{7}$$

$$c_s = \sqrt{\frac{A_s}{\rho}\frac{\mathrm{d}P_s}{\mathrm{d}A_s}} \tag{8}$$

When the pia-matter and dura-matter are coupled, the speeds of the two waves modes observed are (Cirovic, 2009)

$$c_{1,2}^2 = \frac{1}{2}(c_s^2 + c_c^2) \pm \sqrt{\left(\frac{1}{2}(c_s^2 + c_c^2)\right)^2 - \alpha_{cs} c_s^2 c_c^2} \tag{9}$$

where $\alpha_{cs} = 1 - \dfrac{A_c}{A_s}$.

The speeds of these two waves corresponds to the eigenvalues of the system formed by equations (1) and (2).

4.1. Inviscid CSF

For this case, the momentum equations of the SC (1) and the SSS (2) could be written respectively in the following form, omitting the friction term on the right-hand side of the equations

$$\frac{\partial Q_c}{\partial t} + \frac{A_c}{\rho}\frac{\partial P_c}{\partial z} = 0 \tag{10}$$

$$\frac{\partial Q_s}{\partial t} + \frac{(A_s - A_c)}{\rho}\frac{\partial P_s}{\partial z} = 0 \tag{11}$$

where Q_c and Q_s are respectively the averaged CSF flow in the SC and the SSS. Following the transmural pressure (6)

$$\frac{\partial \Delta P}{\partial z} = \frac{\partial P_c}{\partial z} - \frac{\partial P_s}{\partial z}$$

And using the momentum equations (10) and (11), we obtain

$$\frac{\partial^2 \Delta P}{\partial z^2} = -\frac{\rho}{A_c}\frac{\partial^2 Q_c}{\partial z \partial t} + \frac{\rho}{(A_s - A_c)}\frac{\partial^2 Q_s}{\partial z \partial t} \tag{12}$$

For the limiting case where the dura-matter is much stiffer than the pia-matter, which most closely approximates the limiting situation of a SSS fully obstructed with arachnoid scar tissue, the SSS section could be considered constant relatively to the SC section, implying $\frac{\partial Q_c}{\partial z} = -\frac{\partial Q_s}{\partial z}$.
Therefore, the equation (12) becomes :

$$\frac{\partial^2 \Delta P}{\partial z^2} + \frac{\rho}{A_s}\left(\frac{1}{1-\alpha_{cs}} + \frac{1}{\alpha_{cs}}\right)\frac{\partial^2 Q_c}{\partial z \partial t} = 0 \tag{13}$$

Morevover, using the SC wave speed expression (7), the continuity equation of the SC could be written as

$$\frac{\partial^2 \Delta P}{\partial t^2} + \frac{\rho c_c^2}{A_c}\frac{\partial^2 Q_c}{\partial z \partial t} = 0 \tag{14}$$

By combining equations (13))and (14), it yields the wave equation

$$\frac{\partial^2 \Delta P}{\partial t^2} - c_c^2 \alpha_{cs}\frac{\partial^2 \Delta P}{\partial z^2} = 0 \tag{15}$$

In this limiting case, the speeds of the waves modes are $c_1 = c_c\sqrt{\alpha_{cs}}$ and the second is $c_2 \simeq c_s$, as the dura-matter is assumed rigid. This case has been dealt

in the litterature by (Berkouk et al., 2003; Cirovic, 2009; Cirovic and Kim, 2012; Carpenter et al., 2003).

4.2. Viscous CSF

By proceeding in a similar way as previously, for the limiting case where the dura-matter is much stiffer than the pia-matter, it yields the following damped wave equation

$$\frac{\partial^2 \Delta P}{\partial t^2} - \alpha_{cs} c_c^2 \frac{\partial^2 \Delta P}{\partial z^2} + \beta \frac{\partial \Delta P}{\partial t} = 0 \tag{16}$$

where $\beta = \alpha_{cs}\sigma_c + \sigma_s(1-\alpha_{cs})$, $\sigma_c = -\dfrac{8\pi\mu}{\rho A_{c0}}$, $\sigma_s = -\dfrac{8\pi\mu(1-\lambda^2)}{\rho\gamma(A_{s0}-A_{c0})}$, $\gamma = 1 + \lambda^2 + \dfrac{1-\lambda^2}{\ln\lambda}$ and $\lambda = \dfrac{R_{c0}}{R_{s0}}$.

Equation (16) has a similar form to *the telegraphers equation* that describes the propagation and attenuation of electrical signals on telegraph lines. For an inviscid CSF, which means that $\beta = 0$, it yields $k_i = 0$, $k_r = c_c\sqrt{\alpha_{cs}}$ and thus the wave equation (15).

To solve (16), we assume a periodic pressure perturbation

$$\Delta P = \hat{P}_t \exp^{i\omega t} \exp^{i(k_r + ik_i)z} \tag{17}$$

where w represents the pulsation, k_r is the wave speed and k_i is the attenuation coefficient. Equation (17) is assumed time-continuous. The wave damping considered here is spatial. By substituting equation (17) in equation (16), it yields the following expressions of k_r and k_i

$$k_i = -\frac{\omega}{c_c\sqrt{\alpha_{cs}}}\left(\frac{-1+\sqrt{1+\frac{\beta^2}{\omega^2}}}{2}\right)^{\frac{1}{2}} \tag{18}$$

$$k_r = c_c\sqrt{\alpha_{cs}}\left(\frac{2}{1+\sqrt{1+\frac{\beta^2}{\omega^2}}}\right)^{\frac{1}{2}} \tag{19}$$

(Note : mettre figure entre csf visqueux et non visqueux et commentaire ...)

5. Verification and validation

Numerical results are confronted to (Cirovic and Kim, 2012) study case where the CSF was assumed inviscid. Thus, the friction term due to the viscosity of the CSF which correponds to the right-hand side of the momentum equations equations (1) and (2) are removed.

Geometrical and mechanical properties of (Cirovic and Kim, 2012) idealized geometry are used. The length of the model is 0.5 m, the elastance of the pia-matter is 0.125 MPa, the elastance of the dura-matter is 0.14 MPa, the radius of the SC is 0.5 mm, the radius of the SSS is 0.85 mm and the density of the CSF is 10^3 kg.m^{-3}. A pulse excitation is initiated in the SSS. It consists of a half-sine pressure wave with a duration of 10^{-2}s and an amplitude of 100 Pa defined as

$$f(t) = \begin{cases} 100\sin(wt) & \text{for } t \leq 10^{-2}s \\ 0 & \text{for } t > 10^{-2}s \end{cases}$$

where $\omega = \dfrac{2\pi}{T}$, $T = 2.10^{-2}s$.

The boundary conditions consist of zero velocity of the CSF at the cranial end and at the caudal end. In the SSS, it consists of the pressure signal ($P_s = f(t)$) at the cranial end and zero velocity at the caudal end.

Numerical results were highly consistent with (Cirovic and Kim, 2012). Results shows two waves propagating along the geometry. The speeds at which the waves propagate are $c_1 = 7.4m/s$ and $c_2 = 14.7m/s$.

The purpose of this study case was to verify our two step Lax Wendroff numerical scheme. The wave propagation behaviour will not be discussed here as this case has been well documented and studied previously in the litterature (Cirovic, 2009; Cirovic and Kim, 2012) and (Berkouk et al., 2003; Carpenter et al., 2003).

6. Quasi-steady flow approximation

The oscillatory flow of a viscous, incompressible fluid in a straight, circular pipe with rigid walls is well known. A dimensionless number that serve as a general purpose indicator of the nature of unsteady flow is the Womersley number, W_o,

$$W_o = R\sqrt{\frac{\omega\rho}{\mu}} \tag{20}$$

where w is taken as the frequency of the oscillatory pressure gradient, R is the radius of the tube, ρ and μ are respectively the density and the viscosity of the fluid.

In this section, particular interest is given for the annular SSS. Tsangaris (1984) is the first to derive an analytical expression for the velocity for laminar, incompressible, and viscous flow in a circular annulus tube with rigid walls under a periodic oscillatory pressure gradient.

In a cylindrical coordinate system r, θ and z, the exact complex solution of this axial velocity u_{osc} is

$$u_{osc}(r') = -\frac{i}{W_o^2}\left(1 - \frac{aI_0(x) + bK_0(x)}{c}\right)$$

where I_0 and K_0 are respectively the modified Bessel functions of the first and second kind, R_c is the radius of the SC, R_s is the radius of the SSS, r' is a dimensionless radius $r' = \dfrac{r}{R_s}$, $\lambda = \dfrac{R_c}{R_s}$ is the ratio of the SC radius to the SSS one, $x = W_o i^{\frac{1}{2}} r'$, $a = K_0(\lambda W_o i^{\frac{1}{2}}) - K_0(W_o i^{\frac{1}{2}})$, $b = I_0(W_o i^{\frac{1}{2}}) - I_0(\lambda W_o i^{\frac{1}{2}})$ and $c = I_0(W_o i^{\frac{1}{2}})K_0(\lambda W_o i^{\frac{1}{2}}) - I_0(\lambda W_o i^{\frac{1}{2}})K_0(\lambda W_o i^{\frac{1}{2}})$.

Tsangaris (1984) have obtained the amplitude and the phase difference angle of the velocity as a function of the Womersley number, W_o, and the ratio of the annular radi r'.

Figures 2 and 3 shows the velocity amplitude U and the phase difference δ for two different values of λ (λ = 0.1, 0.5) and various values of the frequency parameter W_o (W_o = 0, 1, 3, 5, 8, 10).

For small values of W_o, for instance $W_o = 1$, the velocity amplitude is the same as that for the steady flow and the phase angle δ is almost constant and equal

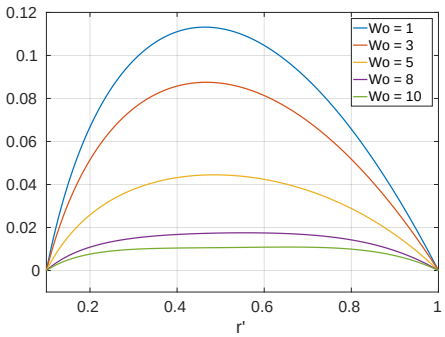

(a) λ=0.1

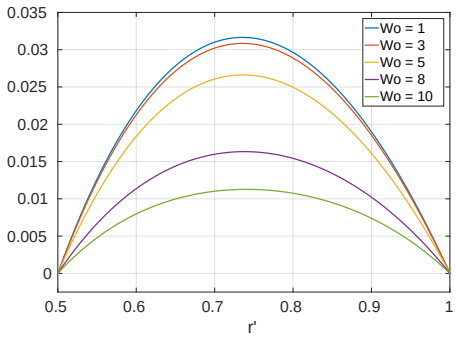

(b) λ=0.5

Figure 2: Amplitude distribution of the oscillatory flow over the cross section for an annuli for λ=0.1, 0.5 and W_0 = 0, 1, 3, 5, 8, 10 (Tsangaris, 1984)

to zero. This means that the flow for small values of W_o behaves as a quasi-steady Poiseuille flow in phase with pressure gradient. For greater values of W_o, the velocity amplitude and the phase angle δ are decreased for the same value of λ. Moreover, for greater values of W_o, the velocity amplitude remains approximately the same by varying λ.

Now, the expression of the velocity u_{osc} is used to express the wall shear stresses (3) in the momentum equation of the SSS (2)

$$\tau_{sd} = \mu \frac{\partial u_{osc}}{\partial r'}\bigg|_{r'=1} = \frac{i^{\frac{3}{2}}}{W_o c}\left(aI_1(W_o i^{\frac{1}{2}}) - bK_1(W_o i^{\frac{1}{2}})\right)$$

$$\tau_{cs} = \mu \frac{\partial u_{osc}}{\partial r'}\bigg|_{r'=\lambda} = \frac{i^{\frac{3}{2}}}{W_o c}\left(aI_1(\lambda W_o i^{\frac{1}{2}}) - bK_1(\lambda W_o i^{\frac{1}{2}})\right)$$

A dimensionless "average" wall shear stress in the annular section corresponding to the right hand side of the momentum equation (2) is defined as

$$\overline{\tau_w} = \frac{R_s\tau_{sd} - R_c\tau_{cs}}{R_c + R_s} = \frac{\tau_{sd} - \lambda\tau_{cs}}{1+\lambda} \tag{21}$$

Figure 4a displays the variation of the amplitude of the "averaged" wall shear stress in the annuli, $\overline{\tau_w}$, for different values of the Womersley number W_o and the radius ratio λ.

It shows that

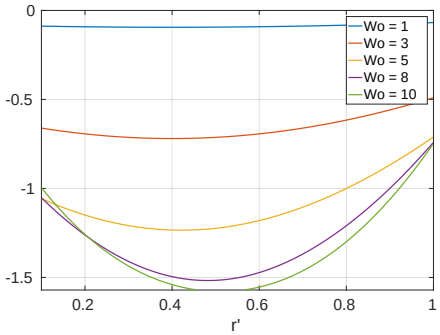

(a) λ=0.1

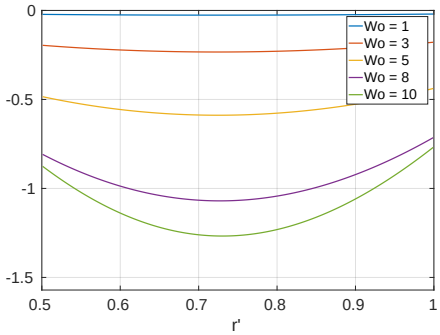

(b) λ=0.5

Figure 3: Phase angle distribution of the oscillatory flow over the cross section for an annuli λ=0.1, 0.5 and W_0 = 0, 1, 3, 5, 8, 10 (Tsangaris, 1984)

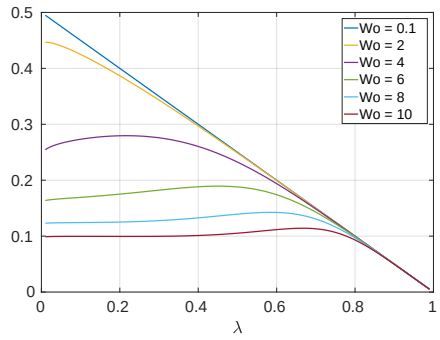

(a) Based on outer radius

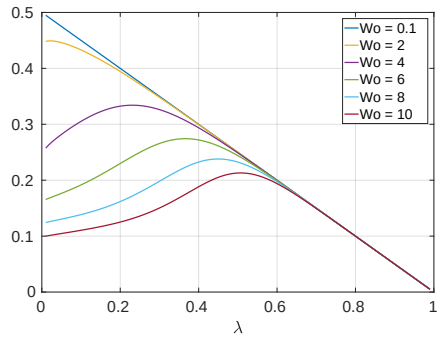

(b) Based on hydraulic radius

Figure 4: Amplitude of the "average" wall shear stress $\overline{\tau_w}$ for different values of the Womersley number as a function of the radii ratio λ

- For a weakly unsteady flow, for instance $W_o < 2$, the amplitude of $\overline{\tau_w}$ varies in a quasi-linear way with the radius ratio λ.
- For a strongly unsteady flow, for instance $W_o > 8$, the amplitude of $\overline{\tau_w}$ is quasi-constant with a radius ratio λ between 0 and 0.5.
- For $\lambda > 0.8$, the amplitude of $\overline{\tau_w}$ remain the same regardless the nature of the unsteady flow.

  The velocity profile tend to exhibit a Poiseuille shape and loses its phase lag with the pressure gradient. The more the annuli is confined, the more the average wall shear stress $\overline{\tau_w}$ of a quasi-steady flow approximation is valid.

Before proceeding further, please note that the definition of the Womersley number used by Tsangaris (1984) for an annuli takes into account as a characteristic length the outer radius of the annuli, neglecting the effect of the inner radius. Thereafter, we define a local Womersley number based on the inner and the outer radius : a hydraulic radius. The hydraulic radius R_h was calculated based on the cross-sectional area and wetted perimeter as

$$R_h = 2\frac{\pi(R_s^2 - R_c^2)}{2\pi(R_c + R_s)} = R_s - R_c \tag{22}$$

The local Womersley number, W_{oh}, is then equal to

$$W_{oh} = (R_s - R_c)\sqrt{\frac{\omega\rho}{\mu}} = W_o(1 - \lambda) \tag{23}$$

Therefore, the "average" wall shear stress (21) is rescaled as a function of the local Womersley number W_{oh}.

Figure 4b shows the variation of $\overline{\tau_w}$ for different values of W_{oh} as a function of λ.

Remarks held previously remain invariable except that the amplitude of $\overline{\tau_w}$ is no longer quasi-constant with a radius ratio λ between 0 and 0.5. However, the area of validity of the quasi-steady flow assumption noticed at Figure 4a has become wider in Figure (4b) by taking into account the inner radius. The quasi-steady flow assumption is considered acceptable when the minimum value

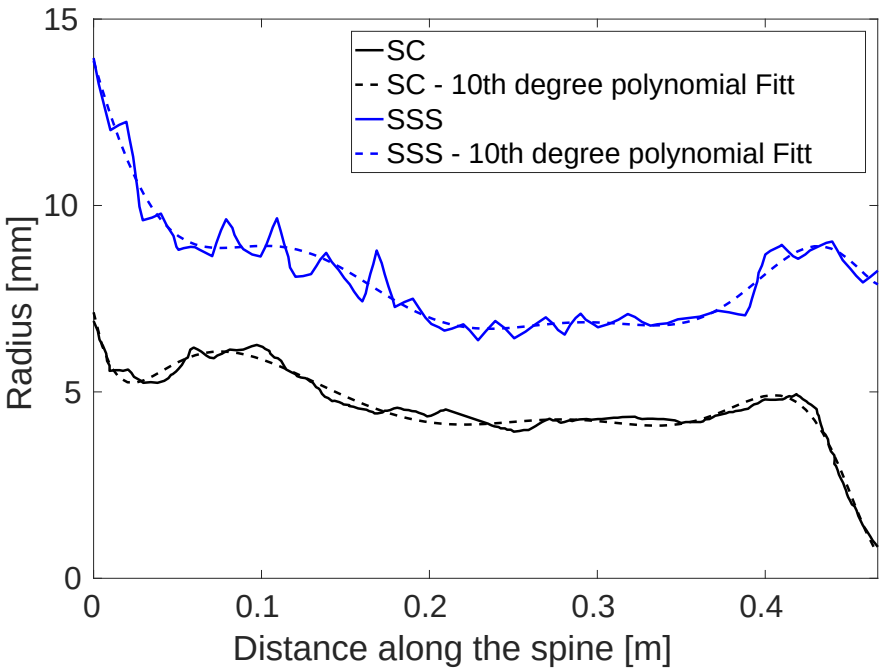

Figure 5

of the radius ratio λ is around 0.6.

MRI data from the Visible Human Project (VHP) provide outlines of the cord and of the SSS/dura interface at 49 sites along the spinal cord. At each cross-section, Bertram (2009) computed the area of each closed outline and the radius of a circle having the same area was calculated. Figure 5 displays these results. The radius ratio λ is computed based on these data. Except near the skull and the base of the spine, hydraulic radius λ is greater than 0.6. It can be assumed that when accounting for the CSF viscosity, the quasi-steady flow approximation for this area is acceptable.

7. Acknowledgments

References

Berkouk, K., Carpenter, P.W., Lucey, A.D., 2003. Pressure wave propagation in fluid-filled co-axial elastic tubes. Part 1: Basic theory. Journal of Biomechanical Engineering 125, 852–856.

Bertram, C.D., 2009. A numerical investigation of waves propagating in the spinal cord and subarachnoid space in the presence of a syrinx. Journal of Fluids and Structures 25, 1189–1205. URL: http://www.sciencedirect.com/science/article/pii/S0889974609000760, doi:10.1016/j.jfluidstructs.2009.06.008.

Bertram, C.D., Brodbelt, A.R., Stoodley, M.A., 2005. The origins of syringomyelia: numerical models of fluid/structure interactions in the spinal cord. Journal of Biomechanical Engineering 127, 1099–1109.

Carpenter, P.W., Berkouk, K., Lucey, A.D., 2003. Pressure wave propagation in fluid-filled co-axial elastic tubes. Part 2: Mechanisms for the pathogenesis of syringomyelia. Journal of Biomechanical Engineering 125, 857–863.

Cirovic, S., 2009. A coaxial tube model of the cerebrospinal fluid pulse propagation in the spinal column. Journal of Biomechanical Engineering 131, 021008. doi:10.1115/1.3005159.

Cirovic, S., Kim, M., 2012. A one-dimensional model of the spinal cerebrospinal-fluid compartment. Journal of Biomechanical Engineering 134, 021005. doi:10.1115/1.4005853.

Elliott, N.S.J., Lucey, A.D., Lockerby, D.A., Brodbelt, A.R., 2017. Fluid-structure interactions in a cylindrical layered wave guide with application in the spinal column to syringomyelia. Journal of Fluids and Structures 70, 464–499. URL: http://www.sciencedirect.com/science/article/pii/S088997461630158X, doi:10.1016/j.jfluidstructs.2016.11.007.

Flanagan, M.F., 2015. The Role of the Craniocervical Junction in Craniospinal Hydrodynamics and Neurodegenerative Conditions. Neurology Research International 2015, 794829. doi:10.1155/2015/794829.

Haughton, V., Mardal, K.A., 2014. Spinal fluid biomechanics and imaging: an update for neuroradiologists. AJNR. American journal of neuroradiology 35, 1864–1869. doi:10.3174/ajnr.A4023.

Lockey, M.P., Poots, G., Williams, B., 1975. Theoretical aspects of the attenuation of pressure pulses within cerebrospinal-fluid pathways. Medical and biological engineering 13, 861–869. URL: https://link.springer.com/article/10.1007/BF02478090, doi:10.1007/BF02478090.

Loth, F., Yardimci, M.A., Alperin, N., 2001. Hydrodynamic modeling of cerebrospinal fluid motion within the spinal cavity. Journal of Biomechanical Engineering 123, 71–79.

Luciano, M., Dombrowski, S., 2007. Hydrocephalus and the heart: interactions of the first and third circulations. Cleveland Clinic Journal of Medicine 74 Suppl 1, S128–131.

Sakka, L., Coll, G., Chazal, J., 2011. Anatomy and physiology of cerebrospinal fluid. European Annals of Otorhinolaryngology, Head and Neck Diseases 128, 309–316. doi:10.1016/j.anorl.2011.03.002.

Tsangaris, 1984. Oscillatory flow of an incompressible, viscous fluid in a straight annular pipe
. Journal de mcanique thorique et applique 3, 467–478. URL: http://www.refdoc.fr/Detailnotice?idarticle.

VHP, . The National Library of Medicines Visible Human Project. URL: https://www.nlm.nih.gov/research/visible/visible_human.html.

Womersley, J.R., 1955. Mathematical theory of oscillating flow in an elastic tube. The Journal of Physiology 127, 37–38P.

Zagzoule, M., Marc-Vergnes, J.P., 1986. A global mathematical model of the cerebral circulation in man. Journal of Biomechanics 19, 1015–1022.

Appendix D

CSF cervical flow computed from 1D model vs. MRI Data

The following poster was presented during the 8th World Congress of Biomechanics held from 8 to 12 July, 2018 in Dublin Ireland

CSF cervical flow computed from 1D model vs. MRI Data

Marc Maher[1], Patricia Cathalifaud[1] & Mokhtar Zagzoule[1]

Institut de Mécanique des Fluides de Toulouse (IMFT), Université de Toulouse, CNRS, Toulouse, France

Motivation

The first objective of this study is to build a 1D model of the dynamics couplings between the blood cerebral vasculature, the cranial CSF, the spinal CSF and the spinal cord. Particular attention is given to the effect of mechanical properties of the CSF network on the cervical (C2-C3) CSF flow.
The second objective is to compare the 1D model outputs to MRI Data from healthy and suspected pathological (hydrocephalus) patients.

Methods

The figure shown below presents the 1D craniospinal CSF-blood coupled model. Blood flows from carotids and vertebrals vessels to jugular veins. Blood volume expanison triggers CSF displacement into the Spinal Canal. Each blood vessel is enclosed within a vessel representing the dura mater in which the CSF flows.

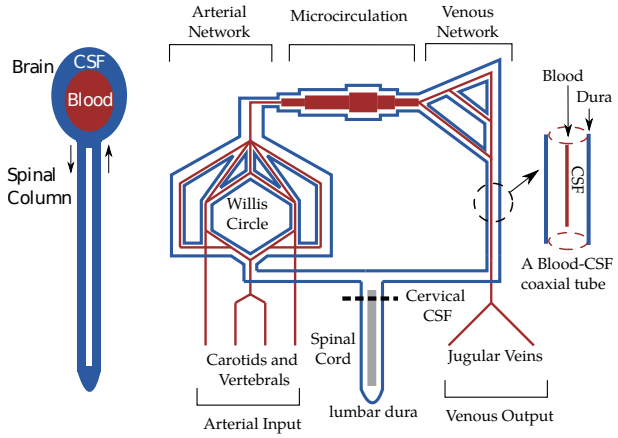

For the blood vessel, we have :

$$\begin{cases} \dfrac{\partial A_b}{\partial t} + \dfrac{\partial (U_b A_b)}{\partial z} = 0 \\ \dfrac{\partial U_b}{\partial t} + U_b \dfrac{\partial U_b}{\partial z} + \dfrac{1}{\rho_b} \dfrac{\partial P_b}{\partial z} = \dfrac{2\sqrt{\pi}}{\rho_b \sqrt{A_b}} \tau_b \end{cases}$$

For the spinal and cranial SS, we have :

$$\begin{cases} \dfrac{\partial A_c}{\partial t} + \dfrac{\partial U_c (A_c - A_b)}{\partial z} + \dfrac{\partial (U_c A_c)}{\partial z} = 0 \\ \dfrac{\partial U_c}{\partial t} + U_c \dfrac{\partial U_c}{\partial z} + \dfrac{1}{\rho_c} \dfrac{\partial P_c}{\partial z} \\ = -\dfrac{2\sqrt{\pi}}{\rho_c (A_c - A_b)} (\sqrt{(A_c)} \tau_{cb} - \sqrt{(A_c)} \tau_{cs}) \end{cases}$$

System closure: a tube law

$$P_t = E_l \left(\frac{A}{A_0} - 1 \right)$$

A is the cross-sectional area, U is the axial mean velocity, P is the pressure and τ is the wall shear force. (1)

Results : Input Blood Signal and resulting Cervical CSF Signal

In the litterature, CSF pressure amplitudes values ranges between 2 and 6 mmHg. C2-C3 CSF peak flow ranges between 1 and 4 mL/s. Figure belows presents the resulting C2-C3 CSF pressure amplitude and peak flow for two types of blood pressure input : a sinusoidal pulse and an arterial one. Figures shows 3 cardiac cycles.

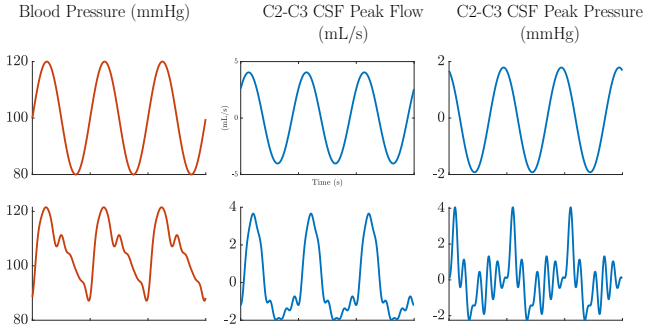

Results: What are the mechanical properties of the CSF network ?

We chose to characterize the CSF network using 3 parametres :

- The confinement $\dfrac{\text{Blood Vessel Section}}{\text{Dura Section}}$. A chosen confinement = A given CSF volume.

  MRI Data from litterature suggests total CSF volume vary between 150 mL and 300 mL.
- The compliance of the lumbar dura. CSF lumbar dura pressure is closely linked to Intracranial Pressure (ICP).
- The global elastance of the cranial and spinal dura.

Figures belows presents the effect of the CSF network parametres on the Cervical CSF peak Flow and pressure amplitude.

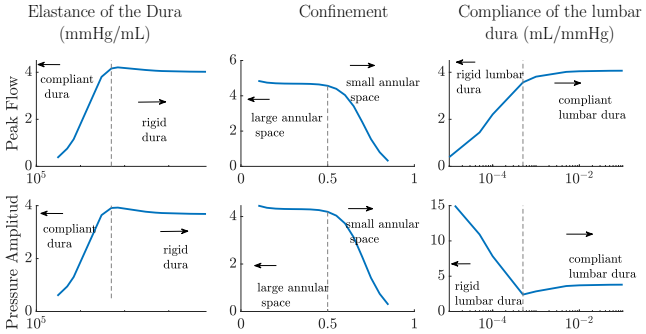

Results: Patient Specific 1D Model vs MRI Data

MRI Data from healthy and pathological patients providing flow signals and surface area of the Carotids, the Vertebrals, the Jugular Veins and the Cervical CSF region(C2-C3).

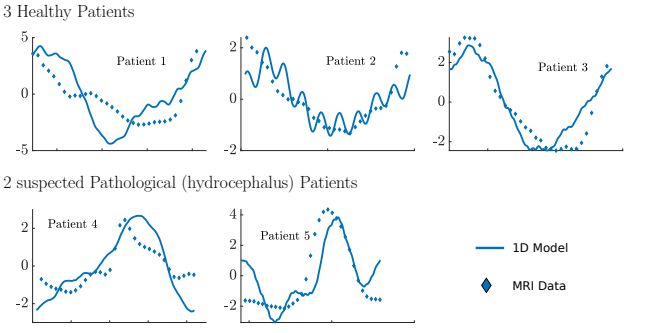

Discussion

We found good agreement between 1D Model and MRI Data. Results suggests that the Dura elastance is around 10^6 mmHg/mL, the compliance of the lumbar dura is around 10^{-4} mL/mmHg except for suspected pathological patient 4 where the Dura elastance is 10 times higher. Future work will be focusing on the optimal control modelling of the Cerebral Autoregulation mechanism.

Acknowledgements

We'd like to thank Olivier Baledent (BioFlowImage, CHU Amiens) for giving us access to their PCMRI data.

References

[1] Zagzoule Mokhtar & Maher Marc Cathalifaud Patricia. Wave propagation into the spinal cavity: a 1d model with coaxial compliant tubes. In *22nd Congress of the European Society of Biomechanics*, 2016.

Bibliography

[1] Lazorthes Guy 1910-2014. *Vascularisation et circulation de l'encephale. Tome I. Anatomie descriptive et fonctionnelle*. fre. Paris New York Barcelone: Masson, 1976 (cit. on p. 20).

[2] Andreas A. Linninger et al. "Cerebrospinal Fluid Mechanics and Its Coupling to Cerebrovascular Dynamics." In: *Annual Review of Fluid Mechanics* 48 (2016), pp. 219–257 (cit. on pp. 47, 60, 61).

[3] N. Alperin et al. "Automated Quantitation of Spinal CSF Volume and Measurement of Craniospinal CSF Redistribution Following Lumbar Withdrawal in Idiopathic Intracranial Hypertension." In: *American Journal of Neuroradiology* 37.10 (Oct. 2016), pp. 1957–1963 (cit. on p. 57).

[4] Noam Alperin et al. "From Cerebrospinal Fluid Pulsation to Noninvasive Intracranial Compliance and Pressure Measured by MRI Flow Studies." In: *Current Medical Imaging Reviews* 2.1 (Feb. 1, 2006), pp. 117–129 (cit. on p. 57).

[5] O. Balédent, M. C. Henry-Feugeas, and I. Idy-Peretti. "Cerebrospinal Fluid Dynamics and Relation with Blood Flow: A Magnetic Resonance Study with Semiautomated Cerebrospinal Fluid Segmentation." In: *Investigative Radiology* 36.7 (July 2001), pp. 368–377. pmid: `11496092` (cit. on pp. 47, 61, 64, 65).

[6] Olivier Balédent et al. "Relationship between Cerebrospinal Fluid and Blood Dynamics in Healthy Volunteers and Patients with Communicating Hydrocephalus." In: *Investigative Radiology* 39.1 (Jan. 2004), pp. 45–55 (cit. on p. 62).

[7] C. D. Bertram. "A Numerical Investigation of Waves Propagating in the Spinal Cord and Subarachnoid Space in the Presence of a Syrinx." In: *Journal of Fluids and Structures* 25.7 (2009), pp. 1189–1205 (cit. on p. 24).

[8] C. D. Bertram, A. R. Brodbelt, and M. A. Stoodley. "The Origins of Syringomyelia: Numerical Models of Fluid/Structure Interactions in the Spinal Cord." In: *Journal of Biomechanical Engineering* 127.7 (Dec. 2005), pp. 1099–1109 (cit. on p. 24).

[9] C. D. Bertram and M. Heil. "A Poroelastic Fluid/Structure-Interaction Model of Cerebrospinal Fluid Dynamics in the Cord With Syringomyelia and Adjacent Subarachnoid-Space Stenosis." In: *Journal of Biomechanical Engineering* 139.1 (Jan. 2017) (cit. on p. 25).

[10] Lynne E. Bilston and Lawrence E. Thibault. "The Mechanical Properties of the Human Cervical Spinal cordIn Vitro." In: *Annals of Biomedical Engineering* 24.1 (Sept. 1, 1995), pp. 67–74 (cit. on p. 25).

[11] P. D. Brown et al. "Molecular Mechanisms of Cerebrospinal Fluid Production." In: *Neuroscience* 129.4 (2004), pp. 957–970 (cit. on p. 15).

[12] Suncica Canic and Eun Heui Kim. "Mathematical Analysis of the Quasilinear Effects in a Hyperbolic Model Blood Flow through Compliant Axi-Symmetric Vessels." In: *Mathematical Methods in the Applied Sciences* 26.14 (2003), pp. 1161–1186 (cit. on p. 27).

[13] Gregory S. H. Chan et al. “Contribution of Arterial Windkessel in Low-Frequency Cerebral Hemodynamics during Transient Changes in Blood Pressure.” In: *Journal of Applied Physiology* 110.4 (Feb. 3, 2011), pp. 917–925 (cit. on p. 49).

[14] Dorian Chauvet et al. “Histological and Biomechanical Study of Dura Mater Applied to the Technique of Dura Splitting Decompression in Chiari Type I Malformation.” In: *Neurosurgical Review* 33.3 (July 2010), 287–294; discussion 295. pmid: `20440557` (cit. on p. 25).

[15] Srdjan Cirovic and Minsuok Kim. “A One-Dimensional Model of the Spinal Cerebrospinal-Fluid Compartment.” In: *Journal of Biomechanical Engineering* 134.2 (Feb. 2012), p. 021005 (cit. on pp. 25, 33).

[16] Marek Czosnyka et al. “Cerebrospinal Fluid Dynamics.” In: *Physiological Measurement* 25.5 (Oct. 2004), R51–76. pmid: `15535175` (cit. on pp. 47, 61).

[17] Helle H. Damkier, Peter D. Brown, and Jeppe Praetorius. “Cerebrospinal Fluid Secretion by the Choroid Plexus.” In: *Physiological Reviews* 93.4 (Oct. 2013), pp. 1847–1892 (cit. on pp. 12, 15).

[18] Dries De Kegel et al. “Biomechanical Characterization of Human Dura Mater.” In: *Journal of the Mechanical Behavior of Biomedical Materials* 79 (Mar. 1, 2018), pp. 122–134 (cit. on p. 25).

[19] Florian Doepp et al. “How Does the Blood Leave the Brain? A Systematic Ultrasound Analysis of Cerebral Venous Drainage Patterns.” In: *Neuroradiology* 46.7 (July 2004), pp. 565–570. pmid: `15258709` (cit. on p. 65).

[20] Zakaria Doulfoukar et al. “Méthode numérique pour la résolution de l’écoulement d’un fluide viscoélastique en conduite à paroi déformable.” In: *Journal de Physique III* 6.3 (Mar. 1, 1996), pp. 433–442 (cit. on p. 31).

[21] Steffi Dreha-Kulaczewski et al. “Respiration and the Watershed of Spinal CSF Flow in Humans.” In: *Scientific Reports* 8.1 (Apr. 4, 2018), p. 5594 (cit. on p. 15).

[22] Michael Egnor et al. “The Cerebral Windkessel and Its Relevance to Hydrocephalus: The Notch Filter Model of Cerebral Blood Flow.” In: *Cerebrospinal Fluid Research* 3 (Suppl 1 Dec. 21, 2006), S48. pmid: `null` (cit. on p. 49).

[23] D. R. Enzmann and N. J. Pelc. “Brain Motion: Measurement with Phase-Contrast MR Imaging.” In: *Radiology* 185.3 (Dec. 1992), pp. 653–660 (cit. on p. 23).

[24] D. R. Enzmann and N. J. Pelc. “Cerebrospinal Fluid Flow Measured by Phase-Contrast Cine MR.” In: *AJNR Am J Neuroradiol* 14.6 (Dec. 1993), 1301–1307; discussion 1309–1310 (cit. on pp. 15, 23, 47, 61, 65).

[25] D. A. Frankel, D. P. Fessell, and W. P. Wolfson. “High Resolution Sonographic Determination of the Normal Dimensions of the Intracranial Extraaxial Compartment in the Newborn Infant.” In: *Journal of Ultrasound in Medicine: Official Journal of the American Institute of Ultrasound in Medicine* 17.7 (July 1998), 411–415; quiz 417–418. pmid: `9669298` (cit. on p. 23).

[26] M. Freund et al. “[Measurement of CSF flow in the spinal canal using MRI with an optimized MRI protocol: experimental and clinical studies].” In: *Rofo* 173.4 (Apr. 2001), pp. 306–314 (cit. on p. 15).

[27] James E. Galford and James H. McElhaney. “A Viscoelastic Study of Scalp, Brain, and Dura.” In: *Journal of Biomechanics* 3.2 (Mar. 1, 1970), pp. 211–221 (cit. on p. 25).

[28] D. Greitz et al. “Pulsatile Brain Movement and Associated Hydrodynamics Studied by Magnetic Resonance Phase Imaging. The Monro-Kellie Doctrine Revisited.” In: *Neuroradiology* 34.5 (1992), pp. 370–380. pmid: 1407513 (cit. on p. 15).

[29] Sumeet Gupta et al. “Three-Dimensional Computational Modeling of Subject-Specific Cerebrospinal Fluid Flow in the Subarachnoid Space.” In: *Journal of Biomechanical Engineering* 131.2 (Feb. 2009), p. 021010 (cit. on p. 48).

[30] Leszek Herbowski. “The Maze of the Cerebrospinal Fluid Discovery.” In: *Anatomy Research International*. 2013 (cit. on p. 2).

[31] J.V. Hickey. *Clinical Practice of Neurological and Neurosurgical Nursing*. Wolters Kluwer Health, 2011 (cit. on p. 4).

[32] O. Hunziker and A. Schweizer. “Postmortem changes in stereological parameters of cerebral capillaries.” eng. In: *Beiträge zur Pathologie: "Aschoff's" Journal* 161.3 (1977), pp. 244–255 (cit. on p. 20).

[33] Zaamin B Hussain, Amaani B Hussain, and Patrick Mitchell. “Extra-Axial Cerebrospinal Fluid Spaces in Children with Benign External Hydrocephalus: A Case-Control Study.” In: *The Neuroradiology Journal* 30.5 (Oct. 2017), pp. 410–417. pmid: 28691570 (cit. on p. 23).

[34] Conrad E. Johanson et al. “Multiplicity of Cerebrospinal Fluid Functions: New Challenges in Health and Disease.” In: *Cerebrospinal Fluid Research* 5 (May 2008), p. 10 (cit. on p. 12).

[35] Miles Johnston et al. “Evidence of Connections between Cerebrospinal Fluid and Nasal Lymphatic Vessels in Humans, Non-Human Primates and Other Mammalian Species.” In: *Cerebrospinal Fluid Research* 1 (Dec. 2004), p. 2 (cit. on p. 12).

[36] Wojciech Kalata et al. “MR Measurement of Cerebrospinal Fluid Velocity Wave Speed in the Spinal Canal.” In: *IEEE transactions on bio-medical engineering* 56.6 (June 2009), pp. 1765–1768 (cit. on p. 59).

[37] Yi-Hsuan Kao et al. “The Respiratory Modulation of Intracranial Cerebrospinal Fluid Pulsation Observed on Dynamic Echo Planar Images.” In: *Magnetic Resonance Imaging* 26.2 (Feb. 2008), pp. 198–205 (cit. on p. 15).

[38] W. W. Lam et al. “Ultrasonographic Measurement of Subarachnoid Space in Normal Infants and Children.” In: *Pediatric Neurology* 25.5 (Nov. 2001), pp. 380–384. pmid: 11744312 (cit. on p. 23).

[39] G Lazorthes. “Arterial vascularization of the brain stem. Research technic and new data.” fre. In: *Bulletin de l'Academie nationale de medecine* 149.30 (1965) (cit. on p. 20).

[40] M. Libicher and J. Tröger. “US Measurement of the Subarachnoid Space in Infants: Normal Values.” In: *Radiology* 184.3 (Sept. 1992), pp. 749–751. pmid: 1509061 (cit. on p. 23).

[41] Andreas A. Linninger et al. “A Mathematical Model of Blood, Cerebrospinal Fluid and Brain Dynamics.” In: *Journal of Mathematical Biology* 59.6 (2009), pp. 729–759 (cit. on p. 6).

[42] F. Loth, M. A. Yardimci, and N. Alperin. “Hydrodynamic Modeling of Cerebrospinal Fluid Motion within the Spinal Cavity.” In: *Journal of Biomechanical Engineering* 123.1 (Feb. 2001), pp. 71–79 (cit. on pp. 48, 55).

[43] Mark Luciano and Stephen Dombrowski. “Hydrocephalus and the Heart: Interactions of the First and Third Circulations.” In: *Cleveland Clinic Journal of Medicine* 74 Suppl 1 (Feb. 2007), S128–131. pmid: 17455561 (cit. on pp. 49, 61).

[44] Melody P. Lun, Edwin S. Monuki, and Maria K. Lehtinen. “Development and Functions of the Choroid Plexus–Cerebrospinal Fluid System.” In: *Nature reviews. Neuroscience* 16.8 (Aug. 2015), pp. 445–457 (cit. on p. 12).

[45] Jason T. Maikos, Ragi A. I. Elias, and David I. Shreiber. “Mechanical Properties of Dura Mater from the Rat Brain and Spinal Cord.” In: *Journal of Neurotrauma* 25.1 (Jan. 2008), pp. 38–51. pmid: 18355157 (cit. on p. 25).

[46] Edward L. Mazuchowski and Lawrence E. Thibault. “BIOMECHANICAL PROPERTIES OF THE HUMAN SPINAL CORD AND PIA MATER.” In: (cit. on p. 25).

[47] C. B. McArdle et al. “Developmental Features of the Neonatal Brain: MR Imaging. Part II. Ventricular Size and Extracerebral Space.” In: *Radiology* 162 (1 Pt 1 Jan. 1987), pp. 230–234. pmid: 3786768 (cit. on p. 23).

[48] B. Mokri. “The Monro-Kellie Hypothesis: Applications in CSF Volume Depletion.” In: *Neurology* 56.12 (June 26, 2001), pp. 1746–1748. pmid: 11425944 (cit. on p. 16).

[49] Nejat Narli et al. “Ultrasonographic Measurement of Subarachnoid Space in Normal Term Newborns.” In: *European Journal of Radiology* 58.1 (Apr. 2006), pp. 110–112. pmid: 16406435 (cit. on p. 23).

[50] Frank H. Netter. *Atlas of Human Anatomy*. Elsevier Health Sciences, Dec. 19, 2017. 674 pp. (cit. on pp. 11, 14–16).

[51] *Neuroscience*. 2nd. Sinauer Associates, 2001 (cit. on p. 10).

[52] Hiroshi Ozawa et al. “Mechanical Properties and Function of the Spinal Pia Mater.” In: *Journal of Neurosurgery. Spine* 1.1 (July 2004), pp. 122–127. pmid: 15291032 (cit. on p. 25).

[53] Soroush Heidari Pahlavian et al. “The Impact of Spinal Cord Nerve Roots and Denticulate Ligaments on Cerebrospinal Fluid Dynamics in the Cervical Spine.” In: *PLOS ONE* 9.4 (Apr. 2014), e91888 (cit. on p. 48).

[54] Dennis Patin et al. “Anatomic and Biomechanical Properties of Human Lumbar Dura Mater.” In: *Anesthesia & Analgesia* 76.3 (Mar. 1, 1993), pp. 535–540. pmid: 8452262 (cit. on p. 25).

[55] T. J. Pedley. *The Fluid Mechanics of Large Blood Vessels by T. J. Pedley*. Apr. 1980. (Visited on 05/13/2019) (cit. on p. 31).

[56] Michael Pollay. "The Function and Structure of the Cerebrospinal Fluid Outflow System." In: *Cerebrospinal Fluid Research* 7 (June 2010), p. 9 (cit. on p. 12).

[57] P. Prassopoulos and D. Cavouras. "CT Evaluation of Normal CSF Spaces in Children: Relationship to Age, Gender and Cranial Size." In: *European Journal of Radiology* 18.1 (Feb. 1, 1994), pp. 22–25 (cit. on p. 23).

[58] Alfio Quarteroni and Luca Formaggia. "Mathematical Modelling and Numerical Simulation of the Cardiovascular System." In: *Handbook of Numerical Analysis*. Vol. 12. Computational Models for the Human Body. Elsevier, Jan. 1, 2004, pp. 3–127 (cit. on p. 31).

[59] Adnan I. Qureshi et al. "Patterns and Rates of Supplementary Venous Drainage to the Internal Jugular Veins." In: *Journal of Neuroimaging: Official Journal of the American Society of Neuroimaging* 26.4 (July 2016), pp. 445–449. pmid: 26888667 (cit. on p. 65).

[60] Leonardo Rangel-Castillo, Shankar Gopinath, and Claudia S. Robertson. "Management of Intracranial Hypertension." In: *Neurologic Clinics* 26.2 (2008). Neurologic Critical Care, pp. 521 –541 (cit. on p. 4).

[61] G. Rodríguez-Boto et al. "Basic concepts about brain pathophysiology and intracranial pressure monitoring." In: *Neurología (English Edition)* 30.1 (2015), pp. 16–22 (cit. on pp. 3, 47).

[62] M. Runza et al. "Lumbar Dura Mater Biomechanics: Experimental Characterization and Scanning Electron Microscopy Observations." In: *Anesthesia and Analgesia* 88.6 (June 1999), pp. 1317–1321. pmid: 10357337 (cit. on p. 25).

[63] L. Sakka, G. Coll, and J. Chazal. "Anatomy and Physiology of Cerebrospinal Fluid." In: *Eur Ann Otorhinolaryngol Head Neck Dis* 128.6 (Dec. 2011), pp. 309–316 (cit. on pp. 12, 57).

[64] Diego San Millán Ruíz et al. "The Craniocervical Venous System in Relation to Cerebral Venous Drainage." In: *AJNR. American journal of neuroradiology* 23.9 (Oct. 2002), pp. 1500–1508. pmid: 12372739 (cit. on p. 65).

[65] Mansoor Sharifi et al. "The Choroid Plexus of the Fourth Ventricle and Its Arteries." In: *Folia Morphologica* 64.3 (Aug. 2005), pp. 194–198 (cit. on p. 12).

[66] Spencer Sherwin et al. "Computational Modeling of 1D Blood Flow with Variable Mechanical Properties and Application to the Simulation of Wave Propagation in the Human Arterial System." In: *Int. J. Numer. Meth. Fluids* 43 (Oct. 2003), pp. 673–700 (cit. on p. 31).

[67] Yubing Shi, Patricia Lawford, and Rodney Hose. "Review of Zero-D and 1-D Models of Blood Flow in the Cardiovascular System." In: *BioMedical Engineering OnLine* 10 (Apr. 2011), p. 33 (cit. on p. 31).

[68] T. Speake et al. "Mechanisms of CSF Secretion by the Choroid Plexus." In: *Microscopy Research and Technique* 52.1 (Jan. 1, 2001), pp. 49–59. pmid: 11135448 (cit. on p. 12).

[69] Souraya Stoquart-Elsankari et al. “A Phase-Contrast MRI Study of Physiologic Cerebral Venous Flow.” In: *Journal of Cerebral Blood Flow and Metabolism: Official Journal of the International Society of Cerebral Blood Flow and Metabolism* 29.6 (June 2009), pp. 1208–1215. pmid: 19352399 (cit. on p. 65).

[70] Mark E. Wagshul, Per K. Eide, and Joseph R. Madsen. “The Pulsating Brain: A Review of Experimental and Clinical Studies of Intracranial Pulsatility.” In: *Fluids and Barriers of the CNS* 8 (Jan. 2011), p. 5 (cit. on p. 15).

[71] Nico Westerhof, Jan-Willem Lankhaar, and Berend E. Westerhof. “The Arterial Windkessel.” In: *Medical & Biological Engineering & Computing* 47.2 (Feb. 1, 2009), pp. 131–141 (cit. on p. 49).

[72] K. Zagórska-Swiezy et al. “Arterial Supply and Venous Drainage of the Choroid Plexus of the Human Lateral Ventricle in the Prenatal Period as Revealed by Vascular Corrosion Casts and SEM.” In: *Folia Morphologica* 67.3 (Aug. 2008), pp. 209–213 (cit. on p. 12).

[73] M. Zagzoule and J. P. Marc-Vergnes. “A Global Mathematical Model of the Cerebral Circulation in Man.” In: *J Biomech* 19.12 (1986), pp. 1015–1022 (cit. on pp. 7, 16, 19–21, 37).

[74] Rui Zou et al. “Intracranial pressure waves: Characterization of a pulsation absorber with notch filter properties using systems analysis - Laboratory investigation.” In: *Journal of Neurosurgery: Pediatrics* 2.1 (July 2008), pp. 83–94. pmid: 18590402 (cit. on p. 49).